Università degli Studi della Calabria

Dipartimento di Fisica

Tesi di Dottorato di Ricerca in Fisica, Ciclo XX

FIS/03

Chemical and morphological influence on nanostructures: synthesis and characterization of Carbon-based materials
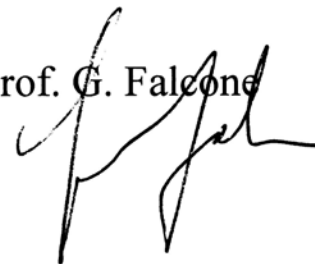
Dr. Alfonso Policicchio

Supervisore

Prof. R. G. Agostino

Coordinatore
del corso di Dottorato

Prof. G. Falcone

Anno Accademico 2007 – 2008

Dr. A. Policicchio

A Mia Nonna 01-01-1916….

" 'A vita mia ! "

Index

1. Introduction

1.1 Preface

The extremely broad effort that the scientific community is putting on the so-called Nanoscience is mainly related to the comprehension of the nanometric-size effects on the physico-chemical properties of the matter. Both, organic and inorganic materials behave in a peculiar way when sets of few atoms are concerned.

Connected to Nanoscience, Nanotechnology is the creation of useful materials, devices, and system through the control of matter on the nanometer scale and the exploitation of novel properties and phenomena developed at the length scale [1]. At the nanometer scale, the wavelike properties of electron inside matter and atomic interactions are influenced by the size of the material [2]. As a consequence, changes in melting point, magnetic, optical and/or electronic properties can be observed as the material takes on nanoscale dimensions.

Due to the high surface-to-volume ratio associated with nanometer-sized materials, a tremendous improvement in chemical properties is also achievable through the reduction in size [2]. By creating nanostructures, therefore, it is possible to control the fundamental properties of materials even without changing the materials chemical composition.

This should, in principle, allow us to develop new materials with useful properties and advanced devices with desirable features for a wide range of applications. Carbon allotropes, whose variety is in continuous expansion, represent a referred category for the study and the use of nanometer sized materials because of their compatibility with both biological and physical systems [1].

Since the discovery of fullerenes and nanotubes, nanostructure carbon-based materials occupy a strategic position in materials science and nanotechnology as one of the most promising and far-reaching systems [2].

Fullerenes and nanotubes have become prominent ingredients in materials science and in nanotechnology. However their incorporation in a solid material or their implementation in micro- and/or nanofabricated platforms remains a major challenge [3]. The work on fullerenes and nanotubes has stimulated and renewed the interest on a broad class of materials generically called nanocarbons or nanostructured carbons [2,4]. These can be obtained by the assembling in various conditions of carbon nanostructures and they are characterized by a hierarchical organization of hybridization, structure and porosity ranging from the nano- to the micrometer scale [4]. Nanostructured carbon offers a growing number of applications in the field of supercapacitors [5,6], fuel cells [7], advanced catalyst supports [8], gas sensors [9,10] and biosensors [11].

In order to establish a link between nanostructure, mesostructure and material performances, production, characterization and manipulation techniques have to be developed and fully mastered down to the nanometric scale (see Par. 3). In nanostructured carbon-based materials the physico-chemical properties are influenced by the pore dimension, surface morphology and local curvature [13,14]. Nanostructured carbon has an electronic conductivity ranging from insulator to metallic-like. This is mainly related to the energy distribution of the π and π^* orbitals in the energy gap between σ and σ^* states [15].

The structural and electronic properties of carbon-based nanostructures are influenced by the inclusion of dopant atoms or nanoparticles. Recently considerable attention has been paid to the possibility of incorporating metal species into different kind of carbon nanostructures (carbon nanotubes) to control their properties and expand their applicability and physico-chemical properties (see Par 3.2, 3.3). It has been shown that the incorporation of metallic atoms or clusters can be used to modify at the same time the local hybridization and hence curvature, the porosity and the electronic structure.

Although very promising, the study of carbon-based nanocomposites is still in its infancy since the mechanisms affecting the growth of carbon nano- and mesostructures in the presence of metallic species is largely unknown. Moreover the large number of parameters affecting the synthetic process makes very

difficult the identification of methods allowing an independent control of the content and distribution of a specific metallic species in a carbon with a fixed structure [17]. An arsenal of advanced growth methods has now the potential to provide a large variety of nanostructured carbon materials with tailored properties and functions [2].

The scientific and technological knowledge acquired during the past decade in the controlled synthesis of carbon nanotubes and nanofibers is of fundamental value to open the door to applications in the field of catalysis, electrochemistry, molecular electronics, chemical and bio-sensing [4].

A deep understanding of these systems needs a cross-linked study performed by making use of different techniques to put in relation the chemical and electronic features with the structural and morphological ones on both mesoscopic and nanoscopic scales (see Par. 2.2). In order to achieve a deep and systematic characterization of carbon-based nanostructures, we investigate chemical and morphological properties by Scanning Electron Microscopy (SEM), Scanning Tunnelling Microscopy/Spectroscopy (STM/STS) and the *traditional* Auger Electron Spectroscopy (AES). Furthermore, we made use of Electron Energy Loss Spectroscopy (EELS) and Raman spectroscopy to analyze the electronic and structural properties. A deeper insight is given by the Ultraviolet Photoemission Spectroscopy (UPS) performed on the SpectroMicroscopy beamline at the Elettra Synchrotron Light Source in Trieste and the Transmission Electron Microscopy (TEM) in the local Advanced Microscopy Laboratory.

Our aim is to explore new production techniques of nanostructured and nanocomposite carbon-based materials with tailored nanostructure, morphology, porosity and doping. Moreover, we investigate the interaction of nanostructured carbon and nanocomposites with light molecules.

The analysed systems are studied in the application framework. As an example, their functionalization with organic molecules is emerging as a promising advance for material science in view of the incorporation of many new properties to the inorganic substrate. Furthermore, the main advantages in

realizing hybrid structures are the size reduction and the spontaneous self-assembling capabilities. The resulting hybrid systems are very appealing candidates for the realization of molecule-based miniature devices with new or advanced functions [44-46]. In particular, the functionalization of single-wall carbon nanotubes [47] nanocomposites [48], and other C-based nanostructures [49] with organic molecules allows for the occurrence of photovoltaic properties that are appealing for device applications. Several studies concerning hybrid systems appeared in the recent past, mainly dedicated to carbon nanotubes (CNTs), fullerenes and complex molecules obtained by their functionalisation [50]. Up to now, several kind of organic molecules, such as monomers, oligomers and polymers were used to form complexes with C-based materials.

Obviously, many of the useful properties of the organic/inorganic interfaces are proportional to the available contact area but only nanostructured materials provide, together to a vast and accessible surface area, also the possibility to realize intercalated surfaces between hard and soft matter. This feature is essential, for example, in order to reduce the charge carrier paths when they are used as dispersed heterojunctions maximizing their efficiency. Phenomena as the carrier injection and separations are basically related to the interfacial electronic structure of organic/inorganic systems [51]. Among other applications, electroluminescent and photovoltaic devices were developed exploiting this effect [52]. As a starting point, the characterization of these interfaces concerns the variation of the vacuum level, the space charge formation and the band bending across the interface that, in turn, are directly related to the bonding characteristics and to the geometrical arrangement of the molecules [52].

1.2 Collaborations

Brookhaven National Laboratory Beam Line U12A – NIST Institute in Brookhaven, Long Island, New York (USA)

In collaboration with Prof. Faisal M. Alamgir on XPS/NEXAFS measurements on Co/Ag/Ni(111) and Platinum/Ruthenium thin film from 30/05/2007 to 01/07/2007.

Istituto per la Microelettronica e Microsistemi – Consiglio Nazionale delle Ricerche (IMM-CNR) – Catania (I)

In collaboration with Dr.ssa Silvia Scalese on the characterization of Carbon Nanocolumns produced by RF-Magnetron Sputtering at the IMM-CNR in Catania.

Liquid Crystal Laboratory – Physics Department, University of Calabria

Raman Laboratory: collaboration with Prof. Enzo Cazzanelli and Dr. Marco Castriota on production and characterization of Carbon-based nanostructures and in particular to the Carbon Nanotubes produced by Silicon Carbide surface decomposition.

AFM/STM Laboratory: in collaboration with Prof. Riccardo Barberi and Dr.ssa Maria De Santo on characterization of Carbon based nanostructures, and with

Prof. Carlo Versace, Prof. Nicola Scaramuzza and Dr. Stefano D'Elia on Carbon nanotubes produced from Silicon Carbide surface decomposition and characterization of PZT/ITO/Glass samples.

Department of Materials Science and Engineering - University of Ioannina (GR)

We work with Prof. Dimitrios Gournis, Dr. Theodoris Tsoufis and Prof. George Froudakis on Tin Filled Carbon Nanotubes, functionalized Carbon Nanotubes and also on other different system for hydrogen storage applications.

Elettra Syncrotron Light Source – Trieste (I)

BeamLine SpectroMicroscopy : we work with Dr. Salvatore La Rosa and Dr. Michele Bertolo to the UPS characterization of different systems:

- ✓ July 2005, Experiment n° 2005389, *Spatially resolved electronic and chemical structure of WO3 thin films*

- ✓ November 2005, Experiment n° 2005381, *Electronic phase separation mapping on stressed manganites thin films*

- ✓ March 2006, *Compositional distribution from the bulk to the surface and the surface morphology of thin-film Pt-Ru alloys prepared through interdiffusion*

BeamLine Material Science : we work with Dr. Kevin Prince

- ✓ March 2005, Experiment n° 2004371, *Resonant photoemission spettroscopy of cluster-assembled nanostructured TiO2*

- ✓ March 2006, Experiment n. 2005773, *Electronic structure of cluster assembled nanocrystalline TiO2 films: Resonant valence band photoemission and in-situ modification by thermal annealing*

 European Synchrotron Radiation Facility, Grenoble (F)

BeamLine BM8 Gilda : we work with Dr. Francesco D'Acapito for XAS

measurements on nanostructured carbon materials

- ✓ June 2005, Experiment n° 08-03-601, *XAS investigation on transition metal nano-cluster embedded in nanostructured carbon films*

2. Investigated systems and experimental approaches

2.1 Carbon-based nanostuctures

The dimensionality of a system has a profound influence on its physical behaviour, more specifically for nanostructured materials in which the size is comparable to the size of the fundamental physical quantities. Carbon-based nanostructured materials exhibit unique mechanical, electrical, and optical characteristics, which may result in many unique device designs [6]. The materials are biocompatible, chemically inert but capable of altering their electronic properties in the presence of some chemical species, and dimensionally compatible with biomolecules (their unique properties and morphological flexibility, rendering them inherently multifunctional and compatible with organic and inorganic systems). With the advances in technology over the past few decades, it has become possible to fabricate and study reduced-dimensional systems in which electron are strongly confined in one or more dimension. Recent revolutionary progress in the synthesis and characterization of carbon-based nanostructured materials and continuously emerging nanotechnologies has demonstrated tremendous potential for the development of new device [1].

The discovery of carbon nanotubes (CNTs) by Iijima in 1991 opened up a new era in material science and nanotechnology [3]. The application of carbon nanotube range from quantum wire interconnects [2], diodes and transistors for computing [3], high power electrochemical capacitors [4], data storage device [5], field emitters for flat panel displays [6, 7, 8] and terahertz oscillators [9]. Successfully contacted CNTs have exhibited a large number of useful quantum electronic and low dimensional transport phenomena [10], such as true quantum wire behaviour [11], room temperature field effect transistors [3], room temperature single electron transistors [12]. CNTs with aspect ratios of the order of 1000, coupled with a high conductivity, are ideal candidates for low voltage

field emitters, with applications in CNT-based cold-cathodes for X-ray generation [15]. When we talk about CNTs, we can image them as a particular type of the so called Carbon Nanofibers (CNFs).

CNFs are cylindrical or conical structures that have diameters varying from a few to hundreds of nanometers and lengths ranging from less than micron to millimiters. The internal structure of carbon nanofibers varies and is comprised of different arrangements of modified graphene sheets. A graphene layer can be defined as a hexagonal network of covalently bonded carbon atoms or a single two-dimensional (2D) layer of a three-dimensional (3D) graphite (fig. 1(a)). In general, a nanofiber consists of stacked curved graphite layers that form cones (fig. 1(b)) or "cups" [19,20]. The stacked cone structure is often referred to as herringbone (or fishbone) while the stacked cups structure is most often referred to as bamboo stem.
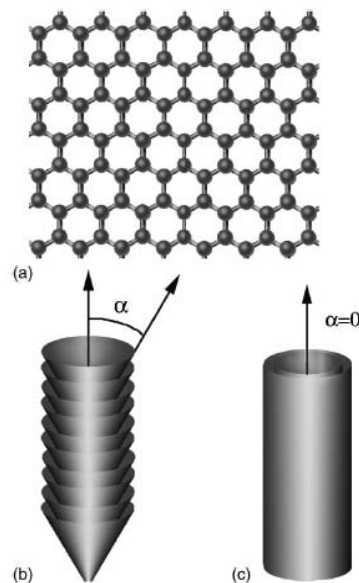
Figure 1. Schematic structure of carbon nanofibers and nanotubes. (a) Graphene layer, (b) stacked cone (herringbone) nanofiber, and (c) nanotube [4].

Currently there is no strict classification of nanofiber structures. The main distinguishing characteristic of nanofibers from nanotubes is the stacking of graphene sheets of varying shapes.

We can define α as an angle between the fiber axis and the graphene sheet near the sidewall surface (fig. 1(b)). The nanofiber with $\alpha = 0$ is a special case in which

one or more graphene layers form cylinders that run the full length of the nanostructure (fig. 1(c)). This arrangement results in extraordinary properties that made this type of a nanofiber known to the world as a carbon nanotubes.

The scientific community focused more attention on the special case of CNTs structure; the reason is because the beauty and perfection of their mathematical description and the resulting extraordinary mechanical and (ballistic) electron-transport properties.

Structures oriented perpendicular to the substrate on which they are grown are commonly called vertically aligned. In case of nanofibers or nanotubes, this means that they are straight and their axes are normal to the substrate (fig. 2). In contrast, synthesis methods such as arc-discharge, laser ablation, chemical vapour deposition (CVD) with floating catalyst produce non-aligned, entangled ropes of nanotubes. The CNT material produced this way can be used for a variety of applications such as reinforcement of composite materials, hydrogen storage, catalyst support, etc. However, for many applications that utilize nanofibers and nanotubes as individual elements (nanoelectronics), tedious manipulations on a microscale are often required if such entangled material is to be used. Accordingly, synthesis of aligned structures at defined positions on a substrate is preferred. Vertically aligned carbon nanofibers and carbon nanotubes can be prepared as a dense mat ("forest") or as individual freestanding structures (often arranged in regular arrays), as can see in figure 2. Vertical alignment in very dense forests is provided by Van der Waals interaction between nanotubes or nanofibers that keeps them aligned, while isolated elements may be aligned by interaction of the growing nanofiber with an electric field.
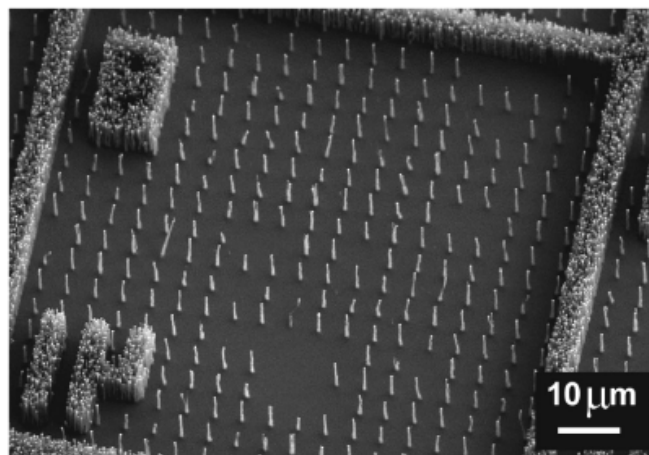
Figure 2. SEM image of regular arrays of freestanding VACNFs and forests of VACNFs. Catalyst definition was produced by photolithography. VACNFs were grown by dc C-PECVD [4].

2.2   Experimental techniques

As previously described, in order to characterize our systems we used different techniques and consequently different experimental apparata. In the following picture these apparata are shown together with their main characteristics.

Advanced Microscopy Laboratory

Physics Department at University of Calabria (Italy)

SEM Microscopy
Quanta FEG 400 (FEI).

TEM Microscopy
Leo 922 Omega HR (Assing,Zeiss)

➢ EDX Tecnique : Micro-analysis

➢ e-SEM mode: *environmental-*SEM
(from UHV to 1.3 mbar)

**Possibility to work in humid environment
and with soft materials**

➢ E : 0 – 200 KeV

➢ Δx = 2 Å

➢ *EELS-TEM*

Electronic Structure
of the Conduction Band

Scanning electron microscopy (SEM) is the best known and most widely-used of the surface analytical techniques [22]. SEM, accompanied by X-ray analysis, is considered a relatively rapid, inexpensive, and basically non-destructive approach to surface analysis. It is often used to survey surface analytical problems before proceeding to techniques that are more surface-sensitive and more specialised. High resolution images of surface topography, with excellent depth of field are produced using a highly-focused, scanning (primary) electron beam. The primary electrons enter a surface with an energy of 0.5 - 30 keV, and generate many low

energy secondary electrons. The intensity of these secondary electrons is largely governed by the surface topography of the sample.

An image of the sample surface can thus be constructed by measuring secondary electron intensity as a function of the position of the scanning primary electron beam. High spatial resolution is possible because the primary electron beam can be focused to a very small spot (< 10 nm). High sensitivity to topographic features on the outermost surface (< 5 nm) is achieved when using a primary electron beam with an energy of <1 keV. In addition to low energy secondary electrons, backscattered electrons and X-rays are also generated by primary electron bombardment.

The intensity of backscattered electrons can be correlated to the atomic number of the element within the sampling volume. Hence, some qualitative elemental information can be obtained. The analysis of characteristic X-rays emitted from the sample gives more quantitative elemental information. Such X-ray analysis can be confined to analytical volumes as small as 1 cubic micron.

- ➢ *e-SEM:* The Scanning Electron Microscope we used (Quanta FEG 400 (FEI)) operates in the e-SEM mode, that is *environmental*-SEM, and allows to operate in very low vacuum conditions (≤ 20 Torr) with the possibility to collect secondary electron with an appropriate detector (GSED). The gas ionization process on the sample allows the compensation of the charge product by the electron beam on the surface. In this way it is possible to analyze also non conductive sample without a pre-metallization. Moreover, operating in a relative *high* pressure permits to study sample with a high content of volatile substances, like water, polymer and etc. Cooling the sample close to or below 0°C is possible to work in a condition of 100% relative humidity.

Transmission electron microscopes (TEM) allow to obtain, on a thin sample (< 0.1 micron), high resolution images (Δx = 2 Å). It has some similarities with the ordinary optical microscope: an incident electron beam passes through a very thin sample and projects an image on a fluorescent screen or a CCD sensor.

The electrons are generated by a tungsten filament or a Lanthanum Hexaboride (LaB_6) source and accelerated up to several hundreds keV and focuses on a submicrometric region by a complex series of electromagnetic lenses, usually from six to eight, consisting of electromagnetic windings arranged symmetrically compared to the incident beam. The electron beam is produced and shaped in Ultra High Vacuum (UHV) conditions generated by both turbomolecular and ion pumps.

The beam passing through the sample is focused by an objective lens on a fluorescent screen (or CCD detector), giving rise to a much larger image. By using this apparatus it is possible to obtain a morphological and electronic characterization in the nanometre scale.

> ➤ ***EELS-TEM:*** Our apparatus, a Leo 922 Omega HR by Assing-Zeiss, is equipped with a high energy electron beam source (up to 200 keV) and with an energy filter (an in-column OMEGA filter) that allows to obtain images from electron that interact inelastically with the sample. Therefore we can associate the morphological information to the EELS information obtaining structural, chemical and electronic combined information [20].

BeamLine SpectroMicroscopy

Elettra Synchrotron Light Source – Trieste (Italy)
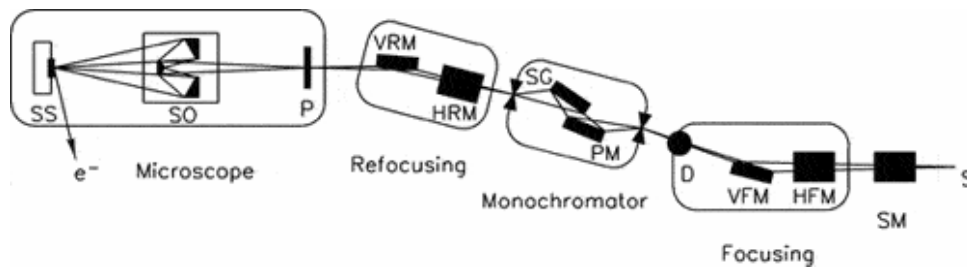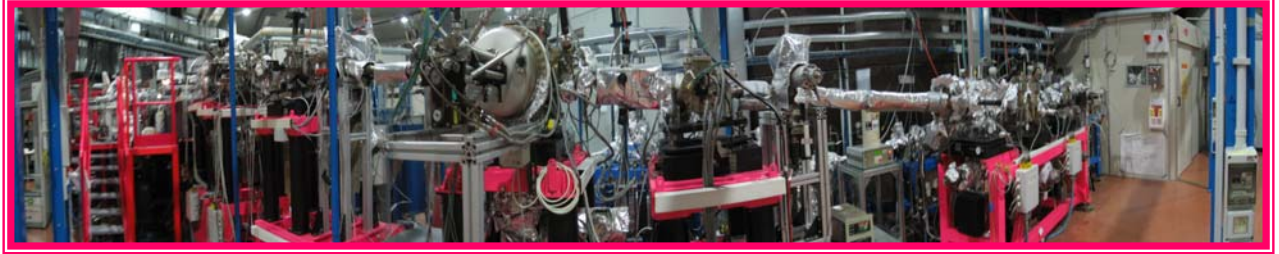
BeamLine SpectroMicroscopy up. On the left schematic representation of the BeamLine

* SS: scanning stage - SO: schwarzschild objective
  P: pinhole - VRM: vertical refocusing mirror
  HRM horizontal refocusing mirror
  SG: spherical grating - PM: plane mirror
  VFM: vertical focusing mirror
  HFM: horizontal focusing mirror
  S: source

Ultraviolet Photoelectron Spectroscopy (UPS)

✦ *The photoelectric effect*

The photoelectric effect is the physical phenomenon on which the photoelectric spectroscopies are based: a sample, irradiated by photons of energy *hν*, emits electrons from his bound states into free states whose kinetic energy is given by the difference between the photon energy and the electron binding energy in the sample [25]. The basic formula is

$$E_{kin} = h\nu - E_B$$

where E_{kin} is the kinetic energy of the emitted "photoelectron", *hν* is the photon energy and E_B is the electron binding energy.

If the photon energy is high enough and the emitted electron final states isn't discrete, there are no selection rules prohibiting any kind of transition, and

every electron bounded state will be able to be excited. We can measure the electron binding energy E_B by knowing the photon energy and measuring the photoelectron kinetic energy.

Figure 3 shows schematically how the energy-level diagram and the energy distribution of photo-emitted electrons relate to each other in the case of a solid sample. The solid sample has core levels and a valence band. In the present case of a metal, the Fermi energy E_F is at the top of the valence band and has a separation W_0 from the vacuum level E_{vac}. If photoabsortion takes place in a core level with binding energy E_B ($E_B = 0$ at E_F) the photoelectrons can be detected with kinetic energy $E_{kin} = hv - W_0 - E_B$ in the vacuum. If the energy distribution of the emitted electron is plotted as in figure 3, their number per energy interval often gives a replica of the electron-energy distribution in the solid [26]. This is an attractive feature of photoelectron spectroscopy: it is able to provide information on the electron energy distribution in a material.
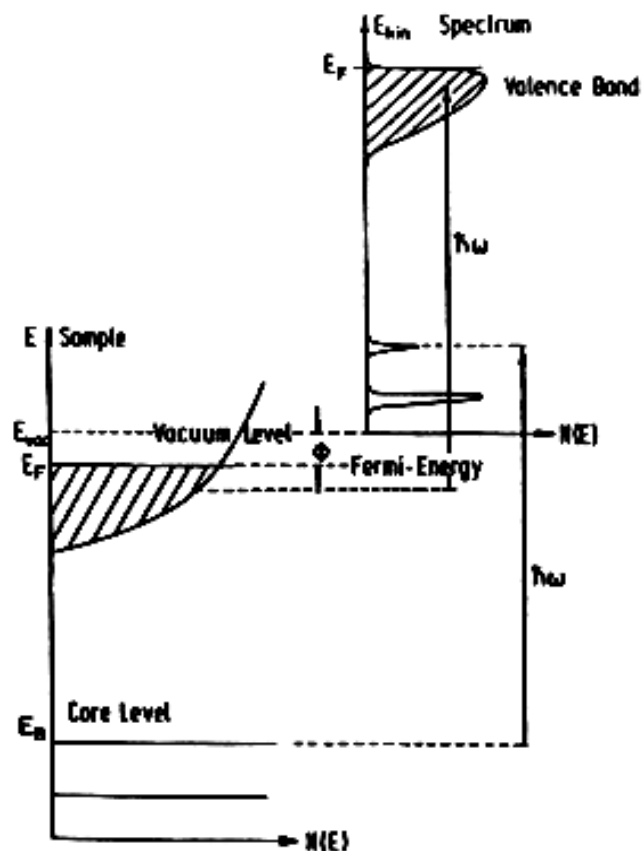
Figure 3. Schematic of a metal sample electronic structure, and the relative photoelectron spectrum in case of core levels excitation and valence band states excitation.

An UPS apparatus consist of a radiation source, a sample chamber and an emitted electron analyser (see fig. 4).
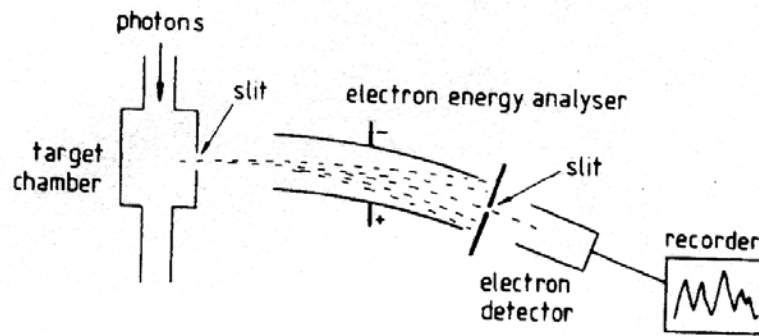
Figure 4. Setup of a photoelectron spectroscopy experiment.

A widely used radiation source is the synchrotron light source: electrons, circulating in circulars orbits, emit a radiation with the following unique features.

1) wide spectral range

2) highly focused radiation

3) polarized radiation

4) pulsed radiation at high frequency

The emitted radiation has energy between the infrared and hard X-rays, and then suitable monochromators must be used to select the right photon energy.

The beam amplitude is around 0.1 eV in the range 10-1000 eV with a typical flux of 109-1011 ph/s.

The ultraviolet photoelectron spectroscopy uses photons whose energy falls in the UV region of the electromagnetic spectrum: 5-500 eV. The X-ray photoelectron spectroscopy uses photon at higher energy. Ultraviolet light usually permit an higher spectral resolution respect the X-rays.

    Valence band determination by UPS

Comparing to other techniques UPS gives information on low intensity and delocalised electrons bindings. With a low photon energy (10-100 eV) only the valence band state and possibly high lying core levels are probed. The mean free path of electrons in solids determine the probing depth. It varies between 0.5 nm for kinetic energy of E_k = 50 eV to 3 nm for E_k = 1.5 keV. The small probing depth requires ultrahigh vacuum instruments to prevent surface contamination. The UPS is sensible to the sample surface but it isn't specifically a surface technique.

A valence band photoelectron spectrum resembles a one-electron density of states curve. However they are not identical. In fact the spectrum represent the emission from an excited state, and many body effects provide screening of the photon-hole, moreover the emission of electrons with different quantum numbers is strongly dependent from the electron-photon cross-section. Within some approximation, photoelectron spectrum gives directly the position and the width of the occupied electronic bands. The variation of the emission at the Fermi level accounts directly for changes in the density of states at the Fermi level [27]. The electron-photon cross section is strongly dependent from the electron states (quantum numbers) and the photon energy. Using photon at various energies the evaluation of the partial density of states is to some extent possible.

The Spectromicroscopy beamline at ELETTRA is designed to perform photoemission experiments with high spatial resolution, which is obtained by focusing the radiation in a small spot on the sample by means of a multilayer-coated Schwarzschild Objective. Three objectives are currently available; these operate at photon energies of 74, 95, and 110 eV. The smallest achievable spot size is currently 0.5 micron. At present, the limit to the spatial resolution is due to aberrations caused by figure errors of the objective. Typical counting rates in photoemission spectra, for example, on the Au 5d peak, are of the order of 10^4-10^5 counts per second with an energy resolution of the order of 100-200 meV.

A controlled temperature range (40-400 K) is available too. The SpectroMicroscopy beamline comprises the monochromator and the microscope joined at the pinhole "P". The source is the U12.5 undulator mounted at the 3.2 section of ELETTRA and shared with the VUV Photoemission beamline. The beamline is based on a variable angle spherical grating monochromator with two gratings optimized for two photon energies engaged. Besides the monochromatization action, the beamline performs a predemagnification of the X-rays by forming a focused image of the source at a pinhole "P" placed at the beginning of the microscope section of the beamline (size = 6 µm H x 4 µm V).

Ultra High Vacuum Chamber

Surface Electron Spectroscopy (SPES) Group
**Physics Department at University of Calabria (Italy)**
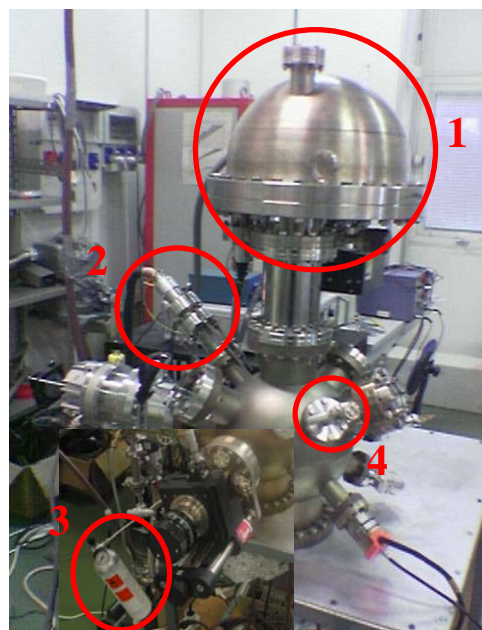
UHV Chamber

EELS: Electron Energy Loss Spectroscopy – Losses for single particle and collective excitations

AES: Auger Electron Spectroscopy – Line shapes study for chemical and electronic surface analysis

1. *CHA Analyzer (VSW)*:

    ➢ CHA = Electrostatic Concentric Hemispherical Analyser (R_0 = 100 mm)

    ➢ Power Supply: HAC 5000 (0 – 5000 Volts)

    ➢ Pass Energies E_0: 10 eV, 22 eV, 44 eV

    ➢ Energy resolution: $\Delta E/E_0$ = 0.025

2. *Electron Gun VSW EG5:*

    ➢ Beam lateral dimension = ~ 250 μm

    ➢ Beam energy = 0 - 3000 eV

    ➢ Energy resolution ≤ 1.0 eV

3. *Gas Line:* CO, O_2

4. *Metal Evaporation Source:* Gold filament on W wire.

5. *Home-made sample-holder*. The sample holder was locally assembled in order to mount a sample of different dimension (from 1 to 10 mm). All the sample holder is made out using Tantalum (Ta) so the stage can reach high temperature compatible with the CNTs growth process reducing the problems as outgassing and melting. In the inset of the following picture it is possible to observe the thermocouple mounting. Using it, we have a better control on the sample's temperature: it is monitored on the sample back, while its front was monitored with a pyrometer external to the UHV system.
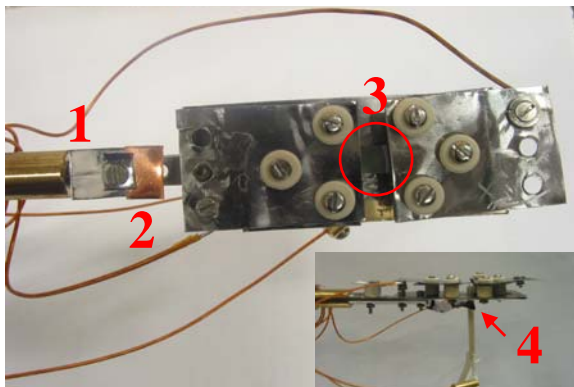
1. ***Fluorescent target***: Used to monitor the electron beam position

2. ***Copper target (Cu)***: Used to maximize the signal

3. ***Sample***: Silicon Carbide before treatment

4. ***Thermocouple***: Used to measure the temperature of the sample on the back.

The picture shown below depicts some steps of the heating procedure used during the growth of aligned CNTs on SiC wafers. As it can be clearly observed, the mounting allows a uniform heating at different temperatures by electrical current flow through the sample (see Par. 3.3)
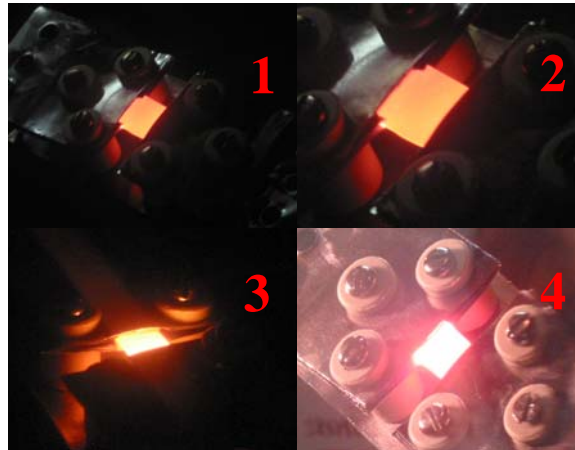
❖   *Snapshots of the heating process. The heating is very uniform. Picture 4 shows the last step before the higher temperature step (~1500°C)*

Bad mechanical contacts between the sample and the two tantalum slabs lead to the formation of hot points and a consequent not homogeneous sample temperature as depicted from the picture below. We can observe on the left side two bright spots indicating a higher temperature compared with the rest of the sample.
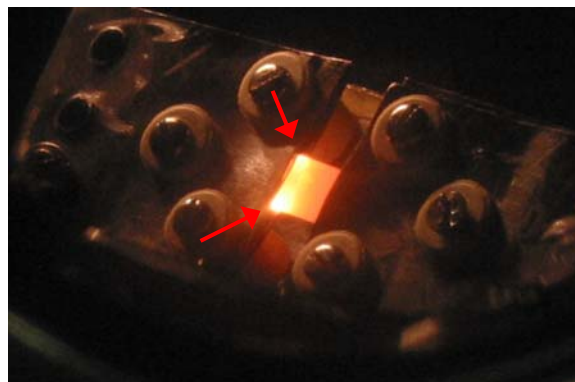
Electron Energy Loss Spectroscopy (EELS)

EELS (Electron energy loss spectroscopy) is an experimental technique that permit the study of materials through the analysis of their electronic and vibrational excitations.

In this spectroscopy, a monochromatic electron beam is sent to the surface of a solid material, these primary electrons are partially unelastically scattered and their kinetic energy distribution is analyzed using an electron energy analyzer [17], the energy losses are due to the excitation of electronic and vibrational transition of the investigated materials and so provide a tool for analysing them.

The EELS technique can be used in various configurations by changing the geometrical and physical parameters. For example different spectra and information can be obtained by changing the electronic energy or the incidence angle of the impinging primary beam, or the angle of analysis of diffused electrons [18,19].

Energy losses are due mainly to three processes:

1) excitations of network vibrations of atoms on the clean surface (optical phonons surface, acoustic phonons surface) and / or vibrations of atomic and molecular species adsorbed on the surface;

2) excitations of valence band transitions that can be divided into single particles electronic excitations (inter-band and intra-band excitations) and collective excitations (surface, volume and interface plasmons);

3) excitations of core levels electrons to conduction band levels.

The mentioned excitations hold a very large energy range, which extends from around tens meV (for phonons) up to a few thousands eV [17] needed to excite core electrons to states above the Fermi level.
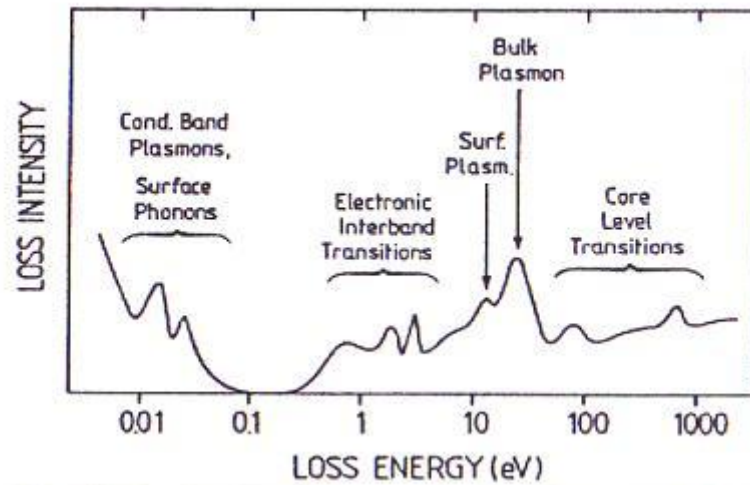
Figure 5. Excitations mechanisms that can contribute to the EELS spectra.

This type of spectroscopy allows us to obtain information on both the occupied and empty electronic density of states in a solid [20]. A primary beam of kinetic energy Ep ≥ 50 eV is suited to investigate plasma excitations of valence band electrons electronic inter-band and intra-band transitions and excitations of core levels electrons to conduction band levels.

A primary energy with Ep ≤ 50 eV is instead usually employed for study vibrational excitations because the reachable higher energy resolution.
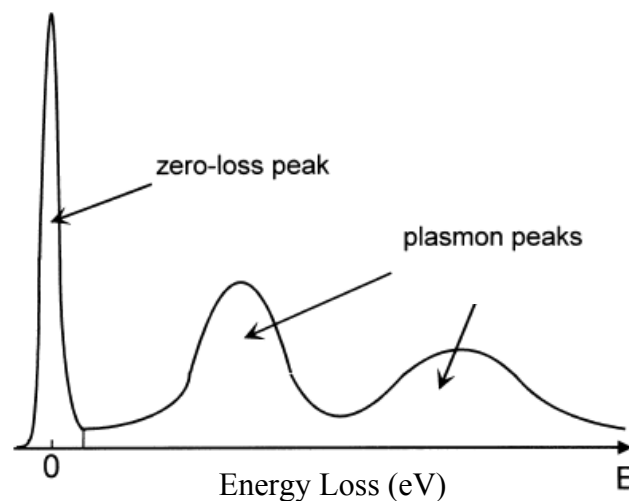
Figure 6. Typical EELS spectra in the range of some ten eV

Auger spectroscopy (AES)

The Auger spectroscopy (AES) is one of the standard techniques for the analysis of surfaces. It was in the past used primarily to verify the degree of cleaning of surfaces prepared under ultra-high vacuum. But possible applications include studies of the chemical bond and determination of the chemical composition of surfaces through a quantitative assessment of all the elements present.

A sufficient energy perturbation (photons, electrons and ions with energy greater than a few hundreds eV) can ionize a multi-electron atom ($Z > 2$) creating an "hole" in an internal level (K, L, ...). The ionized atom electronic structure adjust so that an electron falls from one higher energy level to fills the initial hole in the deep core level. This transition can be accompanied from the emission of a photon with energy corresponding to the energy difference between the initial and final state (fluorescence emission − see fig. 7). Alternatively, the process can involve only electrons (non radiative disexcitation − see fig. 7) and the energy gained by filling up the hole is transferred to another electron that acquires sufficient energy to leave the atom.

The phenomenon, which leaves a doubly ionized atom (two holes in a same or different core levels), is named Auger process [21] by the name of the French physicist Pierre Auger who first postulated their existence. An Auger electron has a kinetic energy similar to the characteristic fluorescence photon energy, but because of the processes involves many bodies interaction, it is not identical. Indeed, for the Auger process the final state atom is doubly ionized and therefore the energy differs from the final state of fluorescence decay.

Both processes (fluorescence and Auger decay) are possible, but in the case of light atoms ($Z < 30$), the second process is more likely than the first.

Because the Auger electron is characterized by a well-defined kinetic energy, which is directly connected to the difference between the energy of core levels involved in the transition, measures of this energy can be used to identify the particular atom. Indeed, the Auger electrons are emitted in discrete energy values which are characteristic of the various elements on the surface.

It is, therefore, possible to make a quantitative analysis of chemical elements in a way similar to what happens with the use of fluorescence techniques, even if the AES is much more sensitive to surface.

The Auger electrons are classified according to energy levels involved in their production. For example, if the hole created in the level K is occupied by an electron belonging to L_1 with the release of an electron from level L_3, then the Auger transition is marked with the notation KL_1L_3.
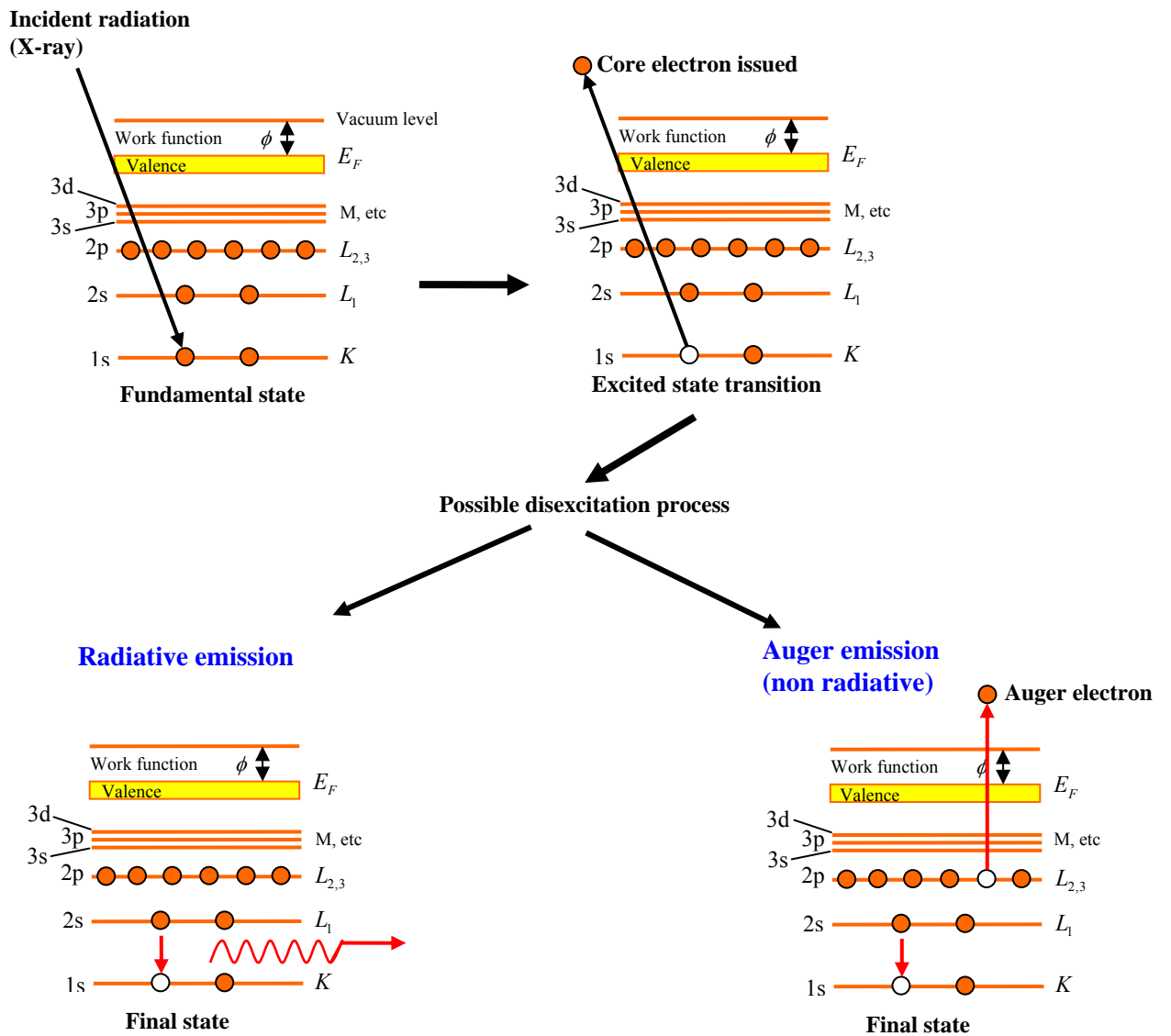

Figure 7. Possible disexcitation process with radiative or Auger emission.

Raman

Lycril Laboratory

Physics Department at University of Calabria (Italy)

Raman microprobe Jobin-Yvon Labram equipped with a Charge Coupled Device (CCD) detector. The low frequency detection limit, due to the notch filter, is at about 190 cm^{-1}. The power of the He–Ne laser (632.8 nm emission) out of the objective was about 5 mW and the laser spot size was about 2–3 μm. To avoid unwanted laser-induced transformations, neutral filters of different optical densities (OD) are available.

Element	*Characteristics*
Laser	HeNe 17mW laser, polarised 500:1 with wavelength 632.817 nm
Holographic Notch Filter	Super Notch Plus used a dichroic mirror. Drop off Stokes edge <120cm^{-1}; Now 200 cm^{-1}.
Confocal hole	Adjustable between 0 and 1500 μm (scaled on the sample by a factor: 1.4xObjective magnification)
Microscope	High stability BX40. Focus graduation 1 μm. Objectives 10x NA 0.25, 50x NA 0.7, 100x NA 0.9. Other objectives available (Long work distance 20x, 50x). Illumination by transmission and reflection for opaque samples. Macro adapter for mounting of macro 40 mm objective under microscope. Colour camera for the observation of the sample.
External Lasers available and Laser entrance	(notch exchange is required) Ar$^+$, 457.8, 514.532 nm, Kr$^+$ 647.1, 752,5 nm, Yag doubled, diode pumped 532 nm, Laser diode 785 nm. Removable mirrors for external Laser. HeNe beam can be directed externally through the external laser entrance for easier external laser alignment.
Spectrograph	Stigmatic 300mm focal length spectrograph. Two gratings mounted on the same shaft 1800 g/mm (holographic) and 600 g/mm (ruled or holographic). Sinus arm drive. Laser diode for alignment.
CCD Dector	Peltier cooled 1024×256, 16 bit dynamic range (pixel size 27 μm).
Computer	Labspec software and VITEC video card for TV image digitalisation.
Separated electronic box	Alimentation of the Laser, drive of hole, slit, gratings, shutters, scanners, alimentation of the Laser diode for alignment.
Options	Motorised XY microscope stage for point by point or laser scanning imaging. Resolution 0.1 μm, reproducibility 1 μm. Raman 90×60 mm. Y piezo table for imaging with laser scanning (X direction), range 100 μm. ″PIFOC″ Z-actuator for automatic focusing of microscope objective or z-scanning (range 0-100 μm). Autofocus device for microscope objective (correction of focus between + / -5 μm). Temperature controlled cells. Set of filters (notch + interferential) for external laser.

Raman Spectroscopy

The Raman Effect and Raman Scattering

When light passes through any material the photons will interact with the material molecules and most of them will be elastically scattered with same energy as the incident photons by the process named the Rayleigh scattering. However, a small fraction of photons (approximately 1 in 10^6 photons) is scattered at energies different from the incident photon energy. The process leading to this inelastic scatter is termed the Raman effect, after it was documented in 1928 by Sir C.V. Raman. Raman scattering can occur with a change in vibrational, rotational or electronic energy of a molecule [28]. In this discussion we are primarily interested with the vibrational Raman effect. The difference in energy between the incident photon and the Raman scattered photon is equal to the energy of a specific vibration of the scattering molecule. A plot of intensity of scattered light versus energy difference is a Raman spectrum.

The Scattering Process

The Raman effect arises when a photon incises on a molecule and interacts with the electric dipole of the molecule. In classical terms, the interaction can be viewed as a perturbation of the molecule electric field. In quantum mechanics the scattering is described as an excitation to a virtual state with nearly coincident de-excitation and a change in vibrational energy. The virtual state description of scattering is shown in figure 18.

As illustrated in the simplified energy level diagram, an unperturbed molecule is in the ground vibrational and electronic states. The electric field of the laser raises the energy of the system for an instant to a no true energy state which returns to the initial ground state (Rayleigh scattering). Relaxation to the first excited vibrational level can also occurs: this result in the so called Stokes-Raman shift [29]. Stokes-Raman shift scattered photon is of lower energy (longer wavelength) than that of the incident laser. If the molecule resides in an exited vibrational level (due to thermal excitation), relaxation to the ground state is possible, producing

scattered photon of higher energy (shorter wavelength) than that of the laser light: this scattering is called anti-Stokes-Raman scattering.
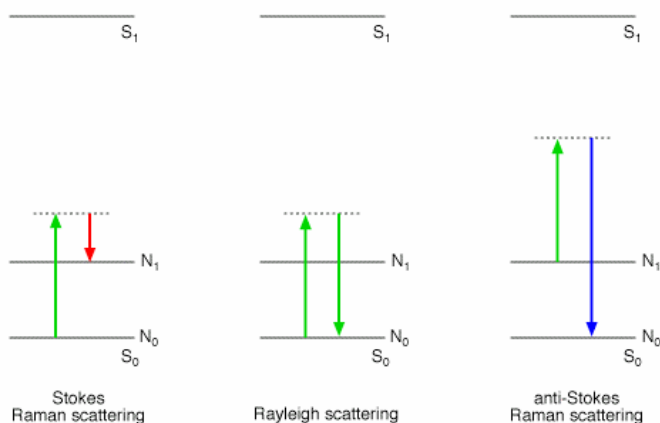
Figure 18. Energy level diagram for scattering by a molecule; (a) Stokes Raman scattering (b) Rayleigh scattering (c) anti-Stokes Raman scattering, S_0 and S_1 are the ground and excited electronic molecular states, N_0 and N_1 are the ground and exited vibrational molecular states.

The energy shift between the incident and scattered photons is usually given as wave numbers (cm^{-1}), and is calculated through the equation

$$\bar{\nu} = \frac{1}{\lambda_{incident}} - \frac{1}{\lambda_{scattered}}$$

in which $\lambda_{incident}$ and $\lambda_{scattered}$ are the wavelengths (in cm^{-1}) of the incident and Raman scattered photons, respectively.

At room temperature the thermal population of vibrational excited states is low, although not zero. The anti-Stokes signal has a lower intensity than the Stokes signal. Therefore, the Stokes shifted scatter is what is usually observed in Raman spectroscopy.

Raman Frequencies and Selection Rules

A simple classical electromagnetic field description of Raman spectroscopy can be used to explain many of the important features of Raman band intensities. The dipole moment, P, induced in a molecule by an external electric field, E, is proportional to the field as shown in equation.

$$\mathbf{P} = \alpha\,\mathbf{E}$$

The proportionality constant α is the polarizability of the molecule, or, more precisely, the polarizability tensor.

Raman scattering can occur because a molecular vibration can change the polarizability: a normal vibration is described by a normal coordinate q_k. and a normal frequency v_k:

$$q_k = q_k^0 \cos(2\pi v_k t)$$

The polarizability can be modulated by a normal vibration, as shown in following expression:

$$\alpha_k = \alpha_0 + \left[\frac{\partial \alpha}{\partial q_k}\right]_0 q_k^0 \cos 2\pi v_k t + \cdots$$

The change is described by the polarizability derivative, $\frac{\partial \alpha}{\partial q_k}$, where q_k is the normal coordinate of the vibration. The selection rule for a Raman-active vibration is then given by $\frac{\partial \alpha}{\partial q_k} \neq 0$

The symmetry of the molecule determine if such condition is fulfilled: an allowed transition is said Raman active, instead a forbidden transition is said Raman inactive [28].

With an incident electric field $E = E_0 \cos(2\pi v_0 t)$, the resulting expression for the oscillating molecular electric dipole is:

$$p_k = \alpha_0 E_0 \cos(2\pi v_0 t) + \frac{1}{2}\left(\frac{\partial \alpha}{\partial q_k}\right)_0 q_k^0 E_0\left[\cos(2\pi(v_0 - v_k)t) + \cos(2\pi(v_0 + v_k)t)\right]$$

This oscillating dipole, emits electromagnetic radiation at various frequency. The first term describes the elastic Rayleigh scattering, the second term the Stokes Raman scattering, and the third the anti-Stokes Raman scattering. This classical equation, however, does not show the individual intensities of Stokes and anti-Stokes Raman lines which are only provided in a quantum mechanical interpretation of the Raman-effect, by considering the relative population of the ground and excited molecular vibrational states.

- *Experimental determination of a Raman spectrum.*

In a Raman experiment the sample is irradiated with strong monochromatic light sources, the scattered radiation is detected and the Raman spectrum is plotted as the intensity of the scattered light versus the scattered light frequency. This is schematically illustrated in figure 8.
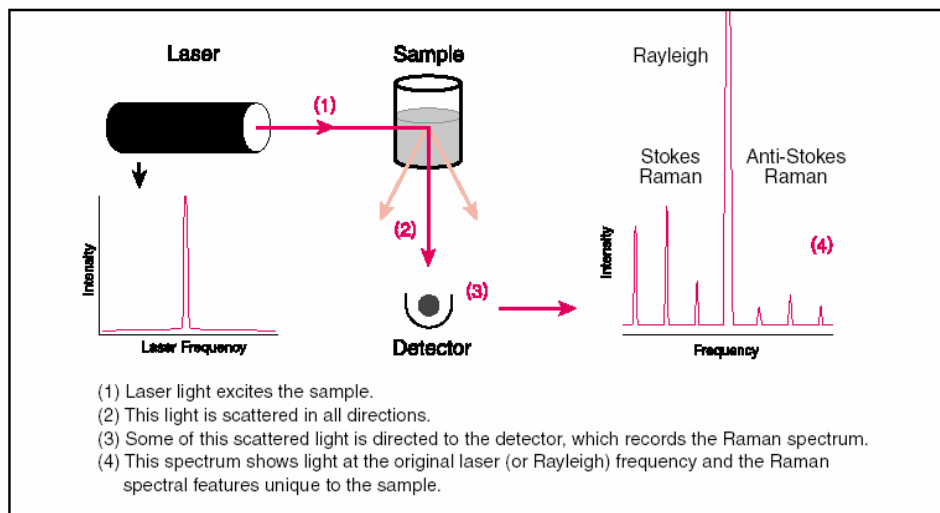
Figure 8. Scheme of a Raman spectroscopic experiment.

The Raman signal is usually of small intensity, so the use of Raman spectroscopy as an analysis tool has became possible only with the availability of strong monochromatic light source (laser sources), the availability of holographic notch filters and of more sensitive Charge Coupled Devices (CCDs).

Raman spectrometers employ dispersive technologies for the collection of spectra. In Figure 9 is illustrated the detector part of a dispersive Raman apparatus. Before entering the detector stage a notch filter cut-off the intense light scattered at the same frequency of the incident radiation. The scattered light is then focused on a grating which spatially separates the individual wavelengths that made Raman spectrum. The spatially dispersed beam is directed to a CCD that, at each wavelengths, gives the signal intensity.
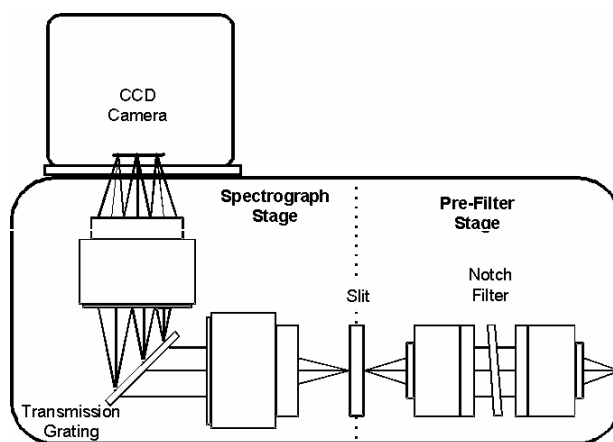
Figure 9. *Scheme for the detector part of a Raman apparatus.*

Raman spectroscopy is usually coupled with a microscope that allows spatial analysis of the samples. The highest spatial resolution is attained using small pinholes or "apertures" somewhere in the microscope. Usually dispersive Raman microscopy offers spatial resolution below 1 μm (called micro-Raman apparatus).

Raman Spectroscopy Applications

Vibrational spectroscopy provides key information on the structure of molecules. For example, the position and intensity of features in the vibrational spectrum can be used to study molecular structure or determine the chemical identity of the sample. It is possible to identify the chemical compounds or to study intermolecular interactions by observing the positions and intensity of the Raman bands.

STM/STS

Physics Department at University of Calabria (Italy)
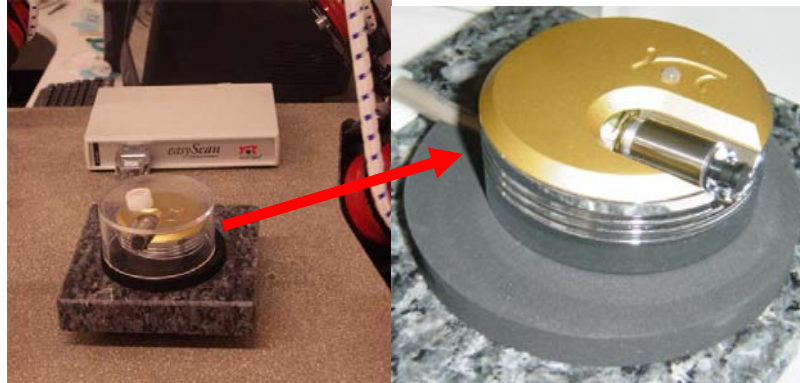
Schaefer STM/STS specifications

- ✓ Maximum XY-Scan range   typ. 0.5/1 μm
- ✓ Maximum Z-range   200 nm
- ✓ Drive resolution Z   0.003 nm
- ✓ Drive resolution XY   0.015 nm
- ✓ Gap voltage   ±10 V in 5 mV steps
- ✓ Set point current   ±100 nA in 25 pA steps
- ✓ Sample size   max. 10 mm diameter

The ***Scanning Tunneling Microscopy (STM)*** was the first instrument to generate real-space images of surfaces with atomic resolution.

STMs use a sharpened, conducting tip with a bias voltage applied between the tip and the sample. When the tip is brought within about 10Å of the sample, electrons from the sample begin to "tunnel" through the 10Å gap into the tip or vice versa, depending upon the sign of the bias voltage (see fig. 10). The resulting tunneling current varies with tip-to-sample spacing, and it is the signal used to create an STM image. For tunneling to take place, both the sample and the tip must be conductors or semiconductors. Unlike AFMs, STMs cannot image insulating materials.
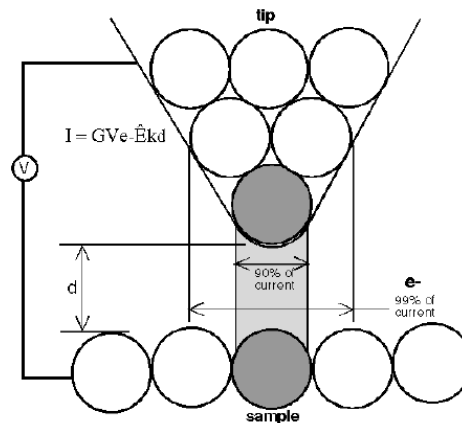
Figure 10. Schematic of tip and sample interaction for STM.

The tunneling current is an exponential function of distance; if the separation between the tip and the sample changes by 10% (on the order of 1Å), the tunneling current changes by an order of magnitude. This exponential

dependence gives STMs their remarkable sensitivity. STMs can image the surface of the sample with sub-angstrom precision vertically, and atomic resolution laterally [24].

STMs can be designed to scan a sample in either of two modes: *constant-height* or *constant-current* mode, as shown in figure 11. In constant-height mode, the tip travels in a horizontal plane above the sample and the tunneling current varies depending on topography and the local surface electronic properties of the sample. The tunneling current measured at each location on the sample surface constitute the data set, the topographic image.

In constant-current mode, STMs use feedback to keep the tunneling current constant by adjusting the height of the scanner at each measurement point. For example, when the system detects an increase in tunneling current, it adjusts the voltage applied to the piezoelectric scanner to increase the distance between the tip and the sample.

In constant-current mode, the motion of the scanner constitutes the data set. If the system keeps the tunneling current constant to within a few percent, the tip-to-sample distance will be constant to within a few hundredths of an angstrom.

Each mode has advantages and disadvantages. Constant-height mode is faster because the system doesn't have to move the scanner up and down, but it provides useful information only for relatively smooth surfaces.

Constant-current mode can measure irregular surfaces with high precision, but the measurement takes more time.
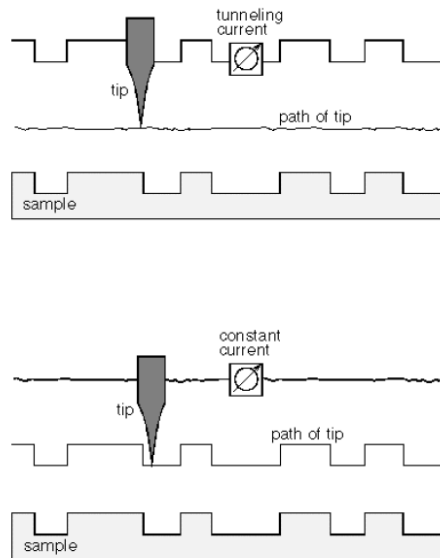
Figure 11. Comparison of constant-height and constant-current mode for STM.

As a first approximation, an image of the tunneling current maps the topography of the sample. More accurately, the tunneling current corresponds to the electronic density of states at the surface. STMs actually sense the number of filled or unfilled electron states near the Fermi surface, within an energy range determined by the bias voltage. Rather than measuring physical topography, it measures a surface of constant tunneling probability.

The sensitivity of STMs to electronic structure can be a tremendous advantage. Other techniques for obtaining information about the electronic properties of a sample detect and average the data originating from a relatively large area, a few microns to a few millimetres across. STMs can be used as surface analysis tools that probe the electronic properties of the sample surface with atomic resolution.

Scanning tunneling spectroscopy (STS) studies the local electronic structure of a sample's surface. The electronic structure of an atom depends upon its atomic species and also upon its local chemical environment (how many neighbors it has, what kind of atoms they are, and the symmetry of their distribution). STS encompasses many methods: taking "topographic" (constant-current) images using different bias voltages and comparing them [23]; taking current (constant-height) images at different heights; and ramping the bias voltage with the tip positioned over a feature of interest while recording the tunneling current. The last example results in current vs. voltage (I-V) curves characteristic of the electronic structure at a specific x,y location on the sample surface. STMs can be set up to collect I-V curves at every point in a data set, providing a three-dimensional map of electronic structure. All of these are ways of probing the local electronic structure of a surface using an STM.

2.3 Analyzed systems

We characterized different kind of Carbon-based nanostructured systems in order to compare them and get a deeper understanding on their interlinked properties. The analyzed systems are:

- ✓ Single Wall Carbon Nanotubes produced by Catalytical Chemical Vapor Deposition (SWCNTs by CCVD) at the University of Ioannina (GR)

- ✓ Functionalized Carbon Nanotubes (f-CNTs) produced at the University of Ioannina (GR)

- ✓ Carbon Nanotubes grown by Silicon Carbide surface decomposition (CNTs by SiC)

- ✓ Tin filled Carbon Nanotubes (Sn@CNTs) produced at the University of Ioannina (GR)

- ✓ Carbon Nanocolumns (Nc-C) produced at the IMM/CNR Institute in Catania (I).

Among the several methods used for the growth of CNTs, thermal CVD is an efficient, versatile and simple technique: the growth of carbon nanostructures employs a carbon precursor molecule and transition metal as catalyst. Since this procedure is performed at relative low temperature (lower than 1000°C) as compare with other techniques, it becomes more attractive, being compatible with other technologies involved in the preparation of electronic devices.

By changing the experimental conditions in catalytic CVD, CNTs presenting significant structural differences such as straight, curved or helical shapes, can be obtained [7,8].

In the present work we will show results on SWCNTs, double wall CNTs (DWCNTs), f-CNTs, and Sn@CNTs produced by Chemical Vapour Deposition; each one is connect with different growth conditions as we will discuss in the following.

We will present the analysis of the Nc-C system produced by RF-Magnetron sputtering from IMM-CNR of Catania (see Par 1.1, 3.5). We studied this system for comparison with the other carbon based nano-systems.

A second technique employed in production of aligned CNTs makes use of the SiC surface decomposition (see Par. 3.3). Silicon Carbide, the only chemical compound of carbon and silicon, is composed of tetrahedra of strongly bonded carbon and silicon atoms. Consequently, SiC is a very hard and strong material, not attacked by any acids or alkalis or molten salts up to 800 °C. In air, SiC forms a protective silicon oxide coating at 1200 °C and does not decompose up to 1600 °C. It is considered a promising compound semiconductor material for high-temperature, high-power, and high-frequency electronic devices [9,10] due to its high breakdown field (2.3 x 10^6 V/cm), high thermal conductivity (4.9 W/(cm K)), high saturated electron field velocity (2 x 10^7 cm/s), relatively large energy band gap, and chemical stability [10]. Furthermore, its low density, high strength, excellent thermal shock resistance etc, allows its use in a large variety of applications, like abrasives, refractories, ceramics, wafer tray support, puddles in semiconductor furnaces, etc.

From a crystallographic point of view, SiC is very well known as a material because of the *polytypism* phenomenon, i.e. different crystal structures in one-dimensional variation with the same chemical composition. In fact, the variation of occupation sites along the c-axis brings different crystal structures named polytypes. In Ramsdell's notation, polytypes are represented by the number of layers in the unit cell and the crystal system (C for cubic, H for hexagonal, and R for rhombohedral). Illustrations of several common polytypes are shown in figure 24 [10].
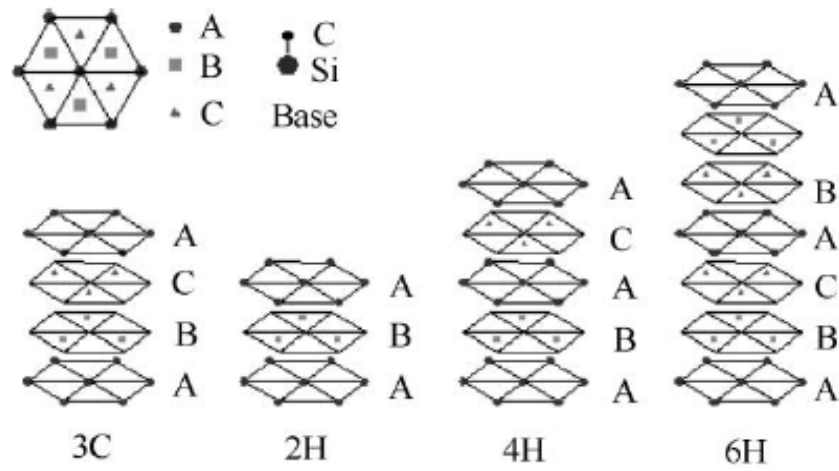
Figure 24. Stacking order illustration of several common SiC polytypes [10].

We make use of sample, C face polish, produced by CREE Materials. We produced CNTs by heating a 6H-SiC sample in Ultra High Vacuum conditions up to 1500 °C. The result are well aligned and very close packed carbon nanotubes (see Par. 3.3). This is a very interesting achievement because there is no need of metal catalyst particles (necessary in all the other growth processes).

3. Results survey

3.1 Single Wall Carbon Nanotubes by Catalytically enhanced Chemical Vapor Deposition (SWCNTs by CCVD)

3.1.1 State of the art

The fabrication in sufficient quantities and at a low cost of well-defined and organized arrays of carbon nanotubes is of high importance owing to their unique properties associated to the nano-scale structure and the resulting wide range of applications [1]. Nowadays, the three most widely used methods for their synthesis are arc discharge [2-4], laser vaporization [5-7] and catalytical chemical vapour deposition (CCVD) [8-11]. The latter appears to be the most promising one to scale up single- [12, 13], double- [14, 15] and multi-wall carbon nanotubes [16, 17] production at low cost [18] using simple apparatus operating at relative low temperatures (500-1000 ^{o}C) compared to the former two [19]. Moreover, the CCVD method offers the opportunity to control and adjust multiple structural parameters of the synthesized carbon nanostructures such as diameter [20, 21] (and therefore chirality [13]), length [22, 23] and alignment [19, 24].

The CNTs growth in CCVD is governed by the choice of carbon source, catalyst and growth temperature although in many studies other parameters, such as growth time [22, 25], have been also proved to be crucial to the resulting carbon materials. Concerning CCVD, the catalytical decomposition of hydrocarbon gases (mainly benzene [26, 27], acetylene [8, 28-30], ethylene [31, 32], methane [13, 20] or CO [33, 34]) is realized making use of metal particles (most commonly Fe, Ni, Mo and Co or their alloys) embedded in supports such as alumina [31, 35], zeolites [36, 37], $CaCO_3$ [38, 39], mesoporous silica [40, 41], silica [24, 42, 43], graphite [44], magnesium oxide [13, 30] and clays [8, 9].

Acetylene in comparison with other hydrocarbon gases, is considered a good carbon source for few-walls CNTs production because of both its lower number of carbon atoms per molecule and its greater reactivity [16, 45].

The use of MgO as support material, as extensively reported in the literature [30, 46-49], as minimizes the formation of amorphous carbon, prevents the metal particles from aggregating, while it can be dissolved from the synthesized carbon products by simple and mild purification procedures (dilute hydrochloric solutions) without destroying neither structural tube integrity nor their intrinsic properties. On the other hand, the use of Fe-Co bimetallic catalysts supported on various substrates, is reported to be more effective if compared to pure Fe or Co catalysts, making them widely employed for the production of SWCNTs and DWCNTs [47, 50, 51] as well as MWCNTs [39, 52]. Moreover residual catalytic centers can be removed from the synthesized products by the use of dilute acid solutions, allowing a high degree one-step purification of CNTs from both substrate (MgO) and metal catalysts.

SWCNTs [46], DWCNTs [53] and mixtures of those two [54] have been grown over Fe-Co bimetallic catalysts using various combinations of support material and hydrocarbon gases [15, 55, 56]. SWCNTs and/or DWCNTs growth over Fe-Co catalysts supported on MgO using acetylene as carbon source still remains a challenge since only MWCNTs have been grown so far by pyrolytic decomposition of acetylene over Fe-Co catalysts supported on MgO [52, 57].

In this work, we report on the synthesis of SWCNTs in high yields by catalytic decomposition of acetylene over MgO supported Fe-Co bimetallic catalysts without performing any pre-reduction treatment. Catalysts with different metal loadings (2 % wt and 10 % wt) were prepared while different reaction temperature (700 $^{\circ}$C and 800 $^{\circ}$C) and reaction time (30 and 60 min) were chosen in the CCVD process. It was found that the optimal SWCNTs growth occurs using catalysts loaded with 1% wt Fe and 1% wt Co at 800 $^{\circ}$C for 30 min. The electronic and chemical structure of the synthesized carbon products were analyzed by Energy Filter Transmission Electron Microscope (EFTEM), valence band photoelectron spectroscopy at the SpectroMicroscopy beamline (ELETTRA synchrotron radiation source) and Scanning Tunneling Spectroscopy (STS), while

TEM, STM, SEM, XRD (X-ray diffraction), DTA/TG and Raman permitted to depict the samples morphology, yield of the reactions and the chemical structure at nanometric scales.

3.1.2 Apparata, sample preparation and treatments

3.1.2.1 Catalysts Preparation

Bimetallic catalysts, with different wt % proportions of Fe:Co:MgO (1:1:98, 5:5:90) were prepared using a wet chemical impregnation method. In a typical synthetic procedure, 500 mg MgO were dispersed in 10 ml of distilled water and the suspension was sonicated, followed by stirring for 60 min in order to produce a homogeneous suspension. Appropriate amounts of aqueous solutions of metals nitrates [Fe(NO3)3·9H2O and Co(NO3)2·6H2O] were then added to the MgO suspension and the mixture was further stirred for 30 min. The final mixture was dried at 120 °C under vacuum, collected and grounded in fine powder.

3.1.2.2 Carbon Nanotubes Growth

For the CNTs synthesis, 100 mg of the catalyst powder were placed in an alumina crucible within a quartz tube, located in a horizontal tubular furnace. The sample was heated up to the desired temperature under nitrogen atmosphere. When the required temperature was achieved, acetylene as a carbon precursor was admixed with the carrier gas (nitrogen) at flow rates of 10 cm^3/min and 90 cm^3/min, respectively. The CNTs growth process took place over catalysts with different metal loadings, at 700 and 800 ^{o}C and for different reaction times (30 and 60 min). After the completion of acetylene flow, the ceramic boat was cooled down to room temperature under nitrogen atmosphere and, finally, the deposited materials were collected from the ceramic boat. The descriptions of each catalyst, the growth conditions as well as the code names for the synthesized CNTs are given in Table 1.

Description of the CNTs sample	Sample Code
CNTs grown over MgO loaded with 5 wt % Fe and 5 wt % Co at 700 ^{o}C for 30 min	CNT-Fe5%-Co5%-700-30
CNTs grown over MgO loaded with 5 wt % Fe and 5 wt % Co at 800 ^{o}C for 30 min	CNT-Fe5%-Co5%-800-30
CNTs grown over MgO loaded with 1 wt % Fe and 1 wt % Co at 800 ^{o}C for 30 min	CNT-Fe1%-Co1%-800-30
CNTs grown over MgO loaded with 1 wt % Fe and 1 wt % Co at 800 ^{o}C for 60 min	CNT-Fe1%-Co1%-800-60

Table 1. Code names for the CNTs samples grown over different catalysts and at different growth conditions.

3.1.2.3 Characterization Techniques

X-ray powder diffraction data were collected on a D8 Advance Bruker diffractometer using Cu Kα (40 kV, 40 mA) radiation and a secondary beam graphite monochromator. The patterns were recorded in the 2-theta (2θ) range from 2° to 90°, in steps of 1° and counting time 2s per step. Raman spectra were recorded in the range of 100-3500 cm^{-1}with a Micro-Raman system RM 1000 RENISHAW using a laser excitation line at 532 nm (Nd-YAG). A beam power of 0.5 to 1 mW was used with 1 μm focus spot in order to avoid photodecomposition of the samples.

Thermogravimetric (TGA) and differential thermal (DTA) analysis were performed using a Perkin Elmer Pyris Diamond TG/DTA. Samples of approximately 5 mg in weight were heated in air from 25 to 850° C, at a rate of 5° C/min.

The Ultraviolet Photoemission Spectroscopy (UPS) data were collected at the Spectromicroscopy beamline of the Elettra Synchrotron in Trieste. The photon beam energy, 95.0 eV, is intentionally chosen to minimize the mean free path of the photoelectrons and, thus, to allow the collection of a signal related to the topmost surface layers with a penetration depth of less than 1nm.

Scanning electron images were recorded using a scanning electron microscope (SEM) Quanta FEG 400 (FEI). The SEM images were acquired with an electron beam of 20 keV and X-ray fluorescence spectra were acquired in the

energetic range 0-10 keV with an Energy Dispersive X-ray Detector (EDX) in order to obtain the bulk elemental composition of the samples. The images show the typical morphology of the samples under observation.

Transmission electron nanograph were obtained with High Resolution Transmission Electron Microscope (HRTEM) LEO 922 200 KV. The microscope can be utilized to obtain electronic and chemical properties by Energy Filter TEM (EFTEM).

Finally, Scanning Electron Microscopy/Spectroscopy (STM/STS) measurements were performed at RT in air with a Schaefer STM using home-made Pt/Ir tips. For the STS measurement we interrupt the feedback control of piezo and we ramp the voltage from −1 to +1 V. The CNTs powder was dispersed in acetone and a small drop of the suspension was left to dry in air on graphite.

3.1.3 Structural, morphological, electronic, thermal and vibrational characterization and discussion

3.1.3.1 Characterization of Carbon Nanotubes

The XRD patterns of the as-prepared catalysts and the final carbon products were compared in order to determinate their crystalline phases. The diffraction patterns (fig. 1) reveal that the samples undergo to an ordering process upon the thermal pre-treatment at 800 ° C. After CVD treatment we detect the characteristic graphite (002) peak at $2\theta \approx 26^o$ together with the MgO lines while they are missing when the catalysts were heated in air without acetylene flow. Although the XRD patterns are not suitable to differentiate microstructual details between CNTs and other similar graphite-like structures, since the CNTs diffraction peaks are close to those of graphite [58], they provide a primary evidence of graphitic-like deposits. The intensity of the graphite (002) peak can be connected with the degree of graphitization of the synthesized products. Generally less ideal graphitized materials, exhibit decreased (002) peaks [39]. However this peak is indicative of the multi walls in the CNTs and its presence in the SWCNTs

samples is due to multilayered graphite catalytic nanoparticles [81]. The peak at 44.8° corresponds to the 100 diffraction of CNTs.
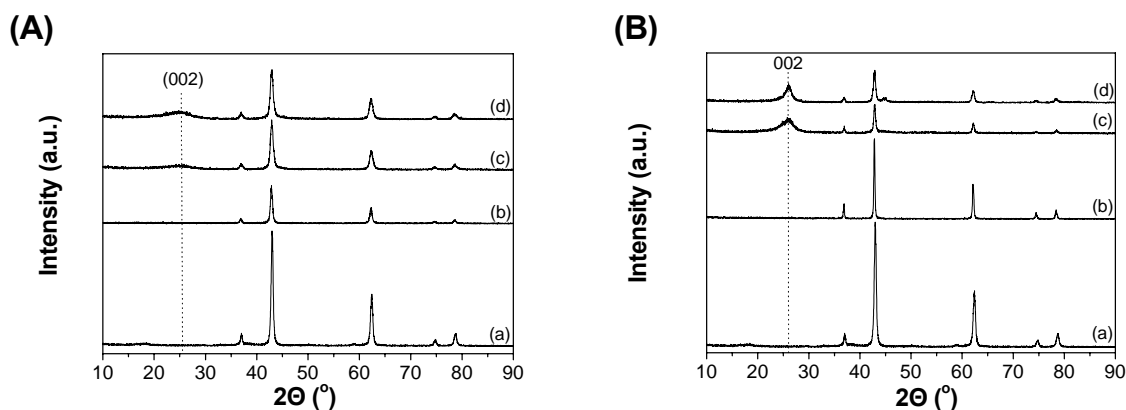
Figure 1. (A) XRD patterns of pure MgO (a), MgO loaded with 5 wt % Fe and 5 wt % Co heated at 800 °C for 30 min under air (b), CNT-Fe5%-Co5%-700-30 sample (c) and CNT-Fe5%-Co5%-800-30 sample (d). (B) XRD patterns of pure MgO (a), MgO loaded with 1 wt % Fe and 1 wt % Co heated at 800 °C for 30 min under air (b), CNT-Fe1%-Co1%-800-30 sample (c) and CNT-Fe1%-Co1%-800-60 sample (d).

Raman spectra of the synthesized samples show the main characteristic CNTs Raman signals, at ~1300 and ~1580 cm^{-1} corresponding to graphite D- and G-bands respectively (fig. 2). In general, the G-band corresponds to the tangential stretching (E_{2g}) mode of highly oriented pyrolytic graphite (HOPG), while the D-band originates from disorder in the sp^2-hybridized carbon atoms and are characteristic for lattice distortions in the curved graphene sheets and/or tube ends [59-61].

The presence of SWCNTs in both CNT-Fe1%-Co1%-800-30 and CNT-Fe1%-Co1%-800-60 samples is confirmed by the appearance of a shoulder peak at 1535 cm^{-1}, on the left side of the main G-band peak (1582 cm^{-1}). This feature originates from the splitting of the E_{2g} tangential mode (ω_G^- component in particular) and it is considered a characteristic Raman feature of SWNTs [62] and/or DWCNTs [63]. The findings from UPS data (see below) are in fully agreement with those derived from Raman data, indicating the existence of CNTs with few graphite

walls. The I_D/I_G ratio value of sample CNT-Fe1%-Co1%-800-30 (Table 2) is quite low (0.242), indicating that the synthesized SWCNTs material is of both good quality and purity [64]. Note that these ratio values are among the lowest reported in the literature, where normally they are I_D/I_G = 0.85-1.3, for CNTs prepared using acetylene as carbon source [65, 66].

3.3..0 Sample code	I_D/I_G Ratio
CNT-Fe5%-Co5%-700-30	0.950
CNT-Fe5%-Co5%-800-30	0.880
CNT-Fe1%-Co1%-800-30	0.242
CNT-Fe1%-Co1%-800-60	0.527

Table 2: I_D/I_G ratio of synthesized samples.

Additionally, in the spectra of CNT-Fe1%-Co1%-800-30 and CNT-Fe1%-Co1%-800-60 samples (fig. 2B), we observe the presence of the Radial Breathing Mode (RBM) bands at about 270 cm^{-1} corresponding to the A_{1g} "breathing" mode of the tubes [67] and attributed to CNTs with small diameters (less than 3nm) [68]. The RBM corresponds to the coherent vibration of the C atoms in the radial direction and it is characteristic of SWCNTs [13, 64, 69], DWCNTs [14, 55, 63] or a combination of those two [46] synthesized by CCVD and other methods. The RBM position is strongly depended on the CNTs diameter and, therefore, it can be used to calculate the tube diameter in the case of SWCNTs. The RBM frequency ω_{RBM} (cm^{-1}) depends on the tube diameter d_t (nm) according to the formula ω_{RBM} = a/d_t + b where a,b are parameters are determined experimentally [70]. If we compare the Raman spectra of CNT-Fe1%-Co1%-800 samples (fig. 2B), passing from 30 min to 60 min of growth time, we record a considerable reduction of G-band's intensity with a doubling of the I_D/I_G ratio (see table 2) indicating that prolonged depositions result in the deposit of carbonaceous material of lower

crystallinity. Longer reaction times enhance the deposition of amorphous carbon without any significant increase in CNTs material.

On the contrary, Raman spectra of CNT-Fe5%-Co5%-700-30 and CNT-Fe5%-Co5%-800-30 samples (fig. 2A) did not show any RBM peaks or shoulder at ~1535 cm^{-1}, suggesting that no SWCNTs growth occurred for 10% metal loading. In addition, the strong D-band at 1338 cm^{-1} indicates a defective structure or a lower degree of graphitization of the synthesized CNTs structure. The presence in high amounts of amorphous carbon in both CNT-Fe5%-Co5%-700-30 and CNT-Fe5%-Co5%-800-30 samples can also be supposed by looking to the upshift of the D-band. It is worth to point out that the increment of the amount of Fe-Co catalysts supported on MgO, did not result in an increment of the SWCNTs. On the contrary, higher metal loadings favor the formation of less graphitized CNTs structures with more carbon walls and/or more amorphous carbon, as indicated from the UPS data (see below).
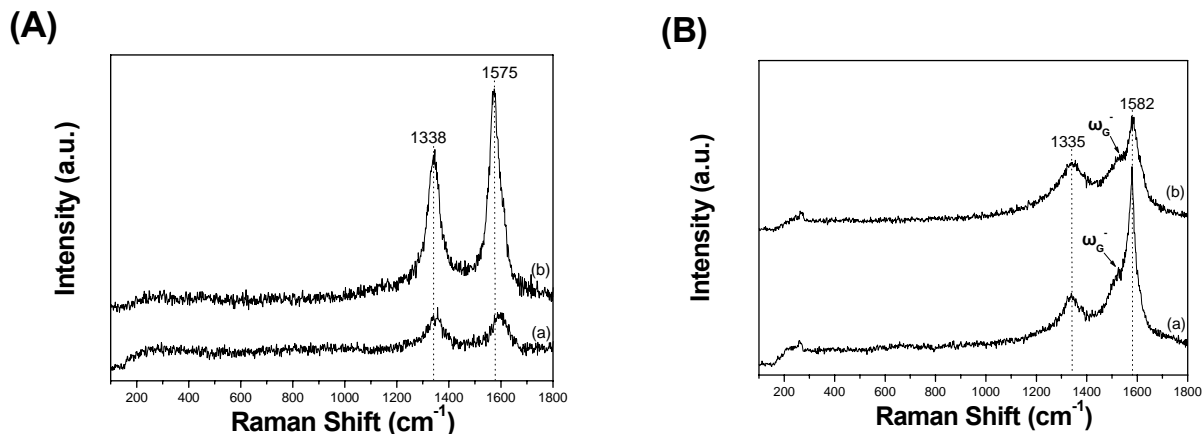
Figure 2. (A) Raman spectra of CNT-Fe5%-Co5%-700-30 (a) and CNT-Fe5%-Co5%-800-30 (b) samples. (B) Raman spectra of CNT-Fe1%-Co1%-800-30 (a) and CNT-Fe1%-Co1%-800-60 (b) samples.

TG curves derived from thermogravimetric analysis (TGA) measurements, can be used to determinate the percentage of deposited carbon (and subsequently the percentage of CNTs) in the synthesized materials [71]. In general, two major

weight losses are recorded when the heating of samples containing CNTs synthesized from CCVD takes place in air. They are attributed to the removal by oxidation of amorphous carbon (300-400° C) and CNTs (typically > 400° C), respectively [72, 73]. The % amorphous carbon yield and the % CNTs yield can be estimated according to the formula $aC\_\%Yield = \dfrac{\Delta W^{300-400°C}}{W^{700°C}} \times 100\%$ and

$$CNT\_\%Yield = \dfrac{\Delta W^{400-700°C}}{W^{700°C}} \times 100\% \text{ [36] respectively.}$$

The oxidation temperature of the deposited carbon material can be measured from the DTA curve and corresponds to the maximum of the exothermic peak. Higher oxidation temperatures are associated with purer, less defective, highly crystalline SWCNTs [67] or MWCNTs [74]. In fact, narrow diameter results in higher degree of curvature and, subsequently, higher reactivity toward oxygen at elevated temperatures [75]. Moreover, the presence of numerous defects along the walls and/or ends is supposed to lower the relative thermal stability of CNTs as these defects provide edges and dangling bonds for oxidative combustion. DTA and TGA curves of the synthesized samples, while in Table 3 are summarized the carbon yield and the oxidation temperature for the synthesized samples.

Sample	CNT-Yield (%)	aC-Yield (%)	DTA $_{Max}$ (^{o}C)
CNT-Fe5%-Co5%-700-30	283	4.7	591
CNT-Fe5%-Co5%-800-30	235	3.1	623
CNT-Fe1%-Co1%-800-30	104	1.5	515
CNT-Fe1%-Co1%-800-60	121	0.8	542

Table 3: Carbon yield and oxidation temperature of the synthesized products

When graphitized carbon products such as MWCNTs coexist with SWCNTs, it becomes rather difficult to specify the amount of SWCNTs only by TGA. This is because, some kind of well-graphitized product also burns at higher temperature range that overlaps the range of SWCNTs. As a possible method for estimating

the amount of each constituent, we could decompose their DTG curves into several Gaussian–Lorentzian components and *attempt* to estimate the amount of each carbon species including amorphous carbons and MWCNTs. However, this method is not accurate for the estimation of the yield.
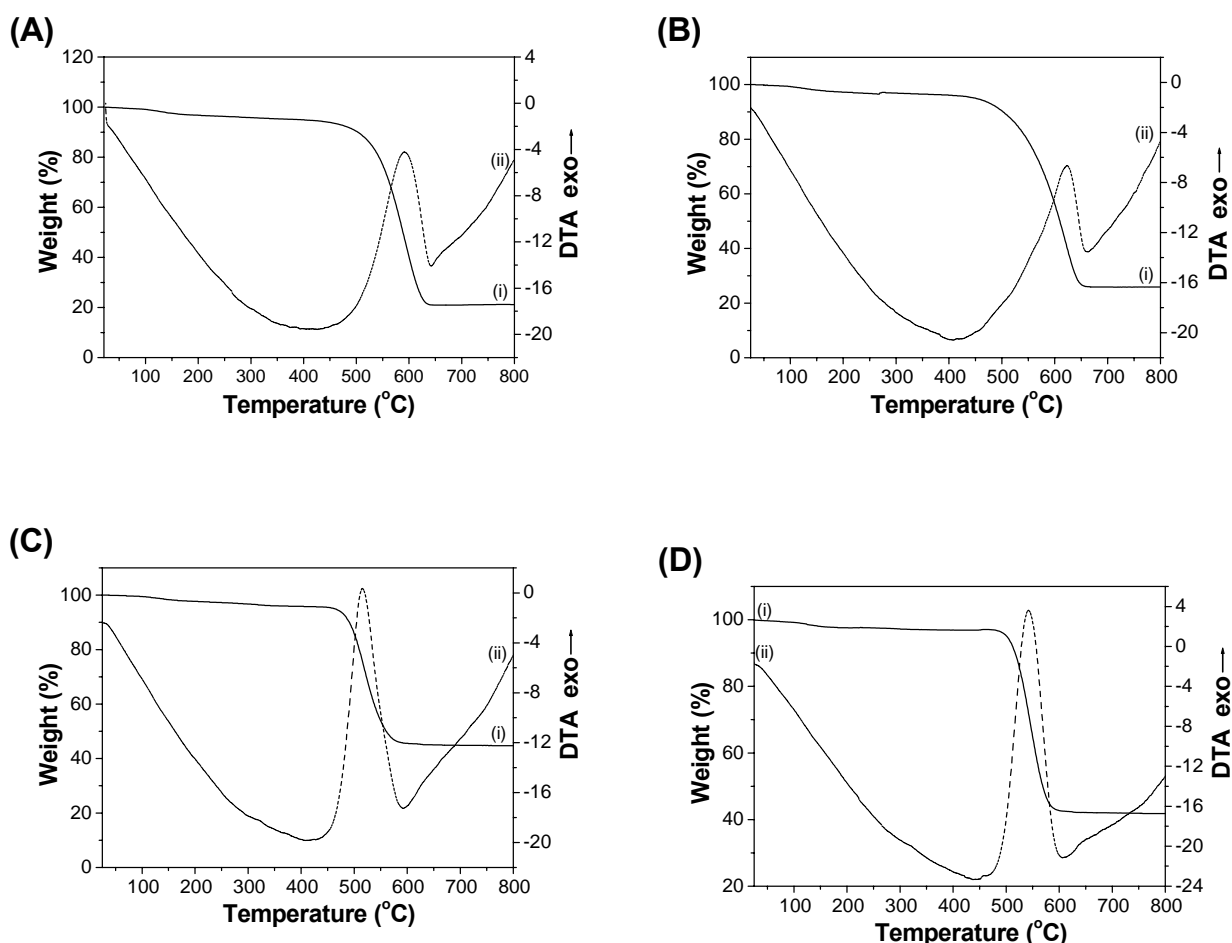

Figure 3. TGA (i) and DTA (ii) curves of CNT-Fe5%-Co5%-700-30 (A), CNT-Fe5%-Co5%-800-30 (B), CNT-Fe1%-Co1%-800-30 (C) and CNT-Fe1%-Co1%-800-60 (d) sample.

The CNTs grown over catalysts with 10 % wt metal loaded MgO exhibit much higher oxidation temperatures compared those grown over 2 % wt metal loaded MgO. This is probably due to their larger diameters and higher crystallinity induced by the high metal content. On the other hand, the thermal stability of the CNTs grown at 800° C over 10 % wt catalyst compared to those grown at 700° C

show a similar influence of the synthesis temperature on the CNTs morphological features. Using the same framework, we can affirm that a longer growth time on the 2 % wt metal loaded MgO should reduce the defects on small diameter CNTs. In order to shine some light on the C bonding characteristics of the investigated samples and to compare them with the reference spectra of graphite, nanostructured C (with a mainly sp^2 hybridization), pure SWCNTs and MWCNTs, we performed a valence band study by photoemission spectroscopy using identical experimental conditions (see figure 4, right panel) [76, 77]. In the graphite spectrum, we distinguish the following spectral regions: the $2p\pi$ states covering the 0-3.5 eV in binding energy with a shoulder at 3.0 eV; the $2p\sigma$ states show three peaks at 8.0 eV, 5.5 eV and 10.5 eV; at higher binding energy we find the region of the weakly interacting 2sp mixed states at 13.5 eV and the 2s states at 17.0 eV [77].
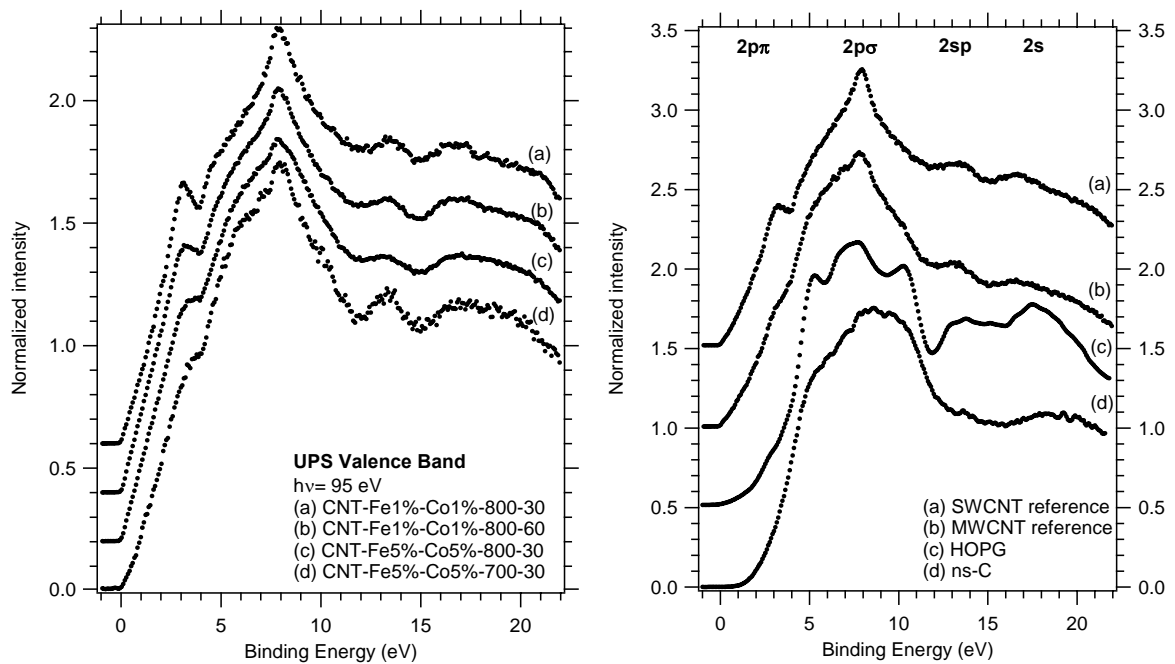
Figure 4. Left panel – Valence Band photoemission spectra induced by a 95.0 eV photon beam on CNT samples. Right panel – The same energetic region for Graphite (full line), MWCNT (dotted line) and SWCNT (dashed line) [88].

In comparison with graphite, the $2p\pi$ emission becomes progressively more intense in the MWCNTs and in the SWCNTs spectra. We can ascribe this behavior to the increasing mixed sp^2/sp^3 character of the bonding in the curved

CNTs walls. As a counterpart of this evolution, the 2pσ spectral distribution that in graphite has pronounced features at 5.5, 8.0 and 10.5 eV develops into a narrower structure in which the central component at 8 eV in binding energy results less intense. In spite to the finely structured spectra of the ordered forms of C, the nanostructured C [ns-C is described as a mainly sp^2-C network containing highly curved surfaces in which the long range order is very low, see ref. 88] shows a smooth spectrum were the broad 2pσ peak can be clearly distinguished. The reported difference in the 2pπ and 2pσ emission is due to the hybridization of the valence states and to the long range order. In this way the low 2pπ emission and the triple 2pσ structure are identified as reference spectral features for graphite and the narrow peaks at 3.0 and 8.0 eV for SWCNTs. Thus, as an example, when the CNTs present less carbon walls or less amorphous carbon they have a 2pπ emission with higher intensity. Therefore, MWCNTs spectrum has an intermediate shape between these extreme cases decreasing the external wall curvature as the number of walls increases.

With this in mind, the differences between the valence band spectra of the different samples shown in the left panel of figure 4 are taken into account. Analyzing the sequence of the samples CNT-Fe5%-Co5%-700-30, CNT-Fe5%-Co5%-800-30, CNT-Fe1%-Co1%-800-60 and CNT-Fe1%-Co1%-800-30, the 2pπ feature and the 8.0 eV peak become gradually more evident. Thus, the signal relative to the content of SWCNTs in the analyzed samples increases from the former to the latter. This is also compatible with: 1) a decrease of the number of multiwall nanotubes in the probed samples, 2) the decrease of the graphitic particles amount or 3) the decrease of sp^2 amorphous carbon. A further evidence of graphite (or sp^2 amorphous carbon) presence in the samples is shown in the zero binding energy edge of the valence band spectra of figure 4: the CNT-Fe5%-Co5%-700-30 spectrum intensity reaches the Fermi edge with the lowest gradient similar to graphite, while the CNT-Fe1%-Co1%-800-30 has the highest one.

Furthermore, the sharpness of the spectral features is bigger in CNT-Fe5%-Co5%-700-30 and CNT-Fe1%-Co1%-800-30 samples compared to the remaining samples. This is an evidence of the absence in these spectra of the amorphous carbon featureless contribution. In fact, the peaks position and width are not

changed however a decrease of the spectral weight in the central part of the valence band emission is observed.

Concerning other possible contributions to the spectra, we find no evidence of Oxygen 2p and 2s signal in our spectra even though its higher cross section would put in evidence any trace of it. As a matter of fact, a clear peak at 27 eV due to the O 2s emission is present in the spectra of purified SWCNTs after the adsorption water or NO_2 at low temperatures.

Furthermore, there is not any feature due to the catalyst particles (Co/Fe) or of the substrate (MgO). An indirect prove of the absence of these contaminants on the surface of our samples is given by the fact that these particles, after a long exposure to air, should result in a very oxidized state providing a further source for the Oxygen signal.

High magnification SEM and TEM images give an excellent overview of the range of carbon nanostructures created in the final products and support these findings as they reveal a granular structure (in microscopic scale) which consists mainly of interlaced nanotubes bundles while the amounts of amorphous carbon varies and the content of remaining catalytic metal particles is always very low.


(a)   (b)
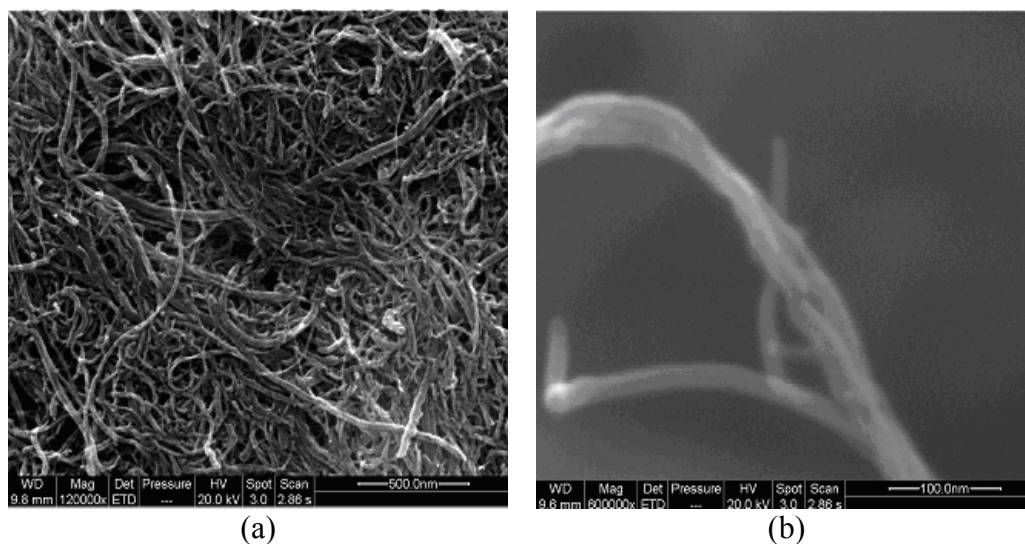
Figure 5. SEM images of sample CNT-Fe1%-Co1%-800-30 showing carbon nanotubes bundles as the main constituents of the sample (a), and a high magnification image showing carbon nanotubes bundles (b).

Figure 5 shows the SEM images of CNT-Fe1%-Co1%-800-30 sample at different magnifications, where we can observe a granular structure with micrometric

length which consists mainly of interlaced nanotubes bundles. In this sample we can not detect any observable trace of amorphous carbon or catalytic metallic particles.

By looking to the SEM images of the CNT-Fe1%-Co1%-800-60 sample we check the effects of a longer growth time on low metal content catalyst. The recorded images (fig. 6) are similar to those of the CNT-Fe1%-Co1%-800-30 sample showing a granular structure. At higher magnification we can observe that the nanotubes bundles are the main building blocks of the material (fig. 6a). Some tiny trace of amorphous carbon material was also seen (fig. 6b).

(a)

(b)

(c)
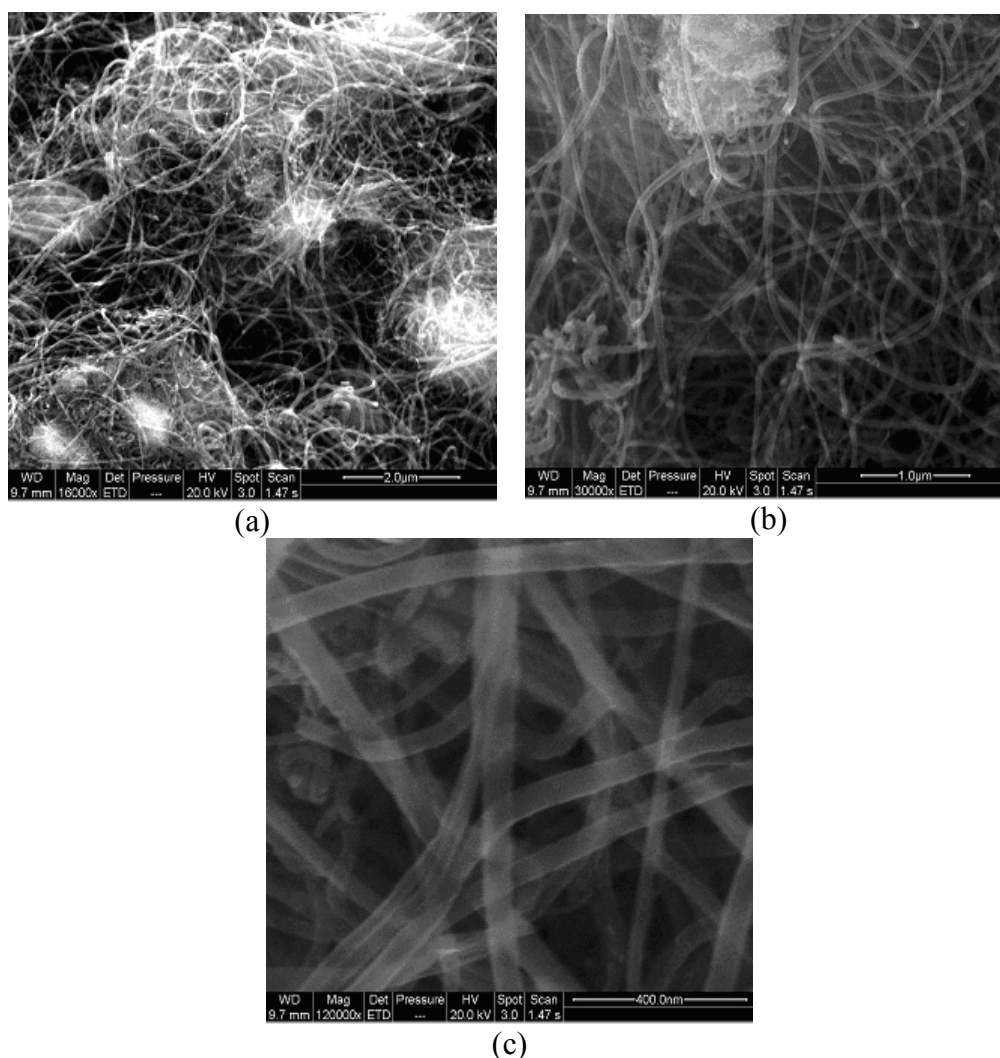
Figure 6. SEM image of the sample CNT-Fe1%-Co1%-800-60 at low magnification (a), and at higher magnifications (b and c). Carbon nanotube bundles and amorphous carbon aggregates can be distinguished in (b).

The structure of the samples produced using 10% metal content catalyst is different from the low metal content one. The coexistence of nanotubes bundles with a large amount of amorphous nanometric aggregates is revealed in the SEM images of the sample CNT-Fe5%-Co5%-800-30 (fig. 7). The amorphous carbon species show a flat morphology with a typical lateral dimension below 100 nm (fig. 7a) while the CNTs bundles have a diameter ranging between 5 and 50 nm (fig. 7b).

(a)   (b)
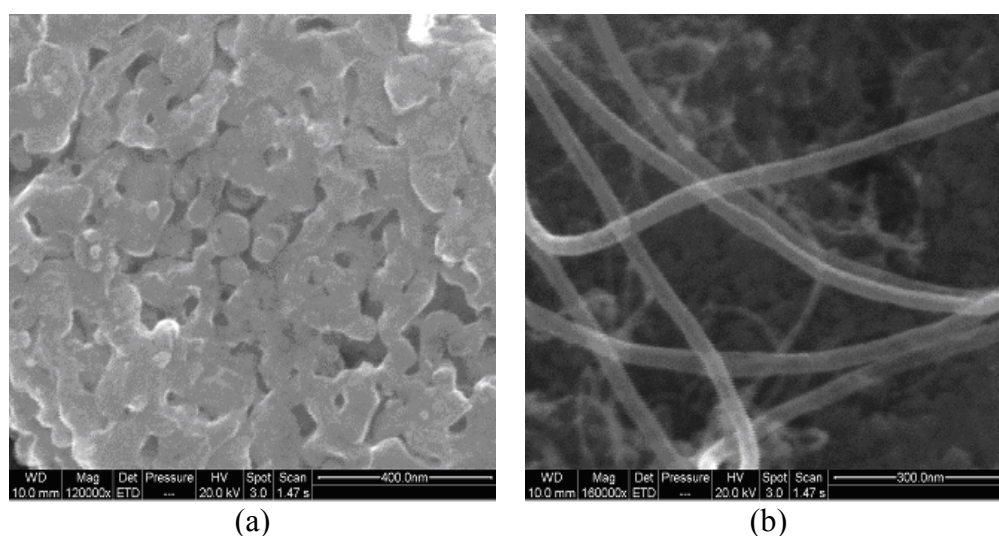
Figure 7. SEM images of the sample CNT-Fe5%-Co5%-800-30 which shows the presence of amorphous structures (a) and nanotubes bundles (b).

The granular appearance is present in the SEM images of the sample CNT-Fe5%-Co5%-700-30 at micrometric length scale (fig. 8a). At higher magnification, we observe the presence of carbon nanotube bundles (fig. 8b,c) and large amounts of other carbon aggregates (fig. 8d). The latter show a platelet structure in which each leaf is several hundreds nm wide and has a rough surface. In accord to the UPS and Raman results, we affirm that these carbon species are mainly amorphous. In fact, eventual graphitic particles should have smoother aspect while the typical Graphite line shape contribution might be present in the UPS spectra (see above)
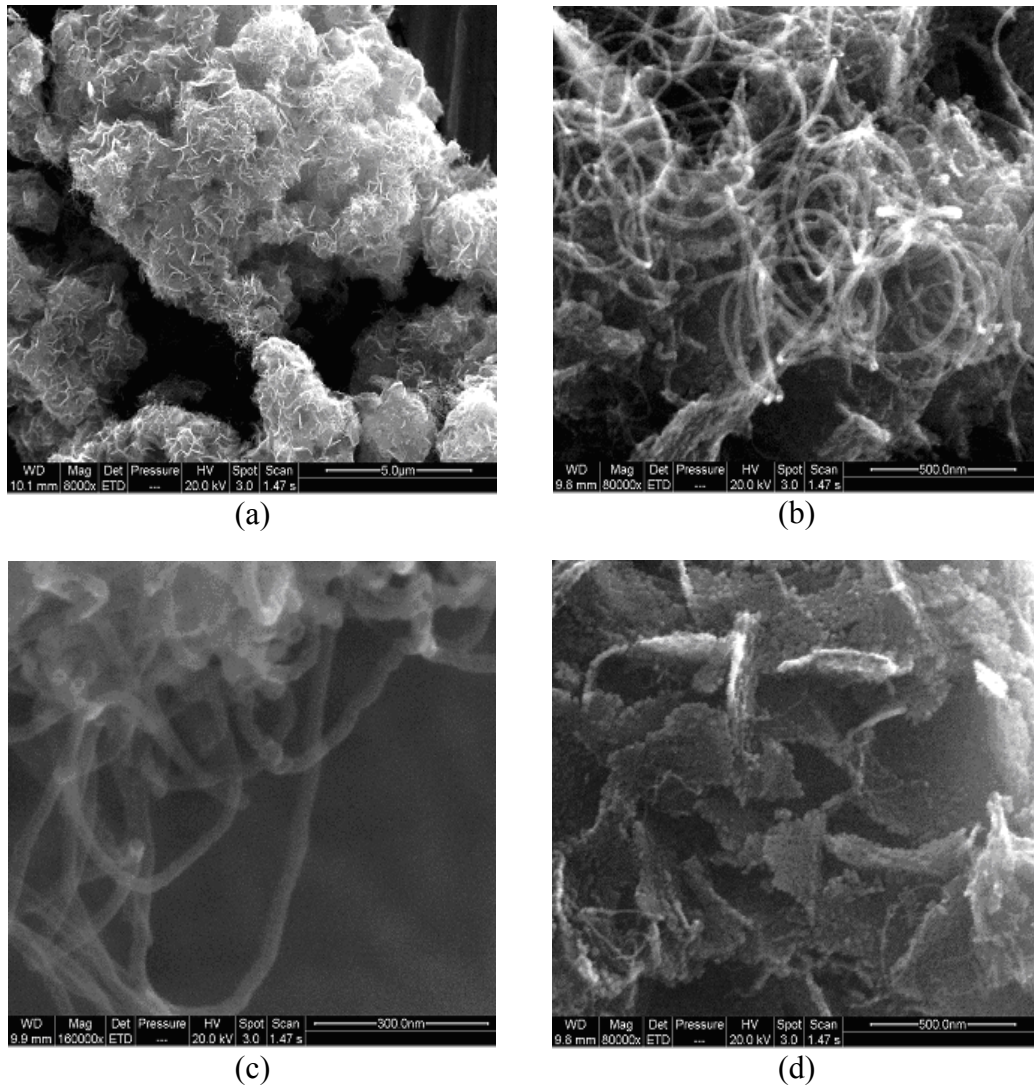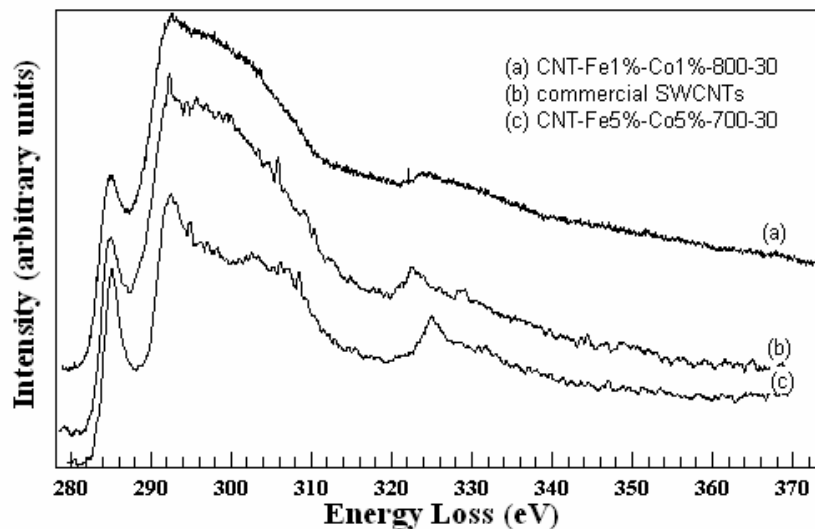
Figure 8. SEM image of the sample CNT-Fe5%-Co5%-700-30 at low magnification (a), at high magnification (b), (c) and at high magnification with predominance of amorphous carbon aggregates (d).

The elemental analysis performed acquiring the fluorescence spectra allowed us to detect the pureness of the analyzed samples and to determine the residual small amounts of catalyst. The CNTs samples grown on Fe1%-Co1%/MgO present less amount of catalytic nanoparticles (less than 5%at) while amount up to 25%at are present in the sample grown on Fe5%-Co5%/MgO catalyst. The catalytic nanoparticles maintain their stoichiometry and are finely dispersed in the sample. In fact, it was not possible to identify any of those particles by combined SEM/fluorescence analysis.

The TEM images give an idea of the tube size (MWCNTs or SWCNTs) and contemporary the local electronic and chemical properties. The samples investigated by TEM were CNT-Fe1%-Co1%-800-30 and CNT-Fe5%-Co5%-700-30. The sample CNT-Fe1%-Co1%-800-30 presents a bundled structure of CNTs and it was not possible to separate one of them.

Both of them present bundled structure with tube size less than 2 nm. The C1s K-edges on the sample CNT-Fe1%-Co1%-800-30 and CNT-Fe5%-Co5%-700-30 and on the commercial SWCNTs were acquired (see figure 9). The line shape of the C1s K-edge spectra can give an idea of the CNTs curvature.

Figure 9. C1s K-edge of commercial SWCNTs, sample CNT-Fe1%-Co1%-800-30 and CNT-Fe5%-Co5%-700-30.

The line shape of commercial and CNT-Fe1%-Co1%-800-30 samples is typical of SWCNTs [78]. On the other hand the sample CNT-Fe5%-Co5%-700-30 shows a C1s K-edge more graphitic with a typical line shape of MWCNTs as shown in the literature [79]. The C1s K-edge it is a reminder of valence band properties of the sample. In fact it presents two main excitations at ~285 eV (C 1s → π^* excitation) and at ~292 eV (C 1s → σ^* excitation). However in the MWCNTs sample (CNT-Fe5%-Co5%-700-30) the two excitations are more pronounced and the decrease of the spectrum after the C 1s → σ^* excitation is more smooth. The behavior is due to curvature effects.

STM images were obtained on the CNT-Fe1%-Co1%-800-30 sample in order to depict the single CNT (see figure 10).
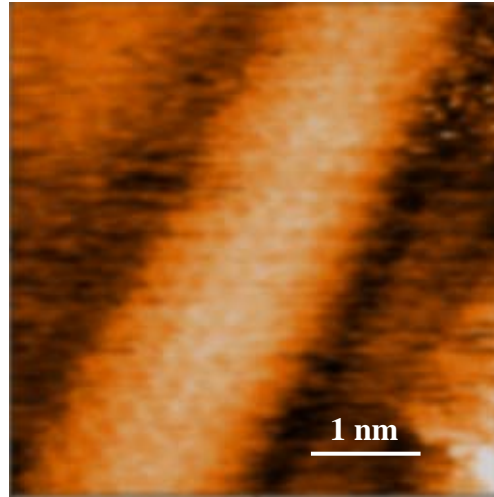
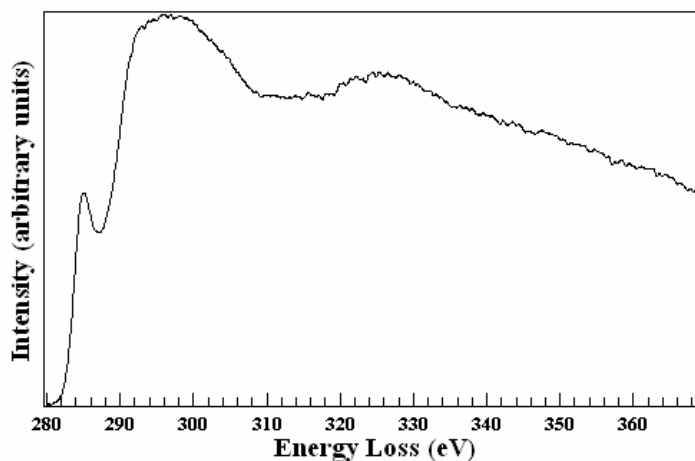**Figure 10**. STM image of sample CNT-Fe1%-Co1%-800-30.

The size of the tube is around 1.4 nm which is indicative of SWCNTs. On the other hand this result is in agreement with the Raman measurements. The STS acquired on it was compared with STS measurements obtained with the same tip on graphite. In figure 11 the normalized conductance of sample CNT-Fe1%-Co1%-800-30 and graphite are reported showing a bigger gap for the SWCNTs than graphite. The continuous line is the threshold to measure the gap. In fact the normalized conductance in metals is equal 1 and it is taken into account like reference to measure the band gap.
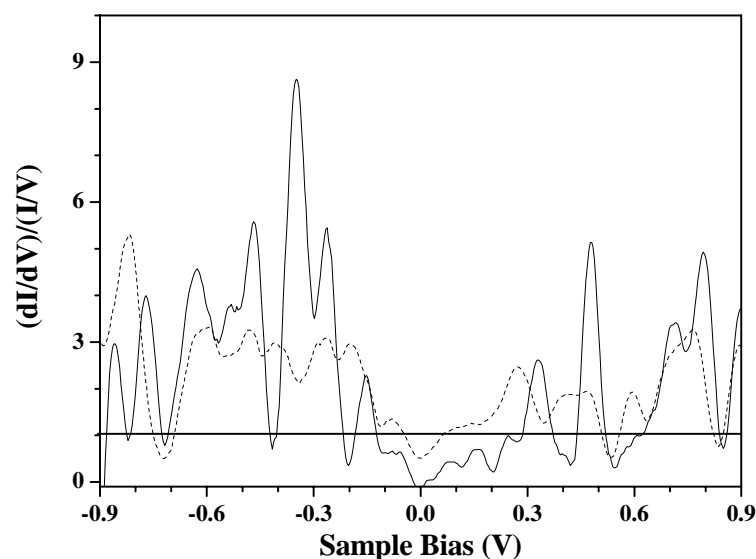
Figure 11. normalized conductance of sample CNT-Fe1%-Co1%-800-30 (continuous line) and graphite (dashed line). The constant line ((dI/dV)/(I/V)=1) is the threshold to calculate the band gap (see text).

Finally the TEM picture and C1s, Co2p and Fe2p K-edge spectra were obtained also on catalytic nanoparticles in sample CNT-Fe1%-Co1%-800-30. The nanoparticles were not observed in UPS and SEM measurements because of the small quantities of the catalyst compared to the carbon materials and in addition the nanoparticles were not localized in the surface of the analyzed powder in the SEM measurements (in the TEM experiments the powder was well dispersed on the carbon grid). The C1s K-edge measurements acquired on these particles show a carbon line shape with intermediate character between graphitic and amorphous (see figure 12) [80]. Probably, the carbon decomposes over it by covering the nanoparticles with amorphous-graphitic walls. This results can also explain the presence of the (002) peak in the XRD spectrum of sample CNT-Fe1%-Co1%-800-30. The Co 2p and Fe 2p K-edge spectra (not shown) were also obtained showing the contemporary presence of the two catalysts in the nanoparticle. Since the nanoparticles should create a unique bimetallic alloy which should explain the high performance of CNTs production in presence of both of them.

Figure 12. C1s K-edge spectrum obtained on the catalytic nanoparticle.

3.1.4 Concluding remarks

The sample CNT-Fe1%-Co1%-800-30 presents is SWCNTs while the sample CNT-Fe5%-Co5%-700-30 has more carbon walls or more amorphous carbon. The latter is in agreement with the Raman results since the spectra of CNT-Fe1%-Co1%-800-30 and CNT-Fe1%-Co1%-800-60 samples show the radial breathing mode which is characteristic of SWCNTs. The lower intensity of the 2pπ excitation in the samples CNT-Fe5%-Co5%-700-30 and CNT-Fe5%-Co5%-800-30 also agrees with their I_D/I_G ratios calculated by Raman spectra which are higher compared to the ratios of the samples CNT-Fe1%-Co1%-800-30 and CNT-Fe1%-Co1%-800-60 due to the presence of higher quantity of amorphous carbon. Carbon is in any case the major constituent (over 70%) of the samples and we suggest (considering also the valence band analysis) that the amorphous phase may be due to sp2 hybridized carbon nano-aggregates (the Mg content being too low, 11 %, to be the major constituent of the nanometric aggregates). In fact the SEM results corroborate and extend the interpretation of the valence band behaviors. In this picture, the CNT-Fe5%-Co5%-800-30 and CNT-Fe5%-Co5%-700-30 valence bands (fig. 4) are due to the sum of the photoemission signal of the nanotubes bundles and that of the amorphous carbon nano-aggregates, this

explain the lower intensity of the C 2pπ signal and the lower gradient of the photoemission intensity approaching the Fermi edge comparing to the CNT-Fe1%-Co1%-800-30 and CNT-Fe1%-Co1%-800-60 samples (made mainly by nanotubes bundles).

Indeed, SEM images show traces of amorphous carbon intercalated into the CNTs network. Similar findings are derived from UPS data, suggesting that SWCNTs was accomplished during the first 30 minutes show better quality.

3.1.5 References

[1]   S. Iijima, Physica B **323**, 1 (2002).

[2]   T. Guo, P. Nikolaev, A. Thess, D. T. Colbert, and R. E. Smalley, Chemical Physics Letters **243**, 49 (1995).

[3]   A. Thess, R. Lee, P. Nikolaev, H. J. Dai, P. Petit, J. Robert, C. H. Xu, Y. H. Lee, S. G. Kim, A. G. Rinzler, D. T. Colbert, G. E. Scuseria, D. Tomanek, J. E. Fischer, and R. E. Smalley, Science **273**, 483 (1996).

[4]   J. L. Hutchison, N. A. Kiselev, E. P. Krinichnaya, A. V. Krestinin, R. O. Loutfy, A. P. Morawsky, V. E. Muradyan, E. D. Obraztsova, J. Sloan, S. V. Terekhov, and D. N. Zakharov, Carbon **39**, 761 (2001).

[5]   S. Iijima, Nature **354**, 56 (1991).

[6]   T. W. Ebbesen and P. M. Ajayan, Nature **358**, 220 (1992).

[7]   F. Kokai, K. Takahashi, M. Yudasaka, R. Yamada, T. Ichihashi, and S. Iijima, Journal of Physical Chemistry B **103**, 4346 (1999).

[8]   D. Gournis, M. A. Karakassides, T. Bakas, N. Boukos, and D. Petridis, Carbon **40**, 2641 (2002).

[9]   L. Jankovic, D. Gournis, K. Dimos, M. A. Karakassides, and T. Bakas, Journal of Physics: Conference Series **10**, 178 (2005).

[10]   B. Chen, G. Parker, J. Han, M. Meyyappan, and A. M. Cassell, Chemistry of Materials **14**, 1891 (2002).

[11]   B. Q. Wei, R. Vajtai, Y. Jung, J. Ward, R. Zhang, G. Ramanath, and P. M. Ajayan, Nature **416**, 495 (2002).

[12]   L. Qingwen, Y. Hao, C. Yan, Z. Jin, and L. Zhongfan, Journal of Materials Chemistry **12**, 1179 (2002).

[13]   H. Ago, S. Imamura, T. Okazaki, T. Saito, M. Yumura, and M. Tsuji, Journal of Physical Chemistry B **109**, 10035 (2005).

[14]   H. Ago, K. Nakamura, S. Imamura, and M. Tsuji, Chemical Physics
        Letters **391**, 308 (2004).

[15]   P. Ramesh, T. Okazaki, R. Taniguchi, J. Kimura, T. Sugai, K. Sato, Y.
        Ozeki, and H. Shinohara, Journal of Physical Chemistry B **109**, 1141
        (2005).

[16]   Y. Soneda, L. Duclaux, and F. Beguin, Carbon **40**, 965 (2002).

[17]   S. W. Yoon, S. Y. Kim, J. Park, C. J. Park, and C. J. Lee, Journal of
        Physical Chemistry B **109**, 20403 (2005).

[18]   J. H. Hafner, M. J. Bronikowski, B. R. Azamian, P. Nikolaev, A. G.
        Rinzler, D. T. Colbert, K. A. Smith, and R. E. Smalley, Chemical Physics
        Letters **296**, 195 (1998).

[19]   C. J. Lee and J. Park, Journal of Physical Chemistry B **105**, 2365 (2001).

[20]   Y. Li, X. Zhang, L. Shen, J. Luo, X. Tao, F. Liu, G. Xu, Y. Wang, H. J.
        Geise, and G. Van Tendeloo, Chemical Physics Letters **398**, 276 (2004).

[21]   C. L. Cheung, A. Kurtz, H. Park, and C. M. Lieber, Journal of Physical
        Chemistry B **106**, 2429 (2002).

[22]   N. Zhao, C. He, Z. Jiang, J. Li, and Y. Li, Materials Letters **60**, 159
        (2006).

[23]   Y. Li, W. Kim, Y. Zhang, M. Rolandi, D. Wang, and H. Dai, Journal of
        Physical Chemistry B **105**, 11424 (2001).

[24]   W. Z. Li, S. S. Xie, L. X. Qian, B. H. Chang, B. S. Zou, W. Y. Zhou, R. A.
        Zhao, and G. Wang, Science **274**, 1701 (1996).

[25]   C. O?ncel and Y. Yu?ru?m, Fullerenes Nanotubes and Carbon
        Nanostructures **14**, 17 (2006).

[26]   W. Chen, A. M. Zhang, X. Yan, and D. Han, Studies in Surface Science
        and Catalysis **142 B**, 1237 (2002).

[27]   Q. Li, H. Yan, J. Zhang, and Z. Liu, Carbon **42**, 829 (2004).

[28]   B. C. Liu, S. C. Lyu, S. I. Jung, H. K. Kang, C. W. Yang, J. W. Park, C. Y.
        Park, and C. J. Lee, Chemical Physics Letters **383**, 104 (2004).

[29]   J. Li, C. Papadopoulos, and J. Xu, Nature **402**, 253 (1999).

[30]   T. Tsoufis, P. Xidas, L. Jankovic, D. Gournis, A. Saranti, T. Bakas, and M.
        A. Karakassides, Accepted to Diamond & Related Materials.

[31]   W. Qian, T. Liu, Z. Wang, H. Yu, Z. Li, F. Wei, and G. Luo, Carbon **41**,
        2487 (2003).

[32]   M. Corrias, Y. Kihn, P. Kalck, and P. Serp, Carbon **43**, 2820 (2005).

[33]   W. E. Alvarez, B. Kitiyanan, A. Borgna, and D. E. Resasco, Carbon **39**, 547 (2001).

[34]   B. Zheng, C. Lu, G. Gu, A. Makarovski, G. Finkelstein, and J. Liu, Nano Letters **2**, 895 (2002).

[35]   H. Dai, A. G. Rinzler, P. Nikolaev, A. Thess, D. T. Colbert, and R. E. Smalley, Chemical Physics Letters **260**, 471 (1996).

[36]   S. Karakoulia, L. Jankovic, K. Dimos, D. Gournis, and K. Triadafyllidis, Studies in Surface Science and Catalysis **158**, 391 (2005).

[37]   P. Ramesh, N. Kishi, T. Sugai, and H. Shinohara, Journal of Physical Chemistry B **110**, 130 (2006).

[38]   E. Couteau, K. Hernadi, J. W. Seo, L. Thie?n-Nga, C. Miko, R. Gaa?l, and L. Forro, Chemical Physics Letters **378**, 9 (2003).

[39]   J. Cheng, X. Zhang, Z. Luo, F. Liu, Y. Ye, W. Yin, W. Liu, and Y. Han, Materials Chemistry and Physics **95**, 5 (2006).

[40]   D. Ciuparu, Y. Chen, S. Lim, G. L. Haller, and L. Pfefferle, J. Phys. Chem. B **108**, 503 (2004).

[41]   Y. Chen, D. Ciuparu, S. Lim, Y. Yang, G. L. Haller, and L. Pfefferle, Journal of Catalysis **225**, 453 (2004).

[42]   W. E. Alvarez, F. Pompeo, J. E. Herrera, L. Balzano, and D. E. Resasco, Chemistry of Materials **14**, 1853 (2002).

[43]   S. M. Bachilo, L. Balzano, J. E. Herrera, F. Pompeo, D. E. Resasco, and R. B. Weisman, Journal of the American Chemical Society **125**, 11186 (2003).

[44]   K. Hernadi, A. Fonseca, J. B. Nagy, D. Bernaerts, and A. A. Lucas, Carbon **34**, 1249 (1996).

[45]   C. N. R. Rao, B. C. Satishkumar, A. Govindaraj, and M. Nath, Chem Phys Chem **2**, 78 (2001).

[46]   J. F. Colomer, C. Stephan, S. Lefrant, G. Van Tendeloo, I. Willems, Z. Konya, A. Fonseca, C. Laurent, and J. B.Nagy, Chemical Physics Letters **317**, 83 (2000).

[47]   J. F. Colomer, G. Bister, I. Willems, Z. Ko?nya, A. Fonseca, G. Van Tendeloo, and J. B. Nagy, Chemical Communications, 1343 (1999).

[48]   E. Flahaut, R. Bacsa, A. Peigney, and C. Laurent, Chemical Communications **9**, 1442 (2003).

[49]   E. Flahaut, A. Peigney, C. Laurent, and A. Rousset, Journal of Materials Chemistry **10**, 249 (2000).

[50]   J. Zhu, M. Yudasaka, and S. Iijima, Chemical Physics Letters **380**, 496 (2003).

[51]   E. Flahaut, A. Govindaraj, A. Peigney, C. Laurent, A. Rousset, and C. N. R. Rao, Chemical Physics Letters **300**, 236 (1999).

[52]   H. Kathyayini, N. Nagaraju, A. Fonseca, and J. B. Nagy, Journal of Molecular Catalysis A: Chemical **223**, 129 (2004).

[53]   B. C. Liu, B. Yu, and M. X. Zhang, Chemical Physics Letters **407**, 232 (2005).

[54]   P. Coquay, A. Peigney, E. DeGrave, E. Flahaut, R. E. Vandenberghe, and C. Laurent, Journal of Physical Chemistry B **109**, 17813 (2005).

[55]   S. C. Lyu, B. C. Liu, C. J. Lee, H. K. Kang, C. W. Yang, and C. Y. Park, Chemistry of Materials **15**, 3951 (2003).

[56]   E. Flahaut, A. Peigney, C. Laurent, C. Marliere, F. Chastel, and A. Rousset, Acta Materialia **48**, 3803 (2000).

[57]   P. Ciambelli, M. Sarno, G. Gorrasi, D. Sannino, M. Tortora, and V. Vittoria, Journal of Macromolecular Science-Physics **B44**, 779 (2005).

[58]   W. Z. Zhu, D. E. Miser, W. G. Chan, and M. R. Hajaligol, Materials Chemistry and Physics **82**, 638 (2003).

[59]   P. C. Eklund, J. M. Holden, and R. A. Jishi, Carbon **33**, 972 (1995).

[60]   W. Z. Li, H. Zhang, C. Y. Wang, Y. Zhang, L. W. Xu, K. Zhu, and S. S. Xie, Applied Physics Letters **70**, 2684 (1997).

[61]   V. Georgakilas, D. Gournis, M. A. Karakassides, A. Bakandritsos, and D. Petridis, Carbon **42**, 865 (2004).

[62]   A. Kasuya, Y. Sasaki, Y. Saito, K. Tohji, and Y. Nishina, Physical Review Letters **78**, 4434 (1997).

[63]   L. Ci, Z. Zhou, X. Yan, D. Liu, H. Yuan, L. Song, J. Wang, Y. Gao, J. Zhou, W. Zhou, G. Wang, and S. Xie, J. Phys. Chem. B **107**, 8760 (2003).

[64]   H. Yan, Q. Li, J. Zhang, and Z. Liu, Carbon **40**, 2693 (2002).

[65]   M. Sveningsson, R. E. Morjan, O. A. Nerushev, Y. Sato, J. Backstrom, E. E. B. Campbell, and F. Rohmund, Applied Physics a-Materials Science & Processing **73**, 409 (2001).

[66]   M. S. P. Dresselhaus, M.A. Eklund, P.C. Dresselhaus, G., Springer Series in Materials Science **42**, 314 (2000).

[67]   S. Arepalli, P. Nikolaev, O. Gorelik, V. G. Hadjiev, W. Holmes, B. Files, and L. Yowell, Carbon **42**, 1783 (2004).

[68]   H. Ago, K. Nakamura, N. Uehara, and M. Tsuji, Journal of Physical Chemistry B **108**, 18908 (2004).

[69]   H. J. Jeong, K. H. An, S. C. Lim, M. S. Park, J. S. Chang, S. E. Park, S. J. Eum, C. W. Yang, C. Y. Park, and Y. H. Lee, Chemical Physics Letters **380**, 263 (2003).

[70]   R. Saito, A. Gru?neis, G. G. Samsonidze, V. W. Brar, G. Dresselhaus, M. S. Dresselhaus, A. Jorio, L. G. Canc?ado, C. Fantini, M. A. Pimenta, and A. G. Souza Filho, New Journal of Physics **5**, 157.1 (2003).

[71]   Y. Li, X. B. Zhang, X. Y. Tao, J. M. Xu, W. Z. Huang, J. H. Luo, Z. Q. Luo, T. Li, F. Liu, Y. Bao, and H. J. Geise, Carbon **43**, 295 (2005).

[72]   C. A. Furtado, U. J. Kim, H. R. Gutierrez, L. Pan, E. C. Dickey, and P. C. Eklund, Journal of the American Chemical Society **126**, 6095 (2004).

[73]   B. J. Landi, C. D. Cress, C. M. Evans, and R. P. Raffaelle, Chemistry of Materials **17**, 6819 (2005).

[74]   D. Bom, R. Andrews, D. Jacques, J. Anthony, B. Chen, M. S. Meier, and J. P. Selegue, Nano Letters **2**, 615 (2002).

[75]   N. Yao, V. Lordi, S. X. C. Ma, E. Dujardin, A. Krishnan, M. M. J. Treacy, and T. W. Ebbesen, Journal of Materials Research **13**, 2432 (1998).

[76]   T. Caruso, R. G. Agostino, G. Bongiorno, E. Barborini, P. Piseri, P. Milani, C. Lenardi, S. La Rosa, and M. Bertolo, Applied Physics Letters **84**, 3412 (2004).

[77]   R. Larciprete, A. Goldoni, S. Lizzit, and L. Petaccia, Applied Surface Science **248**, 8 (2005).

[78]   G. Chiarello, E. Maccallini, R. G. Agostino, V. Formoso, A. Cupolillo, D. Pacile, E. Colavita, L. Papagno, L. Petaccia, R. Larciprete, S. Lizzit, and A. Goldoni, Carbon **41**, 985 (2003).

[79]   O. Stephan, P. M. Ajayan, C. Colliex, F. CyrotLackmann, and E. Sandre, Physical Review B **53**, 13824 (1996).

[80]   G. Bongiorno, M. Blomqvist, P. Piseri, P. Milani, C. Lenardi, C. Ducati, T. Caruso, P. Rudolf, S. Wachtmeister, S. Csillag, and E. Coronel, Carbon **43**, 1460 (2005).

[81]   Ph. Lambin, A. Loiseau, C. Culot, L.P. Biro´, Carbon, **40** (2002) 1635–1648

3.2 Functionalized Carbon Nanotubes (f-CNTs)

3.2.1 Topic review and research motivations

CNTs have attracted particular attention for their unique structural, mechanical, and electrical properties and have extensive applications in many fields. For these reasons a lot of study have been made in order to modify and improve CNTs properties, in order to be much more interesting for applications. However, the manipulation and processing of CNTs have been limited by insolubility in most common solvents. Furthermore, CNTs tend to aggregate, and their non-uniform dispersion in common solvents and organic polymer matrices often results in unsatisfactory effects. Consequently, various methods have been proposed for functionalizing CNTs.

Functionalization of CNTs with polymers, for example, is gaining particular interest because the long polymer chains will help the tubes dissolve in good solvents even with a low degree of functionalization [12].

SWCNT-reinforced polymer composites have the potential to provide order-of magnitude increases in strength and stiffness relative to typical carbon-fiber reinforced polymeric composites. The mechanical behavior of nanotube/polymer composites depends not only on the individual properties of the polymer and the nanotubes, but also on the nanotube/polymer interaction [11].
Since in all semiconductor applications the properties of a device depend on the electronic states in the valence and the conduction bands, the control of the states in these bands is crucial to design and to optimize those devices. So, the future application of SWCNT's will depend upon the ability to modify their intrinsic properties by manipulation of their electronic structure. One route for modifying the solid state properties of SWCNT's is the addition of electron acceptors or donors or by electrochemical doping. Both methods change the solid state properties drastically. It was shown that the Fermi level can be shifted by electron or hole doping [14]. The doping can result in a significantly reduced electrical resistivity and work function. Some study [15-16] show that doping of SWCNT

(usually alkali–metals and the SWNT bundles form intercalation compounds) bundles is likely to be different from that of the multi-walled nanotubes (MWCNT) where alkali–metals can be intercalated between the adjacent shells within the same nanotube if defects are present. Furthermore, the electrochemical reactivity and the porosity make SWCNT bundles attractive host material for energy storage [13].

In this work we characterized the f-SWCNTs system in order to understand as much as possible about its properties. In this way we can try to make a comparison with the other nanostructured carbon-based systems and try to understand which one could be more interesting releated to the different applications.

3.2.2 Investigation and sample production techniques

The analyzed systems are indicated below:

Laponite/CNT/N/4 is a functionalized SWCNT intercalated into the interlayer space of an synthetic clay (Laponite, chemical formula: $(Si_8)^{IV}$ $(Mg_{5.48}Li_{0.52})^{VI} O_{20} (OH)_4 Na_{0.52}$).

DO3/39 samples are functionalized SWCNT containing metallic particles:

- ✓ DO3/39/5 SWCNT/Pyridine/Fe3Oy
- ✓ DO3/39/7 SWCNT/Pyridine/CoPt
- ✓ DO3/39/8 SWCNT/Pyridine/Co

The techniques we used to analyze the samples are similar to the previous time (UPS and SEM). Below we give a brief introduction about them indicating what they are useful for.

UPS: The Ultraviolet Photoemission Spectroscopy data were collected at the Spectromicroscopy beamline of the Elettra Synchrotron in Trieste. The photon

beam energy was 95.0 eV: this allows to collect the signal coming from the topmost surface layers with a penetration depth of less than 1nm.

The samples are micro- and nano-structured and, thus, the signal we recorded is relative to outer part of the particles assembled in the material. Further more, the photon energy allowed to excite the valence band electrons and some shallow core lines. On carbon-containing samples, we exploit the fact that at those energies the photoemission cross section of the C 2s and C 2p electrons is comparable and we get a complete picture of the C valence bands. The 2s and 2p cross sections are increasing with Z and then N and O are more clearly detectable.

On the other hand, the photoemission cross section of the *nd* valence electrons of the transition metals is much higher than those of C electrons and small amounts of those metals give very intense signal which can overshadow the C one.

A further complication is that, in general, it is not possible to analyze a non-conductive sample or a sample which is not grounded: the sample charging consequent of the photoemission process, will alter the spectra and no meaningful result can be obtained. Nevertheless, in particular conditions (low photon flux density, good ground connection) a reasonable signal can be recovered and it is possible to carry out an evaluation of the band gap and of the main valence band features.

SEM: We used an environmental-SEM to acquired images from the functionalized samples only because they gave unusual UPS spectra. The analysis of the induced fluorescence allowed us to depict the composition of each imaged particle. We used both high and low e-beam energies in order to probe different depths on the sample. Below it follows a sample-by-sample description and some considerations about them.

3.2.3 Photoemission Spectroscopy and Electron Microscopy results and discussion

The functionalization of SWCNT samples produce considerable changes in their electronic and morphological structure. In figure 1 we report an overview of the valance band structure of various samples as depicted by UPS. The photoelectron kinetic energy of the reported spectra is between 60 and 90 eV and, thus, in the minimum of the electron mean free path (mfp) in condensed matter, i.e. few Å. In materials with low density the mfp slowly increases because its dependence on the atomic density ρ is $mfp \approx \rho^{-\frac{1}{3}}$. This allows us to assign the observed electronic aspects to the outermost sample layers.
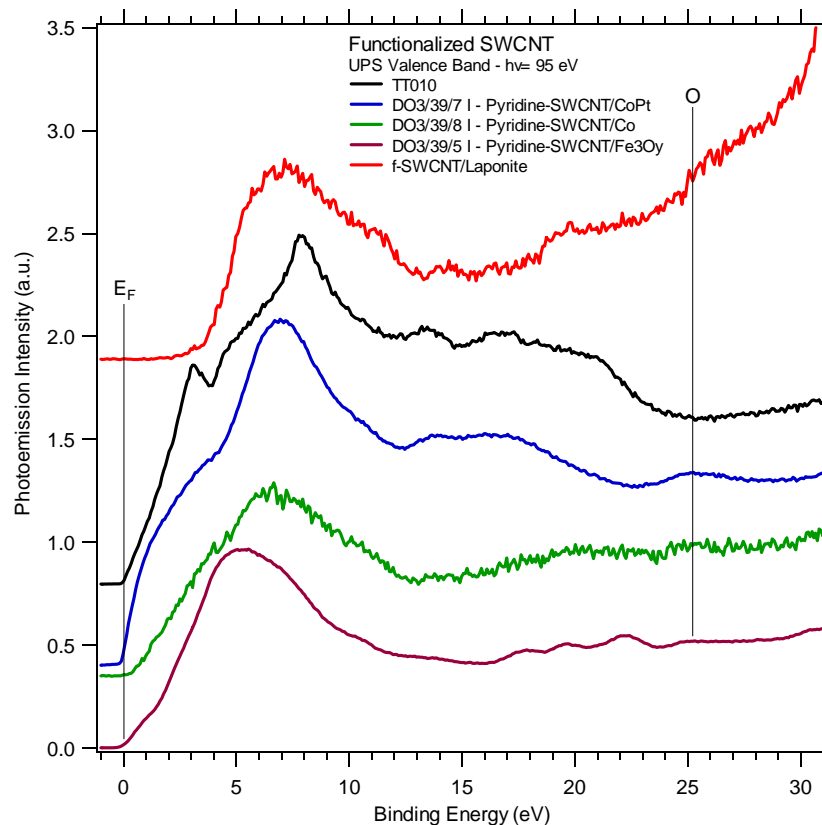
Figure 1. Valence band spectra of Pyridine-functionalized SWCNT containing metallic particles. The spectrum of a pure SWCNT (TT010) sample is shown for comparison.

DO3/39/8. Pyridine-SWCNT embedding transition metal particles show very different behaviors. The inclusion of Co results in a wide-gap semiconductor material and charging phenomena were observed during the measurement and we had to carefully check that no shifts were present between an acquisition sweep and the successive one. This did not allow us to collect a spectrum with high statistics. The shown spectrum (green line) shows a rather featureless shape with some meaningful characteristics: a) the maximum of the valence band lies at 6.5 eV; b) a ≈ 1 eV gap is present between the top of valence band emission and the Fermi level; c) a O 2s peak is discernible at 25 eV.

The SEM analysis of the same sample shows that is has a granular structure with typical dimension of 50 nm (see fig. 2). The high magnification SEM picture put in evidence the presence of bright features surrounded by a gray network. At low magnification (fig. 3), we can appreciate the presence of rare sticks which are typically 2 μm long and 100 nm wide.

The elemental composition of the sample, revealed by fluorescence analysis, is: C 75%, O 18%, Co 4% and traces of contaminants (mainly Cl). Our interpretation of the UPS and SEM data is that nanometric CoOx particles (clear particle in SEM pictures) are scattered in the Pyridine-SWCNT network. In fact, the spectroscopic results point out that the metallic particles are oxidized giving a wide gap around the Fermi Energy and a maximum of DOS at 6.5 eV due to the Co 3d-O 2p bonding states. Moreover, the presence of Co particle is producing a quite high oxidation of the Pyridine-SWCNT complexes (the O content is over-stoichiometric with Co). The material can be though as a semiconductor (oxidized Pyridine-SWCNT) embedding insulating CoOx particles. It remains to be addressed the presence of micrometric sticks which are most likely mainly formed of Co oxides.
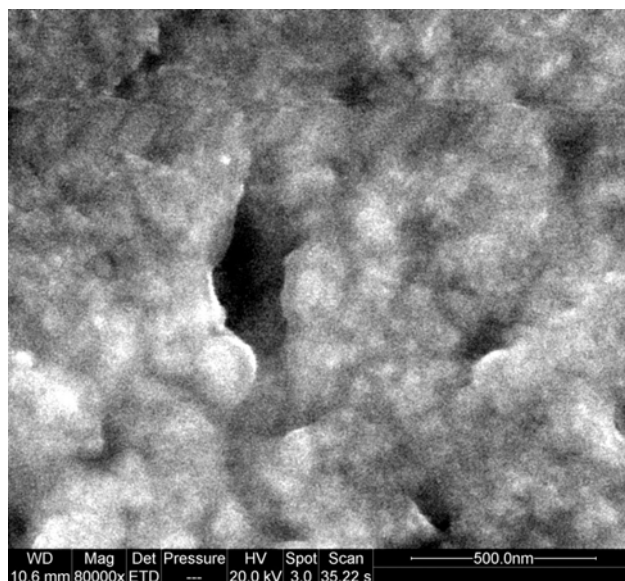
Figure 2. High magnification SEM image of the DO3/39/8 sample (Pyridine-SWCNT/Co).
A nanometric granular structure is present.
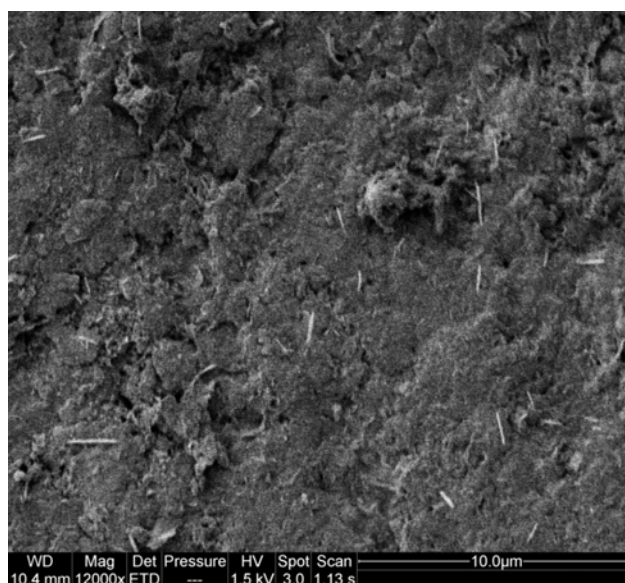
Figure 3. Overview of the surface of DO3/39/8 sample (Pyridine-SWCNT/Co).
Several rigid few-micron long sticks are present.

DO3/39/7. The Pyridine-SWCNT/PtCo sample is metallic (see blue line in fig. 1)
with a very high DOS around the Fermi level. The Co 3d/O 2p and O 2s peaks are
present at 7 eV and 25 eV, respectively, while a series of peaks, probably due to C
states, are present between 10 and 17 eV. The electronic states close to the Fermi

68

level are very probably those of Pt 5d (i.e. it remains catalytically active). No charging was observed on this sample allowing us to conclude that the whole material retains a quite high conductivity. In fact, even though the high DOS close to the Fermi edge could be ascribed to the Pt or Pt/Co particles, only the presence on a continuous conductive environment permits to avoid charging effects. The SEM images (fig. 4) of the sample revealed a very compact surface with some cracks. The sample composition is: C 90%, O 8%, Co/Pt 2% (Co/Pt ratio is 40:60) and various contaminant as Cl and Al and, in a minor extent, K, Ca, Na, As. Compared to the Co containing sample (see above), the Pyridine-SWCNT oxidation is lower in this case.

Several spherules are present on the surface (few μm wide) which show a different composition with higher content of O, Al and Cl and no Pt.

At very high magnification (fig. 5) it is possible to see that a granular morphology is present with a 20 nm typical dimension. Increasing the electron beam energy, it is possible to probe more deeply the sample getting the image of isolated metallic particles (fig. 6) which have the same typical radius.

Figure 4. Overview of the DO3/39/7 sample surface (128x100 micron) showing the compactness of the material and the presence of few-micron wide spherules.
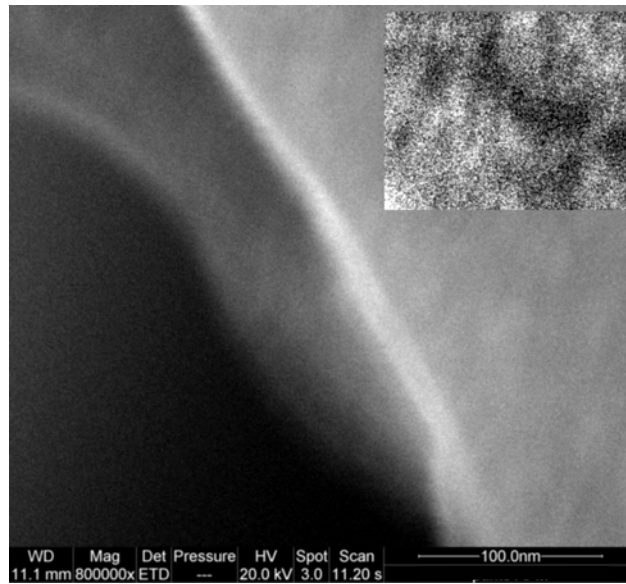
Figure 5. High magnification SEM image acquired on the border of a small fissure. The contrast of the upper right part of the image is enhanced in order to highlight the surface morphology.
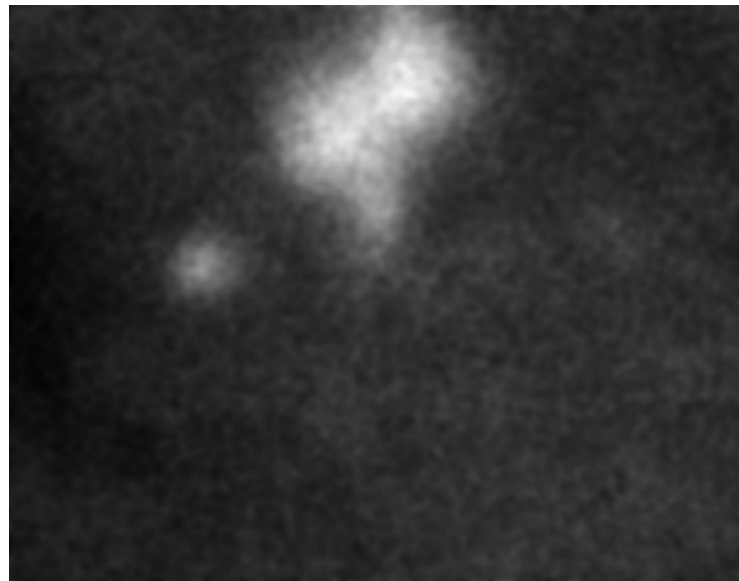
Figure 6. High magnification SEM image of a 400x312 nm surface region on DO3/39/7 sample showing the presence of isolated metallic particles.

DO3/39/5. The iron 3d levels contribution to the UPS spectrum of the Pyridine-SWCNT/FeO$_x$ sample is present as a broad peak centered at 4.5 eV. The shown spectrum (fig. 1) has a low intensity at the Fermi edge revealing a bad conductive

behavior. Several weak peaks are present on the high binding energy side of the main structure. We assign these peaks to the emission from O 2s and C 2s.

In different areas of the sample, charging effects took place and it was not possible to acquire a meaningful spectrum. We noticed that not all the features of the emission spectra move under the photon beam irradiation: only the strong Fe 3d emission is shifting while the energy of the C-related features remains unchanged. The spatial resolution of the Spectromicroscopy Beamline allowed us to collect spectra in region where no shifts induced by photoelectron emission are present and, in these conditions, we collected the shown spectrum.

A hint to clarify the observed facts is given by the fluorescence/SEM analysis. Sample is mainly made of nanometric platelets (see fig. 8) with an averaged composition of C 40%, Fe 20% and O 40%. Traces of Cl, K, Ni and Si contaminants are present too but their concentration is on the low ‰ range. We found in some regions the presence of a high concentration of thin rods (see fig. 9) whose dimensions are few *μm* long and few hundred *nm* long.

From the fluorescence analysis we found that their composition is compatible with a Fe_2O_{3-x} stoichiometry. Thus, it is possible that those iron oxide rods are responsible for the charging effects observed on UPS spectra while the C/Fe/O compound with flat morphology is mainly semiconductive.
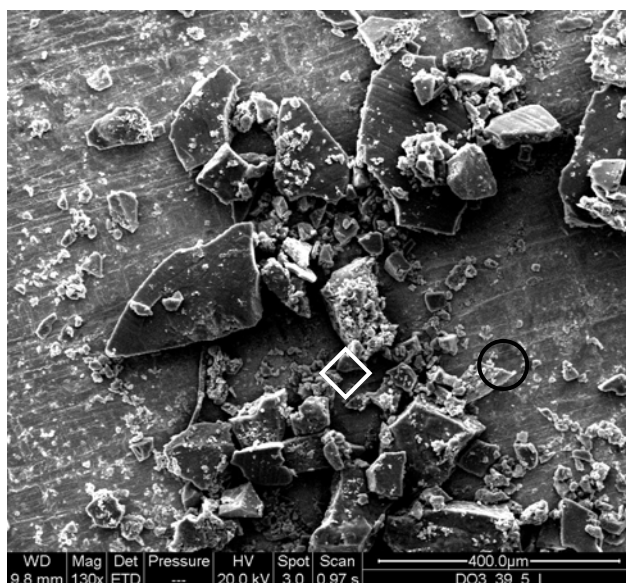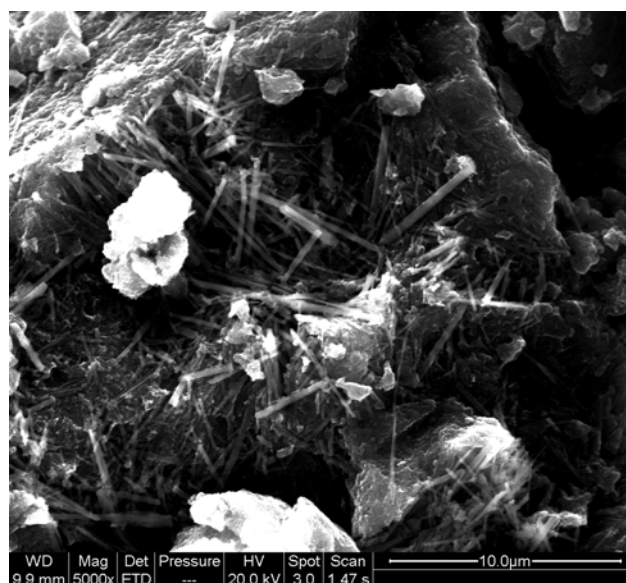

Figure 7. Very low magnification image of the DO/38/5 sample. A white square and black circle indicate the regions where the SEM image shown in figure 8 and 9 are respectively acquired.
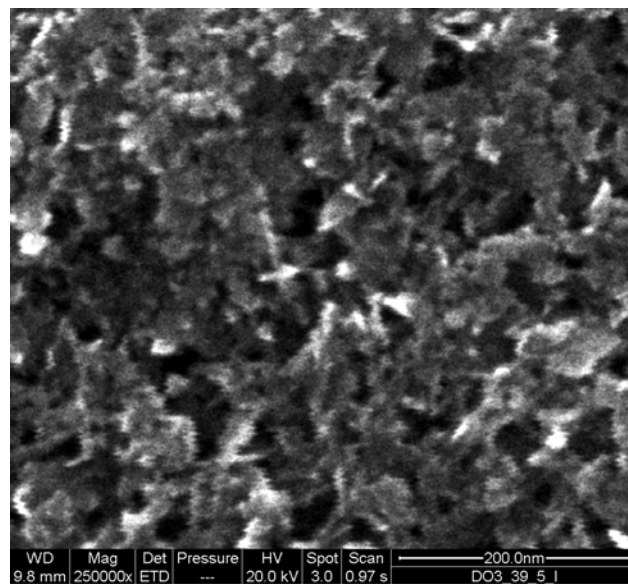
Figure 8. SEM image of a grain surface for sample DO3/39/5. It appears formed by platelets with tents of nm typical dimension.

Figure 9. Thin rods appearing in selected points on the surface. The imaged ones are relative to the area indicated by a circle in figure 7.

Laponite/CNT/N/4. The f-CNT intercalated into Laponite sample is highly insulator and this renders it very hard to be analyzed by UPS spectroscopy. An accurate search for a region in which discharging is possible (such as very thin layers of material) allowed us to collected the spectrum shown in figure 4 and reproduced in a larger energy region in the following figure. The spectrum does

not show any emission in the region between 0 and 1 eV in binding energy. Very low emission is present up to 4 eV and a series of well distinct peaks are present for higher binding energies. The identification of these structures is very difficult because of the manifold composition of the probed system and the lack of valence band studies in literature. As a speculative try, we can attribute the main features to the heavier elements (on the basis of the higher cross section of their external electronic shells) and to O (strongly present in the Laponite). As a matter of fact, the f-CNT material does not provide a conductive network (very similarly because it is insulator itself) and the whole sample remain insulator.
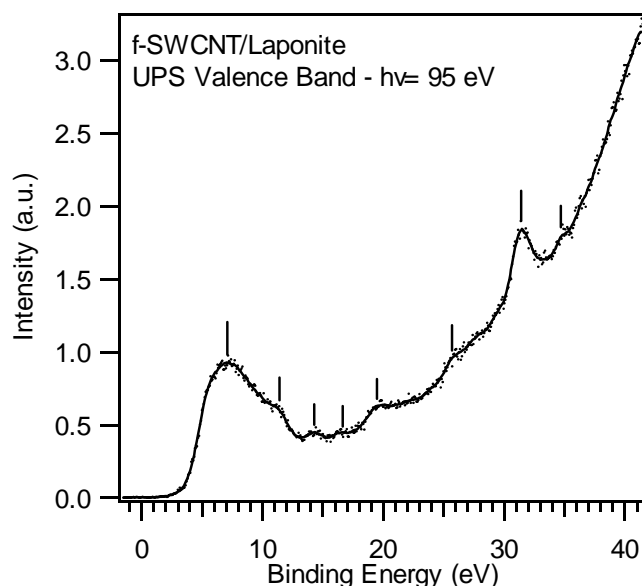
Figure 10. UPS spectrum of Pyridine-SWCNT/Laponite sample in an extended energy range. The smooth thin line is used as a guide for the eyes while vertical ticks mark the observed features.

3.2.4 Conclusion

Put together all SEM and UPS measurements we can characterize in a good way our samples. This characterization, connected with other future analysis (e.g. Raman, EELS, XRD), could improve our knowledge on these systems and at the same time suggest possible useful applications of them. We can conclude that,

depending on the metal particles embedded in the different samples, all of them show different behaviours. In fact we found that DO3/39/8 and DO3/39/5 show a semiconductive behaviour, while DO3/39/7 is metallic and Laponite/CNT/N/4 has an insulating characteristic. This means that CVD is however a good method for produce CNTs also if the quality, as already explained, is strictly related to catalyst particles. In fact we found that, different types and % of metal particles give rise to different systems.

3.3 Carbon Nanotubes grown by Silicon Carbide surface decomposition (CNTs by SiC)

3.3.1 New methods for the production of aligned carbon nanotubes

The growth of Carbon Nanotubes (CNTs) by Silicon Carbide (SiC) surface decomposition appears to be promising methods to scale up CNT production with accurate control using simple apparata working in Ultra High Vacuum (UHV) conditions. The growth of CNT is realized by making use of a single crystal SiC (Carbon terminated) heated at high temperature (~ 1400/1600°C) [1], by passing the current through the SiC substrate for few hours. The temperature of the substrate can be an important parameter for the quality of the growth CNTs.

In order to efficiently utilize the great properties of CNTs in applications such as photovoltaics, the problem of physical support of the CNTs must be overcome. The new frontier in photovoltaic devices is the development of molecular, polymeric and inorganic-organic hybrid thin film systems, because of their potential low-cost and easy processability [2] also, dye-sensitized-heterojunctions is one of the hotter subjects in the photovoltaic field.

Thinking beyond simple heterojunctions, the collection of the photo-separated charges can be improved by using nanostructured materials, as their high structural organization can increase charge separation and mobility by orders of magnitude. Specifically, by growing carbon nanotubes (CNTs) directly on substrates it is possible to avoid problems due to interfacial states while at the same time induce high charge mobility through a highly delocalized electronic structure.

The EEL spectroscopy is an experimental tool to determine the graphitization and the quality of the tubes [2] and in order to follow the electronic structure modifications, EEL (Electron Energy Loss) spectra were acquired during the heating procedure observing, as a function of the temperature, the evolution of the CNTs. In this experimental work, the electronic, chemical and structural

properties of synthesized carbon products are investigated by several experimental techniques (Electron Energy Loss (EEL), Raman Spectroscopy, Scanning Tunneling Microscopy/Spectroscopy (STM/STS) and Scanning Electron Microscopy (SEM)) and compared with experimental results recently obtained on single/multi –walled carbon nanotubes (SWCNT/MWCNT) [3, 4] as a function of the heating temperature and growth time.

3.3.2 Production techniques setting up and sample treatments

The investigated samples were grown by heating the SiC sample through current passage. Related to the resistance of the sample ($\sim K\Omega$) we used ~1 Ampere (~ 45 Volt). SiC substrate of 1 cm squared was utilized and heated in UHV at temperatures ranging between (1150-1550)°C. The final temperature was reached with steps of 100 °C. During this heating procedure it is important to avoid to stop the temperature value around 1000 °C, because graphitic layers can be formed, inhibiting CNT growth. Prior to the above mentioned heating procedure, the sample was annealed at ~ 400/500 °C for few hours to remove the contamination due to the air exposure of the sample surface.

The EEL and Auger spectra were acquired using an electron gun and hemispherical analyzer mounted in our UHV chamber. The SEM/EDX measurements were collected by FEI - Quanta FEG 400 F7. The STM/STS and Raman measurements were obtained by using a Schaefer microscope equipped in air and Raman microprobe Jobin-Yvon Labram (He-Ne laser - 632.8 nm emission).

### 3.3.3 Spectro-microscopic results

The EEL measurements were obtained by using an electron beam energy of 1000 eV. In this way, the signal coming out is from the topmost surface layers (~ 10-20 Å). In figure 1 the evolution of the EEL spectra as a function of temperature, during the heating of the SiC substrate to 1550 °C, are shown. All the spectra

show two main peaks at ~6 eV and ~23 eV characteristic of π and σ+π plasmon excitation [2]. Starting from the SiC substrate, the π plasmon, typical of graphitic-like structures, appears (fig. 1 (b)) and increase in intensity at higher temperature. In addition at higher temperature the π plasmon moves to higher energy. Recently was demonstrated that this excitation is at higher energy loss value in graphitic structures (graphite and CNTs) than amorphous carbon nanonostructures [3]. Since the upshift of the π plasmon show a good graphitization of the CNTs. In addition the increase of the intensity is compatible with an increase of CNTs amount and ordering. The increase of σ + π plasmon intensity is in agreement with the previous changes on π plasmon. The energy loss position of the π plasmon starts to move already at 1150 °C (fig. 1(b)) and it fixes its position at annealing temperature of 1400/1500°C (fig. 1(c)). After this temperature value only some changes in the peak intensity are observed.

However the good quality of CNTs is connected to the absence of the oxygen atoms which binds to the defect present in the CNTs structures. A direct prove of the absence of these contaminants on the surface of the CNTs is given by Auger measurements (not shown here) which exclude the presence of oxygen contaminants. In addition the EDX measurements show only the presence of Carbon and Silicon atoms.

The acquisition of SEM images and the analysis of the EDX results allows to study the morphology and contemporary the chemical composition of the samples. The SEM images were acquired with an accelerator voltage of 20 kV and X-ray fluorescence spectra were acquired in the energetic range 0-10 keV in order to obtain the bulk elemental composition of the samples.

At lower magnification (fig. 3a) a very packed and rough surface is observed. The inset of figure 3 shows the profile of the growth CNTs which have micrometric length (~ 400 nm). The CNTs seem to have different characteristics throughout the sample: in some areas the film is high ~ 400/500 nm whereas in other areas they are less high. The difference in length can depend in the temperature gradient along the sample. In both case however, the film is very uniform and packaged.
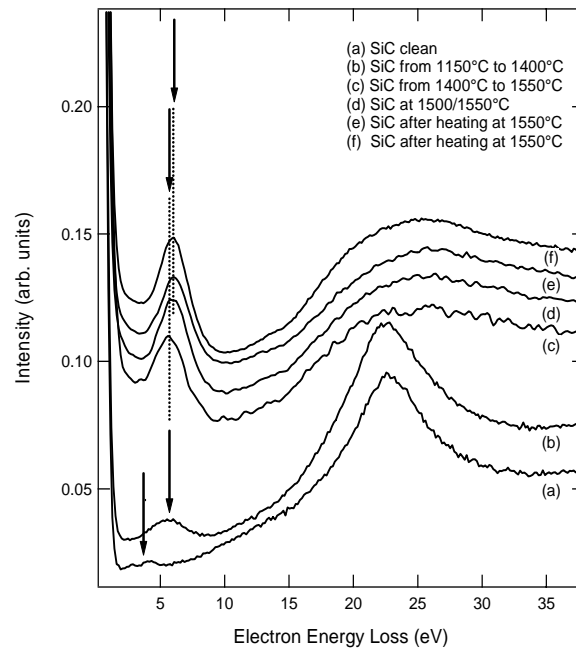
Figure 1. EEL spectra of SiC and CNTs growth by SiC substrate. The image show the spectra changes step by step with the temperature and how the CNTs grow up.

In order to have clearer SEM images along the CNTs axis mechanical defects were induced (figure 3b at lower magnification and figure 3c and 3d at higher magnification). It is obvious from images 3c and d the high packaging of CNTs

From SEM imaging and from magnification some isolated CNTs can be distinguished, and an approximated estimation gives a diameter size of few nanometer (2-10 nm) and length of few micron.

The EDX spectra acquired on different areas of the sample show an average chemical composition of C 88,67 % and Si 11,33%.

The same analysis was carried out in thinner part of the sample, probably due to smaller temperature on this area. In this case we found average composition of C 82,60 % and Si 17,40%. The bigger amount of silicon is due to the higher signal detected from the analyzer coming from the substrate. However both of EDX data exclude the presence of oxygen.

Obviously, silicon signal is connected to the substrate of SiC because the electron beam energy is 20KeV which penetrates the film of CNTs (~100 nm).

The Scanning Tunneling Microscopy/Spectroscopy (STM/STS) measurements were carried on the same sample. The STM images of CNT on SiC were acquired

in different region of the sample where the CNTs laid on the substrate (see fig. 4a) perpendicular to the substrate (see fig. 4b,c,d). The figure 4a shows CNTs of (2.5-3.5) nm which are in agreement with the size of the CNTs cap shown figures 3c, 4c and 4d. At higher areas, the morphology of CNT is flat (see fig. 4b). The black region does not give the idea of the sample roughness. In fact the profile of the sample along the arrow in figure 4b is reported in figure 5 showing a height difference of ~4nm between the arrow ending points. The magnification of that area gives an idea of the bigger structures present in figure 4b (see fig. 4c).

The figures 4c,d and the inset of figure 4d show circle-like structure with an average diameter of 2 nm. Those structures are attributed to the CNTs caps.

(a) CNTs on SiC (60000 X) – Inset 120000 X

(b) CNTs on SiC 16000 X – Mechanical defects

(c) CNTs on SiC (160000 X) – Inset 1200000 X

(d) Package film of CNTs on SiC (240000 X)
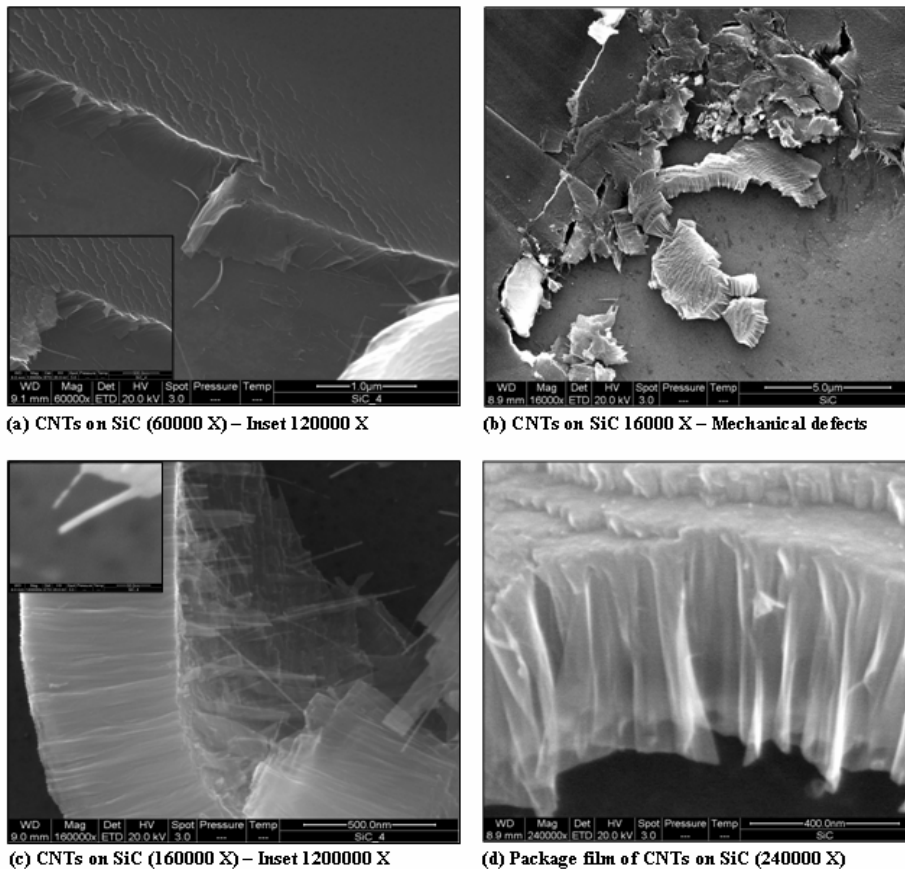
Figure 3. SEM image of the CNT samples grown by SiC. (a) All the samples show a very packed surface morphology with a micrometric length scale. (b) Mechanical cut of the layer allows us to perform the morphological characterization of the of its inner side. (c), (d) High magnification images showing carbon nanotubes and the package structure close to the surface.
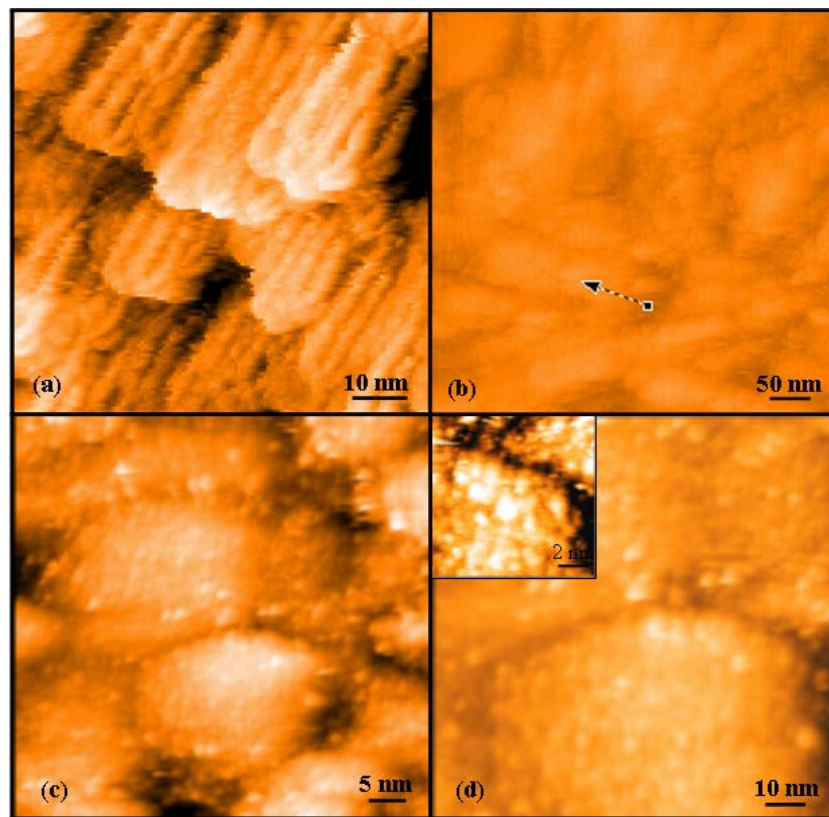
Figure 4. STM image of the CNT samples grown by SiC. (a) Topography 65x65 nm of CNTs laid on SiC, (b)STM topography acquired with set point 0.1 nA and 4 V. The differents between the two is :(a) In the former the CNTs laid on the substrate (b) area where the CNTs were straight to the substrate. Note the roughness of the surface. (c), (d) STM topography acquired with set point 0.1 nA and 4 V. Both show circle-like structure with an average diameter of 2 nm (inset in (d)). Those structures are attributed to the CNTs caps.
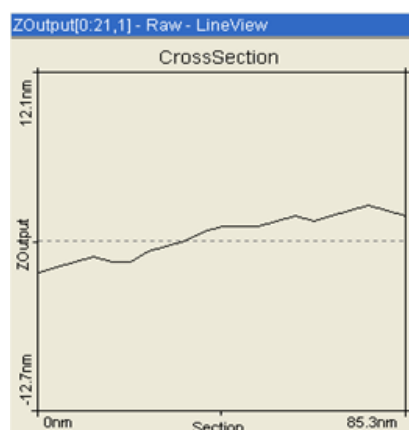
Figure 5: cross section in figure 4b along the arrow

The STS is, somehow, connected to the STM and we can relate to each structure obtained in the STM image a I-V characteristic curve of the sample.

By using simple models characteristic electronic properties of the sample like the band gap value, the Density of the States (DOS) shape can be extracted from the I-V curve utilizing peculiar models [4-7].

In general the sample shows everywhere I-V diode-like characteristic curve (see fig. 6). In figure 7 the normalized conductance of the samples is plotted.

The I-V curves presented a bias which was eliminated by centring the gap in the normalized conductance to the zero bias voltage, (the zero bias voltage represents the Fermi Level). In figure 7 the line at normalized conductance equal 1 is traced. In fact at this value we can measure the gap of the sample, because in metals the normalized conductance close to the Fermi Level is 1. So, from this value, we can have an estimation of the gap for the semiconductors. In the present case, the cap of the tube presents a gap value of 1.4 eV. In addition we can see a narrow DOS in the occupied electronic states which can explain the high tunnelling current at negative voltage shown in figure 6.

The measured tunnelling current from the STM depends also from the mobility of the carrier along the CNTs. In fact at negative voltages the electron tunnels from the tip to the CNTs while in the positive sample bias the hole are carried from the CNTs. Since the electron mobility in the CNTs should be higher then the hole mobility.

When we apply negative sample bias we probe the empty states of the sample where the DOS (see fig. 7) has a single intense peak. Probably in this part of the DOS the carrier collision time and then the mobility are higher. In contrast at positive sample bias the carrier collision time is higher.
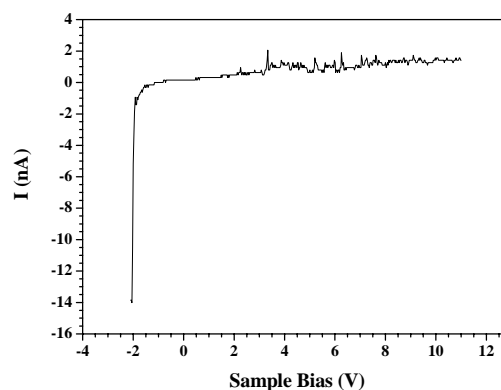
Figure 6. I-V characteristic curve of the sample.
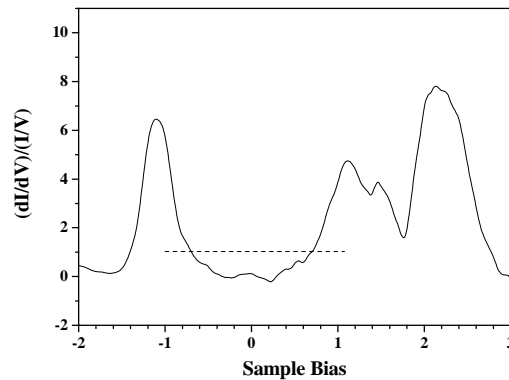
Figure 7. Normalized conductance of the
sample.

How we had already mentioned before, a good help to understanding our system comes from the Raman spectroscopy.

Raman Spectra have been collected by a Raman microprobe Jobin-Yvon Labram. A He-Ne laser (632.8 nm emission) has been used as source. A 100x Mplan Olympus with Numerical Aperture of 0.90 objective has been used in order to collect the spectra. The power of the laser out of the objective, was about 5 mW and the focused laser spot was about 2-3 μm of apparent diameter. The resolution of the reported Raman spectra can be estimated, with some excess, to be 2 cm^{-1}.

The representative optical images collected on the sample are shown in figure 8. In figure 9 are reported representative Raman spectra corresponding to the sample zones shown in figure 8. The range 200-1000 cm^{-1} is reported in figure 9a, and the one between 1000 and 1900 cm^{-1} in figure 9b. As it is possible to see in figure 9a, only the spectrum collected on the (f) zones shows Raman features at about 768, 789 and 967 cm^{-1} and a shoulder at 798 cm^{-1}. Such bands have been assigned to the silicon carbide substrates. This means that the layer of the deposited film on the (f) zone is much thinner than that present on the others zones.

In detail, the observed pattern is assigned to a well crystallized layer of Lely 6H-SiC [8] where the A_1 (LO) band falls at 967 cm^{-1}, the two TO (E_2) bands appear at 768 cm^{-1} and 789 cm^{-1} and the E_1 planar mode is detectable as a shoulder at about 798 cm^{-1}[9]. The absence of the radial breathing mode at lower wave number excludes the growth of SWCNTs, in agreement with SEM and STM images.

The spectra obtained at higher frequency region (fig. 9b) confirm the differences between the (f) and the others zones.

All the spectra show Raman features at about 1328 (strong), 1580 (strong) and 1615 (shoulder) cm^{-1} (see fig. 9b) attributed to the presence of multiwall carbon nanotubes (MWCNTs) and multiwalled nanofibers (MWNFs) [10]. However the spectrum (f) shows additional features. In fact, as it can be seen in figure 10, where the fitting results are shown, different Lorentians functions have been used in order to reconstruct the experimental spectrum. Remarkable peaks are at ~1544, ~1559 and ~1587 cm^{-1} that, with the weak band at ~1700 cm^{-1}, they can be assigned to the presence of single wall carbon nanotubes (SWCNTs) [11]. Also the bands at 1532 cm^{-1} [12-14] and at 1515 cm^{-1} [15] can be associated to SWCNTs, while the last band at 1481 cm^{-1} can indicate the presence of other carbon form, in fact it is similar to that observed on the Raman spectra of finite size molecular domains of condensed aromatic ring [16].
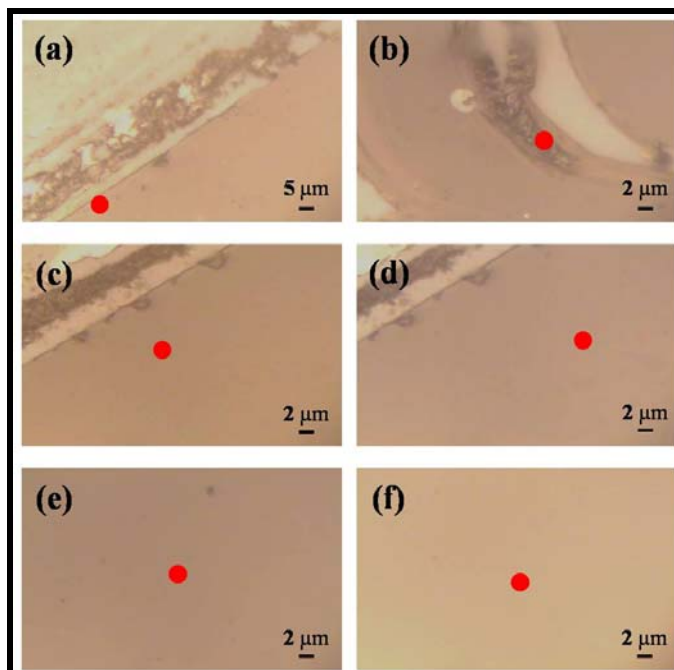

Figure 8. Representative optical images collected by the microscope. The red circle indicate the laser spot relative to the spectra shown in the following figures.
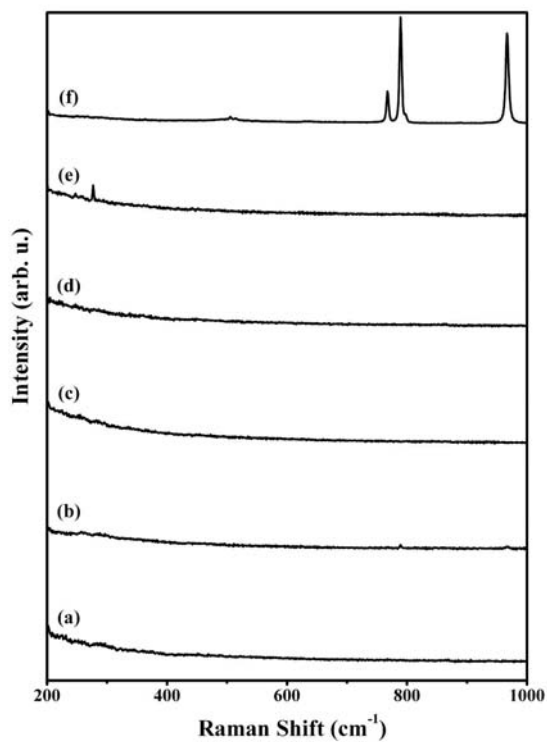
Figure 9a. Representative Raman spectra between 200 and 1000 cm^{-1} collected on the different spots shown in figure 8.
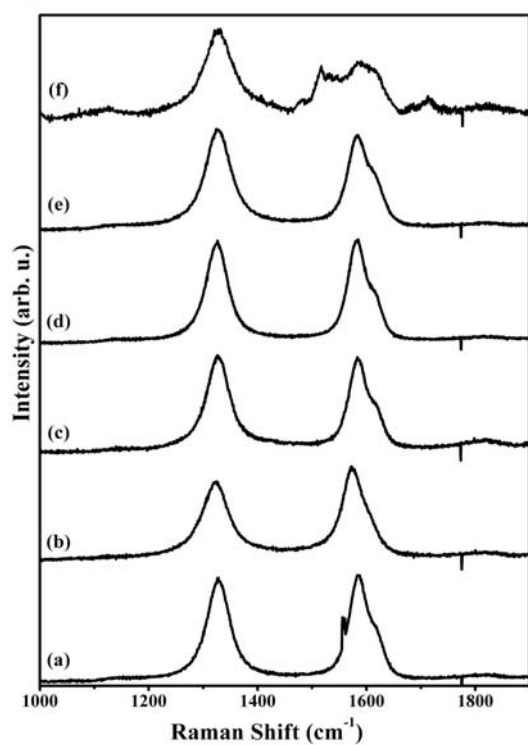
Figure 9b. Representative Raman spectra between 1000 and 1900 cm^{-1} collected on the different spots shown in figure 8.
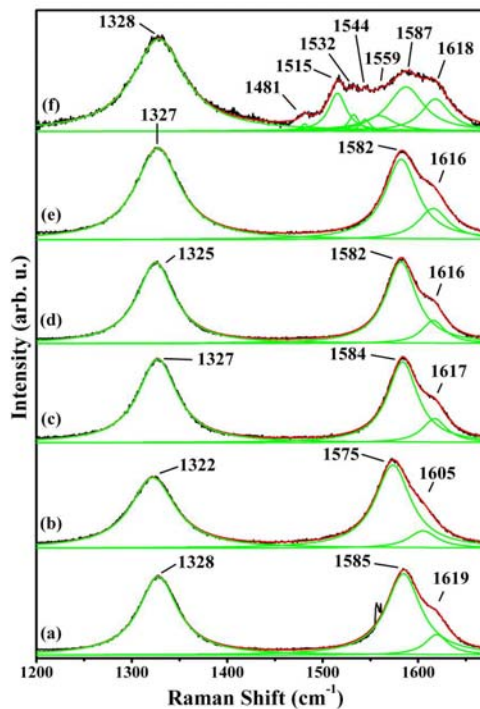
Figure 10. D and G Raman bands collected on the zones indicated in figure 8. The black lines are experimental data; the green lines are the single Lorentzian bands and the red line is the total fitting curve.

3.3.4. Concluding remarks

CNTs grown by SiC surface decomposition are very packaged on the surface, as we can see in the SEM and STM images. In addition the EEL spectra show the good quality of the sample. The Auger and EDX spectra confirm this quality from the absence of oxygen signal. All of those technique and Raman spectroscopy exclude the presence of SWCNTs. However the diameter of the tube measured by STM and the Raman peaks indicate a small number of the carbon walls. The investigated samples show a diode-like behaviour depending on the sample bias and in particular it shows electron collector behaviour. In the future we plan to deposit a gold electrode to use this system as an electron electrode collector in solar cells devices.

3.3.5 References

[1]   M. Kusunoki, T. Suzuki, T. Hirayama, N. Shibata - *Physica B 323 (2002) 296–298.*

[2]   G. Chiarello, E. Maccallini, R.G. Agostino,V. Formoso, A. Cupolillo, D. Pacile, E. Colavita,L. Papagno, L. Petaccia, R. Larciprete ,S. Lizzit , A. Goldoni - *Carbon 41 (2003) 985–992.*

[3]   R.G. Agostino et al. - *Phys. Rev. B 68, 035413 (2003).*

[4]   Bardeen, J. - *Physical Review Letters 1961, 6, 57.*

[5]   Tersoff, J.; Hamann, D. R. - *Phys. Rew. B 1985, 31, 805.*

[6]   Hansma, P. K.; Tersoff, J. - *Journal of Applied Physics 1987, 61, r1.*

[7]   Stroscio, A. J.; Kaiser, W. J. – *Scanning Tunneling Microscopy; Academic Press:San Diego, 1993.*

[8]   M. Dudley, W. Huang, S. Wang, J. A. Powell, P. Neudeck and C. Fazi; *J. Phys.D: Appl. Phys.,* **28,** A56 (*1995*).

[9]   M. W. Russel, J. A. Freitas Jr., W. J. Moore and J. E. Butler; *Advanced Materials for optics and Electronics,* **7,** 195 (*1997*).

[10]   L. Delzeit, I. McAninch, B. A. Cruden, D. Hash, B. Chen, J. Han and M. Meyyappan; *Journal of Applied Physics,* **91,** 6027 (*2002*).

[11]   L. Song, L. Ci, C. Jin, P. Tan, L. Sun, W. Ma, L. Liu, D. Liu, Z. Zhang, Y. Xiang, S. Luo, X. Zhao, J. Shen, J. Zhou, W. Zhou and S. Xie; *Nanotechnology,* **17,** 2355 (*2006*).

[12]   S. Chiashi, Y. Murakami, Y. Miyauchi and S. Maruyama; *Thermal Science & Engineering,* **7,** 10 (*2000*).

[13]   A. M. Rao, E. Richter, S. Bandow, B. Chase, P. C. Eklund, K. A. Williams, S. Fang, K. R. Subbaswamy, M. Menon, A. Thess, R. E. Smalley, G. Dresselhaus, M. S.Dresselhaus; *Science,* **275,** 187 (*1997*).

[14]   E. Cazzanelli, M. Castriota, G. Mariotto and J. M. Rosolen; *Surfaces Engineering,* **19,** 454 (*2003*).

[15]   M. A. Pimenta, A. Marucci, S. A. Empedocles, M. G. Bawendi, E. B. Hanlon, A. M. Rao, P. C. Eklund, R. E. Smalley, G. Dresselhaus, M. S. Dresselhaus; *Physical Review B: Rapid Communications,* **58,** R16016 (*1998*).

[16]   C. Mapelli, C. Castiglioni, E. Meroni and G. Zerbi; *Journal Of Molecular Structure,* **80-481,** 615 (*1999*).

3.4 Tin filled Carbon Nanotubes (Sn@CNTs)

3.4.1 Topic review: carbon covered metallic nano-wires

Carbon nanostructures possess important properties derived from a combination of unique dimensional, structural and topological features. This opportunity is given from the ability of carbon atoms to have orbital hybridization [1]. Carbon nanotubes (CNTs), along with fullerenes, represent the most characteristic example of this family of materials. Electronic conductive or semiconductive behaviour, excellent mechanical strength, stiffness and elasticity, low density, high thermal conductivity, open pipe framework and relative chemical inertness render carbon nanotubes outstanding materials for various potential technological applications [2].

Moreover, the characteristic inner cavity in submicron and nano-dimensions renders them suitable as a host material [3,4]. Indeed, the inherent pore structure of carbon nanotubes has already been explored as a confined space for encapsulation and stabilization of various elements or compounds [5-7]. Towards this aim, recently [8] we reported a simple and reproducible method which yields individual micrometer-long carbon nanotubes filled with highly pure, single crystalline, superconducting tin nanowires. Furthermore, it is known that the in-situ filling of the inner hollow cavity can induce changes in the graphitic structure and therefore to modify the CNT properties. Especially, the electronic properties of CNTs can be changed due to the introduction of Stone Wales defects which can change and tune properly the electronic properties of CNTs [9,10].

In this work Single- and Multi-Wall Carbon Nanotubes are compared with CNTs filled with Sn in order to investigate the effect of filling in morphological and electronic properties of the produced CNTs. The morphology was investigated by Scanning Electron Microscopy (SEM) and Scanning Tunneling Microscopy (STM) while the electronic properties were investigated by Scanning

Tunneling Spectroscopy (STS). In addition Raman spectroscopy was acquired to evaluate the quality of the carbon samples.

3.4.2 Sample production procedures and probing techniques

The synthesis of unfilled CNTs was carried out by the Catalytical Chemical Vapour Deposition (CCVD) method. In detail, Fe-Co bimetallic catalysts supported on MgO were prepared according to a previously reported method [11]. A quantity of 100 mg of the as prepared powder was placed in an alumina crucible within a quartz tube, located in a horizontal tubular furnace. The sample was heated up to the desired temperature under nitrogen atmosphere. When the required temperature was achieved, acetylene as a carbon precursor was admixed with the carrier gas (nitrogen) at flow rates of 10 cm^3/min and 90 cm^3/min, respectively. SWCNTs were grown at 800 °C for 30 min using a low metal loading (1% wt Fe and 1% wt Co in MgO) catalyst while MWCNTs were obtained under the same conditions using a higher metal loading (5% wt Fe and 5% wt Co in MgO) catalyst [12,13]. After the completion of acetylene flow, the ceramic boat was cooled down to room temperature under nitrogen atmosphere and finally, the deposited materials were collected from the ceramic boat.

Tin filled carbon nanotubes (Sn@CNTs) were grown at 700 °C in the same experimental apparatus by the catalytic decomposition of acetylene over tin-dioxide catalyst (Aldrich, 99.9%) using the same quantity of catalyst, the same flow rates and argon as carrier gas [8].

Scanning electron images were recorded using a scanning electron microscope (SEM) Quanta FEG 400 (FEI). The SEM images were acquired with an electron beam of 20 keV and X-ray fluorescence spectra were acquired in the energetic range 0-10 keV with an Energy Dispersive X-ray Detector (EDX) in order to obtain the bulk elemental composition of the samples. The images provide the typical morphology of the samples powders deposited on carbon tape. Scanning Tunneling Microscopy/Spectroscopy (STM/STS) measurements were performed at RT in air with a Schaefer STM using Pt/Ir tips. In order to perform

the STS/STM measurements, the CNTs powder was dispersed in acetone and a small drop of the suspension was left to dry in air on graphite. For STS measurement the feedback control of piezoelectric motor was suspended and the tip-to-sample current was recorded while a voltage ramp from −1 to +1 V was applied. Raman spectra were recorded with a Micro-Raman system RM 1000 RENISHAW using a laser excitation line at 532 nm (Nd-YAG). A beam power of 0.5 to 1 mW was used with 1 μm focus spot in order to avoid photodecomposition of the samples.

3.4.3 Morphology and electronic characterization

SEM images of the as prepared samples show a bundled structure (see fig. 1).
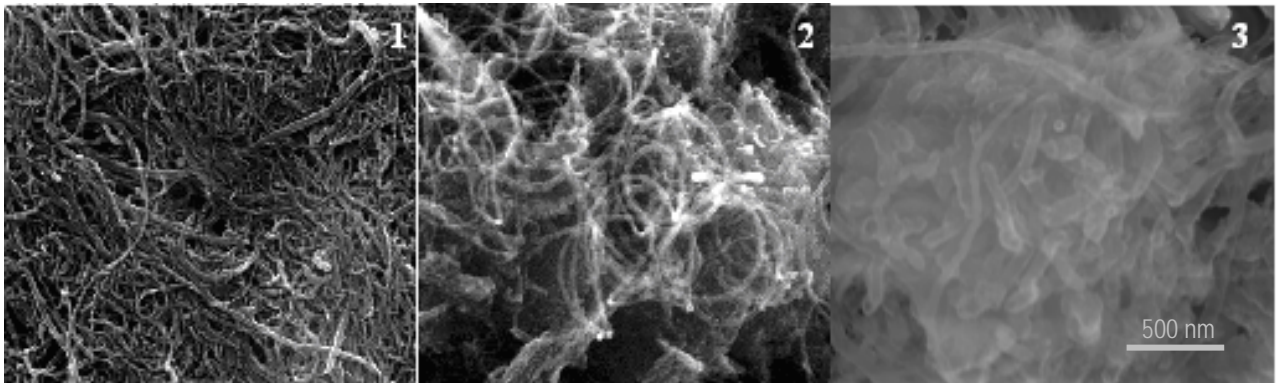
Figure 1. SEM images of samples SWCNT (1), MWCNT (2) and Sn@CNTs (3) showing carbon nanotubes bundles as the main constituents of the samples.

The unfilled CNTs (images 1 and 2) show straighter and smoother structures and do not show any considerable defect. On the contrary the Sn@CNTs sample shows pronounced defects in the structure with drastic changes in the curvature. The different curvature of the CNTs can be attributed to the Sn nanowires encapsulation as the filled MWCNTs have curvature effects on pressure-induced buckling [14]. As a consequence, changes in the chemical and physical properties of the filled carbon nanotubes are expected.

The elemental analysis performed acquiring the fluorescence spectra can be used to detect the texture and the purity of the analyzed samples and to determine the residual amounts of catalysts and support material. SWCNTs present fewer amounts of metal catalysts (less than 5 %at) while amounts up to 25 %at are present in MWCNTs. The catalytic particles maintain their stoichiometry and are finely dispersed among the graphitic network.

The main constituent atoms of Sn@CNTs sample are C (74 %), Sn (16 %) and O (10 %) which correspond to carbon deposits (mainly CNTs encapsulating Sn), encapsulated Sn and remaining unreacted catalyst and the copper oxide of the sample holder. On the other hand the higher ratio of Sn compared to O indicates the successful encapsulation of Sn into CNTs, as during the CNTs growth the encapsulated tin transforms from SnO_2 to β-Sn phase [8].

A very powerful method for the characterisation of CNTs is Raman spectroscopy, as it has been reported for both single-wall (SWNTs) and multi-wall carbon nanotubes (MWCNTs) [15-17]. Figure 2 shows the Raman spectrum of the SWCNTs, MWCNTs and Sn@CNTs samples. All spectra are characteristic for the respective carbon nanotubes. In the spectrum of SWCNTs we observe the presence of the Radial Breathing Mode (RBM) bands at lower Raman shift corresponding to the A_{1g} "breathing" mode of the tubes [18] and attributed to CNTs with small diameters (less than 3 nm) [19]. On the contrary, Raman spectra of MWCNTs and Sn@CNTs did not show any RBM peaks suggesting that the grown carbon nanotubes have a higher number of graphitic walls. In the Raman-shift range 1200–1800 cm^{-1}, two peaks are observed at 1350 and 1595 cm^{-1} corresponding to graphite D- and G-bands, respectively. The G-band corresponds to the tangential stretching (E_{2g}) mode of highly oriented pyrolytic graphite (HOPG) and can be used to assess the degree of crystallinity/graphitisation, while the D-band at 1354 cm^{-1} originates from disorder in the sp^2-hybridized carbon atoms, characteristic for lattice distortions in the curved graphene sheets and/or tube ends [20,21]. The relative intensity of D and G bands (I_D/I_G), reveals the degree of disorder and it was found to be 0.24, 0.69 and 0.86 for SWCNTs, MWCNTs and Sn@CNTs respectively. The I_D/I_G ratio is lower in the case of SWCNTs indicating that resulting carbon nanotubes exhibit limited disorder. The

ratio is much higher in the case of unfilled MWCNTs (0.69) while the presence of Sn within the inner cavity results to more defective graphitic structure leading to further increment of the recorded I_D/I_G ratio (0.86). Indeed, the presence of tin induces a softness of CNTs structure giving rise to the observed curvature defects in the SEM image of figure 1.
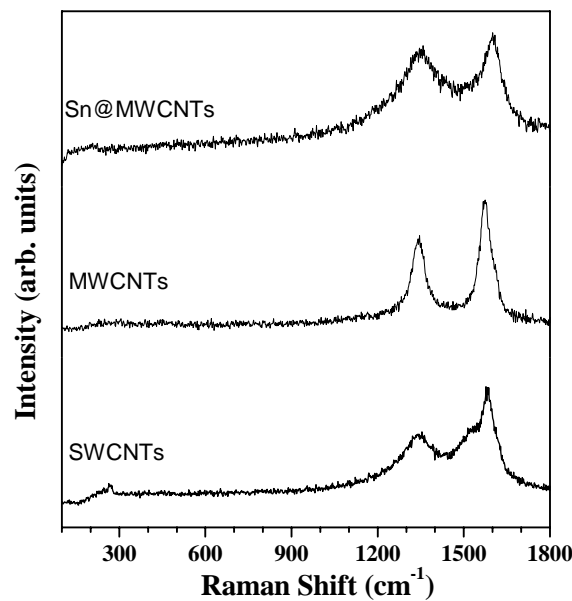
**Figure 2.** Raman spectra of SWCNT, MWCNT and Sn@CNTs.

Finally, STM/STS results show the difference in the Local Density of States (LDOS) of CNTs. The STM topography of sample 1 and 2 show CNTs with diameter of 1.4 nm and 2.6 nm. STM topography of Sn@CNTs shows CNTs with higher diameter (in average 12 nm). The unfilled SWCNTs and MWCNTs present, usually, a straighter structure along the axis while the Sn@CNTs show a bended structure in agreement with SEM (shown above) and TEM images [8].

On the CNTs shown in figure 3 the I-V characteristic curves were obtained (see fig. 4). The data were processed depending on simple models to get the normalized conductance which is, at first approximation, proportional to the Density of States (DOS) of the sample surface [22].

91
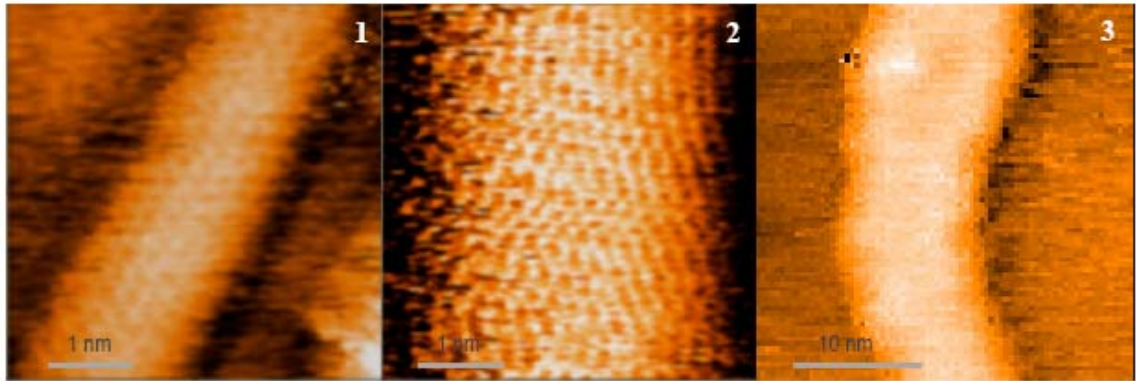
Figure 3. STM images of SWCNT (1), MWCNT (2) and Sn@CNTs (3). The topographies were acquired with set point 0.2 nA and 0.2-0.5 V. (1) Topography 4.5x4.5 nm and (2) topography 4.4x4.4 nm and (3) topography 29.5x29.5 nm.

The I-V curve was also obtained for Highly Oriented Pyrolitic Graphite (HOPG) and was used as a reference. The band gap is almost zero in HOPG while it is larger, up to 0.1 eV, in the CNTs samples. This indicates that the CNTs are semiconductors and their band gap depends not only on their diameter but also on the incorporated metal. In fact, Sn@MWCNT sample presents clearly an additional state to the band gap near the zero sample bias (Fermi Level). The presence of this state was interpreted as the result of defects presence in the CNTs structure [23] confirming the findings from the SEM, Raman and STM measurements which indicate the presence of a more defective structure.
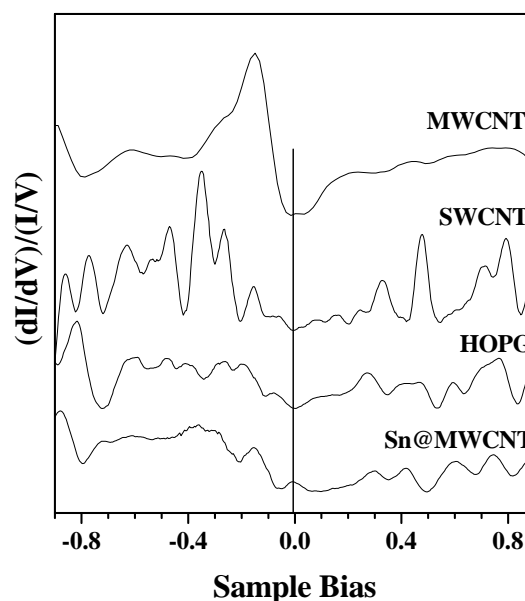
Figure 4. Normalized conductance obtained in the topographies of figure 3.

3.4.4 Concluding notes

In conclusion, the insertion of soft metals like Sn inside the CNTs gives pronounced curvature changes and consequently induces changes in the electronic properties of the sample close to the Fermi Level. The encapsulation of the metals in the inner cavity of CNTs can bend easily the nanotube structure and thus tune their electronic properties. This is an important finding that could expand the potential application of CNTs for the development of novel electronic devices.

3.4.5 References

[1]   Dresselhaus, M. S.; Dresselhaus, G.; Eklund, P. *Science of Fullerenes and Carbon Nanotubes*; Academic Press: San Diego, 1996.

[2]   Baughman, R. H.; Zakhidov, A. A.; de Heer, W. A. *Science* **2002**, *297*, 787.

[3]   Barborini, E.; Lenardi, C.; Piseri, P.; Milani, P.; Agostino, R. G.; Caruso, T.; Colavita, E.; La Rosa, S.; Bertolo, M.; Ducati, C. *European Physical Journal D* **2003**, *24*, 273.

[4]   Bongiorno, G.; Lenardi, C.; Ducati, C.; Agostino, R. G.; Caruso, T.; Amati, M.; Blomqvist, M.; Barborini, E.; Piseri, P.; La Rosa, S.; Colavita, E.; Milani, R. *Journal of Nanoscience and Nanotechnology* **2005**, *5*, 1072.

[5]   Monthioux, M. *Carbon* **2002**, *40*, 1809.

[6]   Chiarello, G.; Maccallini, E.; Agostino, R. G.; Caruso, T.; Formoso, V.; Papagno, L.; Colavita, E.; Goldoni, A.; Larciprete, R.; Lizzit, S.; Petaccia, L. *Physical Review B (Condensed Matter and Materials Physics)* **2004**, *69*, 153409.

[7]   Agostino, R. G.; Caruso, T.; Chiarello, G.; Cupolillo, A.; Pacile, D.; Filosa, R.; Formoso, V.; Colavita, E.; Papagno, L.; Ducati, C.; Barborini, E.; Lenardi, C.; Bongiorno, G.; Piseri, P.; Milani, P. *Physical Review B (Condensed Matter and Materials Physics)* **2003**, *68*, 035413.

[8]   Jankovic, L.; Gournis, D.; Trikalitis, P. N.; Arfaoui, I.; Cren, T.; Rudolf, P.; Sage, M. H.; Palstra, T. T. M.; Kooi, B.; De Hosson, J.; Karakassides, M. A.; Dimos, K.; Moukarika, A.; Bakas, T. *Nano Letters* **2006**, *6*, 1131.

[9]   Koloczek, J.; Brodka, A.; Burian, A.; Dore, J. C.; Honkimaki, V.; Kyotani, T. *Diamond and Related Materials* **2006**, *15*, 1036.

[10]   Lambin, P.; Mark, G. I.; Biro, L. P. *Physical Review B* **2003**, *67*.

[11]   Tsoufis, T.; Xidas, P.; Jankovic, L.; Gournis, D.; Saranti, A.; Bakas, T.; Karakassides, M. A. *Diamond and Related Materials* **2007**, *16*, 155.

[12]   Policicchio, A.; Caruso, T.; Chiarello, G.; Colavita, E.; Formoso, V.; Agostino, R. G.; Tsoufis, T.; Gournis, D.; La Rosa, S. *Surface Science* **2007**, *601*, 2823.

[13]   Policicchio, A.; Tsoufis, T.; La Rosa, S.; Caruso, T.; Maccallini, E.; Chiarello, G.; Colavita, E.; Formoso, V.; Gournis, D.; Agostino, R. G. *Carbon (in prepration)* **2007**.

[14]   Qian, H.; Xu, K. Y. *Acta Mechanica* **2006**, *187*, 55.

[15]   Georgakilas, V.; Gournis, D.; Karakassides, M. A.; Bakandritsos, A.; Petridis, D. *Carbon* **2004**, *42*, 865.

[16]   Karakoulia, S.; Jankovic, L.; Dimos, K.; Gournis, D.; Triadafyllidis, K. *Studies in Surface Science and Catalysis* **2005**, *158*, 391.

[17]   Dresselhaus, M. S.; Eklund, P. C. *Advances in Physics* **2000**, *49*, 705.

[18]   Arepalli, S.; Nikolaev, P.; Gorelik, O.; Hadjiev, V. G.; Holmes, W.; Files, B.; Yowell, L. *Carbon* **2004**, *42*, 1783.

[19]   Ago, H.; Nakamura, K.; Uehara, N.; Tsuji, M. *Journal of Physical Chemistry B* **2004**, *108*, 18908.

[20]   Eklund, P. C.; Holden, J. M.; Jishi, R. A. *Carbon* **1995**, *33*, 959.

[21]   Li, W. Z.; Zhang, H.; Wang, C. Y.; Zhang, Y.; Xu, L. W.; Zhu, K.; Xie, S. S. *Applied Physics Letters* **1997**, *70*, 2684.

[22]   Stroscio, A. J.; Kaiser, W. J. *Scanning Tunneling Microscopy*; Academic Press: San Diego, 1993.

[23]   Carroll, D. L.; Redlich, P.; Ajayan, P. M.; Charlier, J. C.; Blase, X.; DeVita, A.; Car, R. *Physical Review Letters* **1997**, *78*, 2811.

3.5 Carbon Nanocolumns (Nc-C)

3.5.1 State of the art

Over the past few years, the interest for the nano-sized C-based materials has received a growing interest, due to peculiar properties that may lead to several applications in electronic devices and sensors. Furthermore, recently, it was shown that carbon-based hard materials, such as diamond-like carbon and carbon nitride thin films, can be used as protective coatings, due to high wear resistance, low friction and high elasticity combined with high hardness [1,2], as dielectrics, due to high resistivity and breakdown fields in metal–insulator–semiconductor (MIS) devices [3] and for display applications, since the incorporation of nitrogen was shown to improve the field emission from amorphous carbon (a-C) [4]. The C–N thin film system, obtained by magnetron sputtering, has been observed mainly in the amorphous phase or in a fullerene-like structure, depending on the growth parameters (i.e. temperature and deposition rate). In the present work we report the growth of a new kind of C nanostructures, by radio-frequency (RF) magnetron sputtering technique, C deposition is performed using a graphite cathode as material source, on a Si(100) substrate covered with SiO2 (22 nm thick) and with Ni (10 nm thick).

Our interest is related to their properties, and especially to see if different substrate means different Nc-C properties. We would like to understand if substrate covered with metal particles gives different results compare with no metal substrate in the growth of carbon nanofibers [5,6]. In this work we report on the electronic and chemical structure of synthesized carbon products analyzed by valence band photoelectron spectroscopy (UPS) and scanning electron microscopy (SEM).

3.5.2 Apparata, sample preparation and treatments

Carbon deposition has been performed by RF-magnetron sputtering, using a 99.999% pure graphite target as material source. The substrate used for the deposition was a Si(100) substrate covered with SiO2 (22 nm thick) and with Ni (10 nm thick).

Such kind of substrate is useful in order to observe whether a different growth takes place on silicon dioxide and on nickel during the same deposition process. The base pressure in the vacuum chamber was 2 x 10^5 mbar; the sputter gas (nitrogen, argon or a mixture of both) was then introduced into the chamber, reaching an operating pressure of 2 x 10^2 mbar. Several deposition processes were performed, using a plasma generated by applying RF power in the range between 100 and 250W. During the deposition process the substrates were kept at a fixed temperature value in the range 400–600 °C. Our samples were product with this process at the CNR-IMM in Catania and they are named as XVI and XX. Below, for each sample, we indicate all growth conditions.

XVI

- ✓ Deposition @ 400 °C
- ✓ Time deposition = 4 hours (power 100Watt)
- ✓ Substrate: SiO2 22nm / Si (100)

XX

- ✓ Deposition @ 400 °C
- ✓ Time deposition = 4 hours (power 100Watt)
- ✓ Substrate: Ni islands / Si (100)
- ✓ Ni islands: 10 nm deposited on Si + HF 25% for 10 minutes
         and annealing @ 700 °C for 1 hour

SEM measurements were done as pre-characterization in order to see what kind on nanocolumns we had. Because in this way can collect morphological and chemical (Energy Dispersive X-ray analysis - EDX) information about our samples. As we will show, the Nc-C film seems to be very package and only where we created some mechanical defects by cutting the film, is possible to look at the carbon columns.

UPS measurements were acquired at the BeamLine SpectroMicroscopy at Elettra Syncrotron Light Source with an energy photon beam of 95 eV in order to get information from the topmost layers (penetration depth of few nanometers).

Each samples is analyze in more than one point trying to understand how it is structured and eventually showing chemical and morphological different across the sample itself. For the same reason we acquired not only UPS spectra but also some maps (spatially-resolved photoemission spectroscopy). In the following paragraph showing our results we will speak about "*focalized*" and "*de-focalized*" beam. When we say "*focalized* beam" it means that the spot on the sample is 0-0,5 μm, while "*de-focalized* beam" means a spot with a dimension > 0,5 μm.

3.5.3 SEM, UPS results

UPS spectra were acquired in different position in order to map all the sample. As we already explained, a complication in UPS measurements comes from the difficult in analyze the non-conductive sample or sample which are not grounded. This because the sample charging consequent of the photoemission process alter the spectra. Nevertheless, in particular conditions (low photon flux, good ground connection) a reasonable signal can be recovered and its possible to carry out an evaluation of the band gap and of the main valence band features. It follows a sample-by-sample descriptions and some considerations.

<u>Sample XX</u>: In order to start the investigation of our samples, we collect SEM image to record information on their morphology and on their chemical composition. Figure 1 shows a very packed and uniform nanocolumns film.

Mechanical defects are necessary to get a lateral image of the carbon nanostructures. Figure 2 shows a different area with the same structures confirming the uniformity of the film.
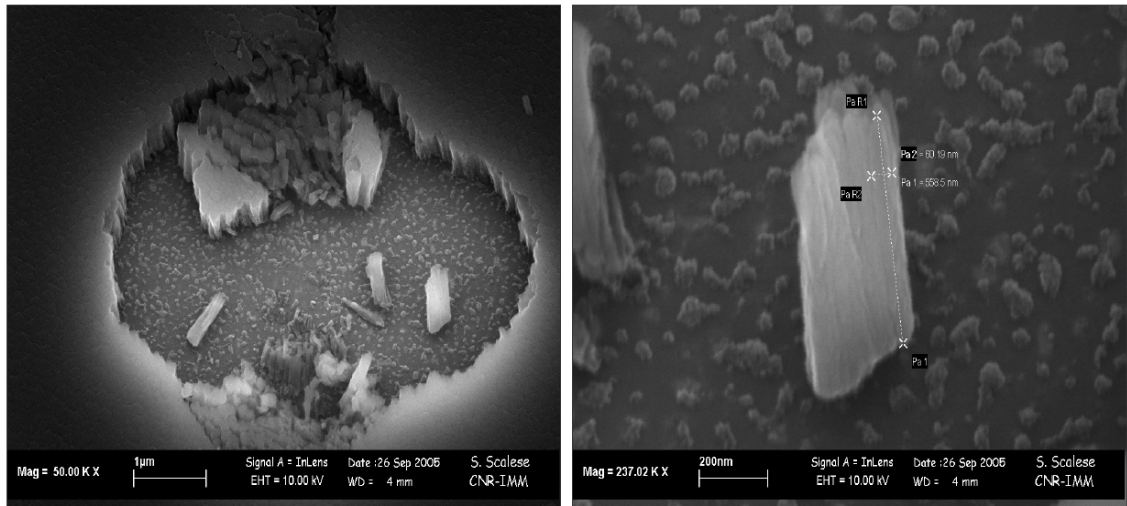
Figure 1. SEM image of sample XX. On the left is shown an area where there is a mechanical defect created in order to see the nanostructured columns. On the right a detail inside the area (carbon nanostructured laid on the substrate and some cluster on the surface - Images acquired by Dr. S. Scalese – IMM-CNR Catania [7,8])
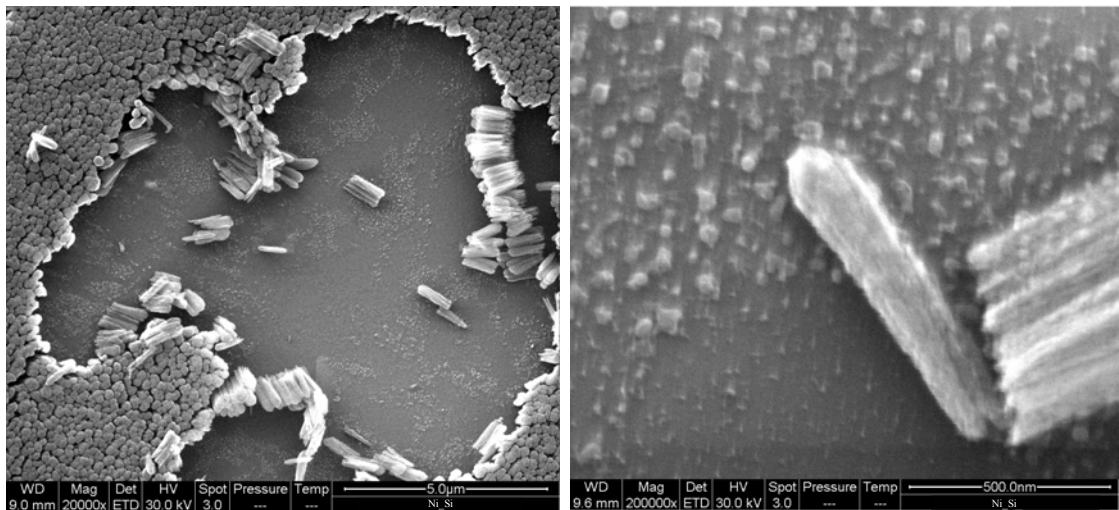
Figure 2. SEM image in a different area of XX sample. On the left there is a natural defect, on the right a detail inside the areas. It shows a carbon nanostructured laid on the substrate, and some cluster on the surface.

The previous pictures (fig. 1 and 2) give an idea of the morphology of the Nc-C films. In both pictures, on the Si substrate's surface, we can distinguish free from

carbon nanostructures, some *Ni* clusters with dimensions of few nanometers (see below).

We estimated diameter of the carbon nanostructures is ranging from ~130 to ~170 nm and a length of 500/600 nm, while on nickel clusters we found typical area value in the 100-300 nm^2 range and a mean diameter equal to 20-40 nm. We also evaluate that the typical distance between two nickel clusters is ~ 120/130 nm.

A verification of chemical composition of the surface features comes from EDX analysis. In fact, collecting spectra in different points, we tracked the atomic % of various elements and inside with particular attention to the nickel signal. In three different position on the surface we found:

- ✓ C = 78,66 % and N = 21,34 %   (Nc-C top surface)

- ✓ C = 78,78 % and N = 21,22 %   (Nc-C top surface)

- ✓ C = 5,95 %, Si = 93,7 %, Ni = 0,35%; (On the substrate surface)

Depending on the analyzed area, the samples show different behaviours. In some areas acquiring UPS measurements, we note that the spectrum changes and/or shifts during the acquisition (fig. 3 and fig. 4). According to the previous paragraph, this means that in the considered areas the sample is not conductive, showing therefore semiconductive or insulator characteristics and that some photo-induced processes are happening. The picture below are referred at the same area, but they show two different beam condition. In figure 3 we have a de-focalized beam while in figure 4 the beam is focalized. Looking at the spectra, it seems that an evolution of the sample under the beam takes place or, to be more precise, the sample is modifying under the photon flux (the structures at 79 eV and ~ 75 eV moves to higher kinetic energy).
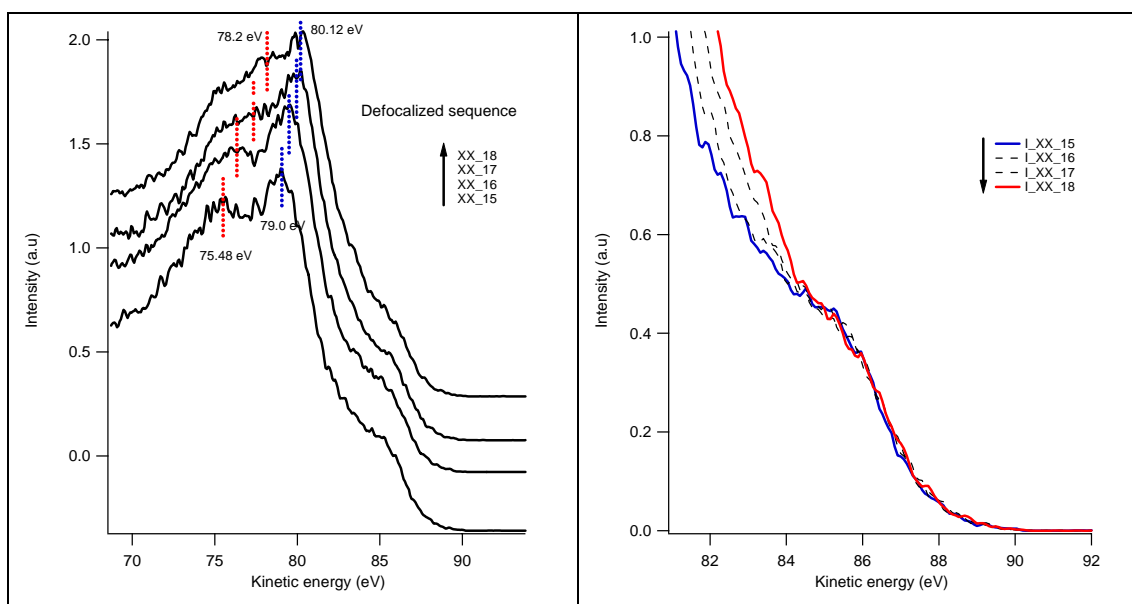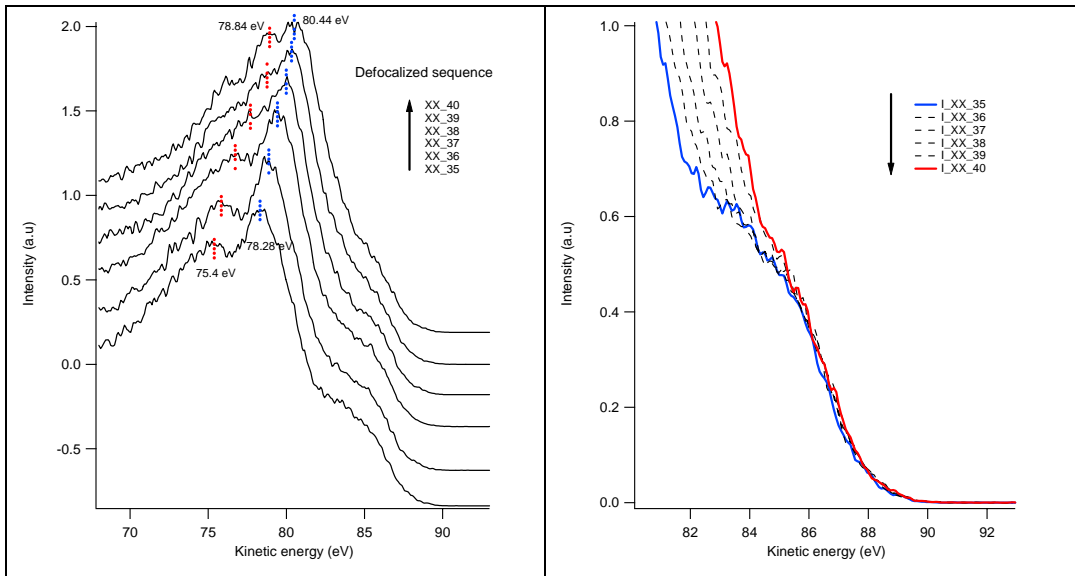
Figure 3. The picture show: on the left the small temporal evolution of the sample under the photon beam (hν = 91,5 eV) (acquisition time = 160s/scan). On the right: no changes at Fermi level in the range 81-92 eV.
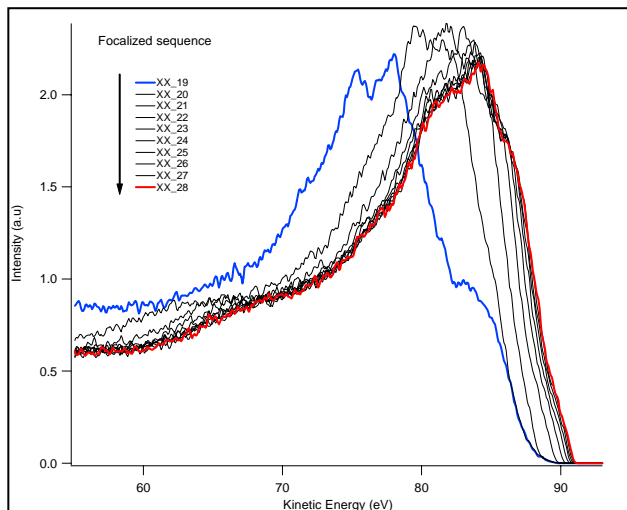
**Figure 4**. Charging and photochemical effects under the photon beam (hν = 91,5 eV). The structures shift to higher kinetic energy (acquisition time = 85s/scan) while the overall lineshape is changing.

Blue and red line are respectively initial and final behaviour of the sample.

We acquired some other UPS spectra in different positions (fig. 5 and fig. 6) in order to observe and describe eventually differences.

Figure 5. The picture show: on the left the small temporal evolution of the sample under the photon beam (hν = 91,5 eV) (acquisition time = 160s/scan). On the right show no changes at Fermi level.
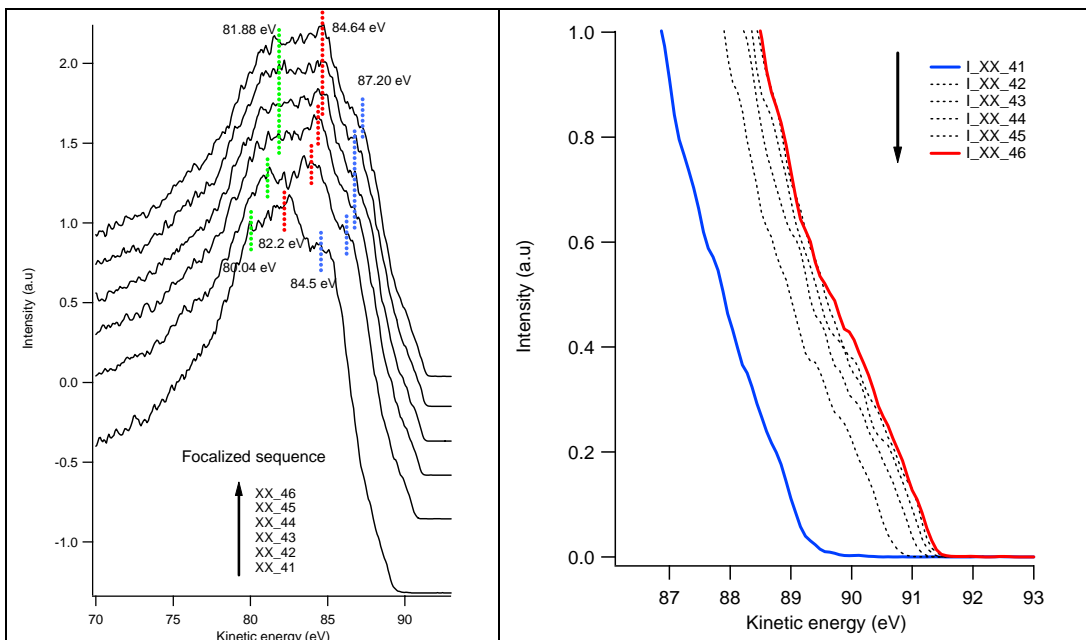

Figure 6. Effects of focalized beam (hν = 91,5 eV) on the sample (acquisition time = 160s/scan). The region is the same as in figure 5. The structures moves to higher kinetic energy (left). Range 86-93 eV (right), the picture show changes at the Fermi level. Blue and red line are respectively initial and final behaviour of the sample.

In both pictures (fig. 5 and 6) we observe the temporal evolution of the sample under the photon beam. In figure 5 where we have a defocalized beam, we find

the same behaviour as in the previous area (see figures 3 and 4). In figure 6 (focalized beam) the spectral evolution is different. In fact, comparing it with figure 3 and 5, we observe changes near the Fermi level (K.E.= 91,2 eV) with an intensity increase that can be related to the augmentation of the metallic behaviour of the exposed area.

This information leads to the conclusion that we are collecting a signal from an area with no nanostructured materials i.e. from the substrate. Therefore the typical metallic emission near the Fermi level is justified with the presence of nickel islands.

As explained before, in order to evaluate the chemical and morphological properties of the sample, we acquired also some photoemission maps (spatially-resolved photoemission signal recording). As an example, we show some of the collect data in figures 7 and 8.
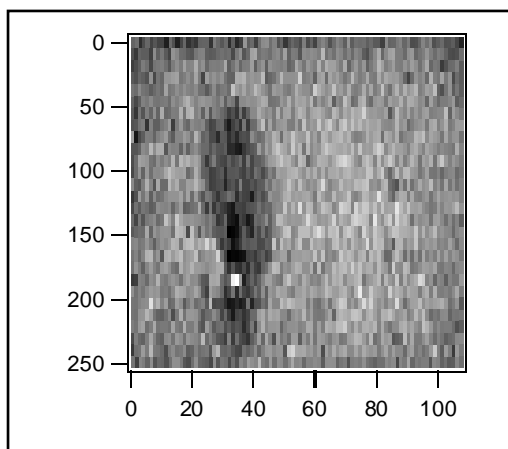
Figure 7. Map acquired on the sample with kinetic energy = 83,6 eV. The image is 100x100 μm wide.
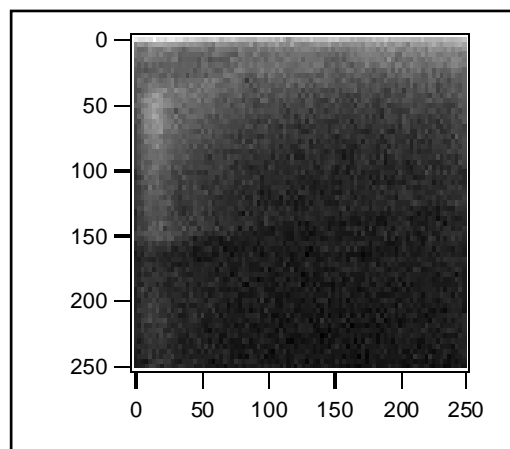
Figure 8. Map acquired on the sample with kinetic energy = 76,6 eV. The image is 100x100 μm wide.

The map shown in figure 8 is uniform: there are no particular structures or other differences that can suggest a chemical or structural non uniformity of this area. On the contrary, in figure 7, we can clearly distinguish a dark zone on a white background. In this case the dark zone is connected with a minimum in correspondence with the kinetic energy used for acquire the map, and on the contrary the white zone is related to a maximum in the energy.

These differences can be related to chemical or morphological changes in the analyzed zone. In order to better understand the cause we should take into account the ratio of the signal on the different channels. In this way is possible to increase all the information about the systems.

Sample XVI: Similarly to the XX sample, we found changing behaviours related to the different analyzed area on the sample. According with the previous analysis we can say that the XVI sample show conductive, semi-conductive or insulating behaviour depending on the analyzed zone.

Looking at figure 9 and 10 (SEM measurements) we note that also in this case the film is package and uniform. Therefore, the only way to observe some structure is to find some natural defect (see fig. 10) or create mechanical defect (see fig. 9).
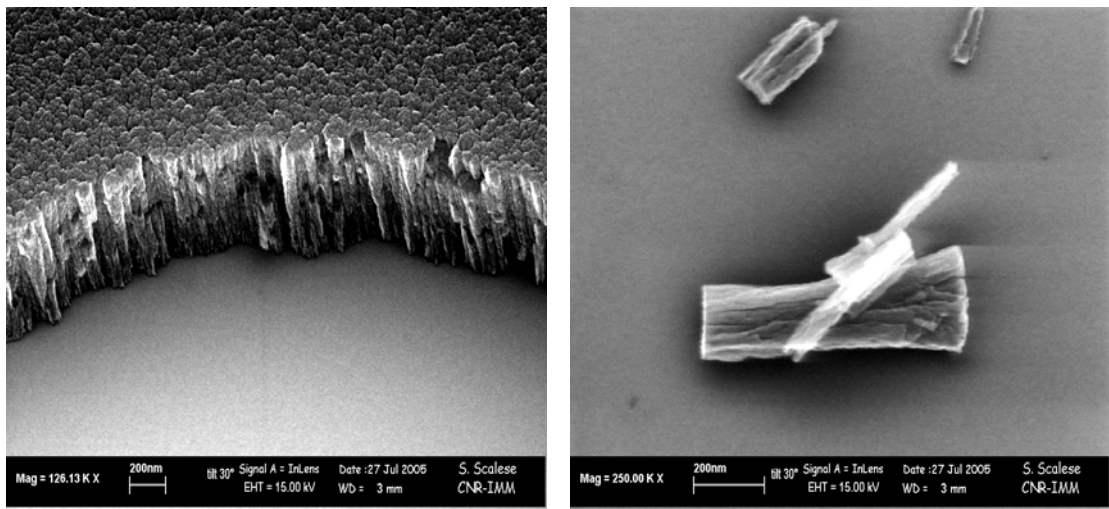
Figure 9. SEM image of sample XVI. On the left is show a nanostructured film closest to a mechanical defect created in order to see the nanostructured columns. On the right a detail inside the area (carbon nanostructured laid on the substrate - Images acquired by Dr. S. Scalese – IMM-CNR Catania [7,8]).
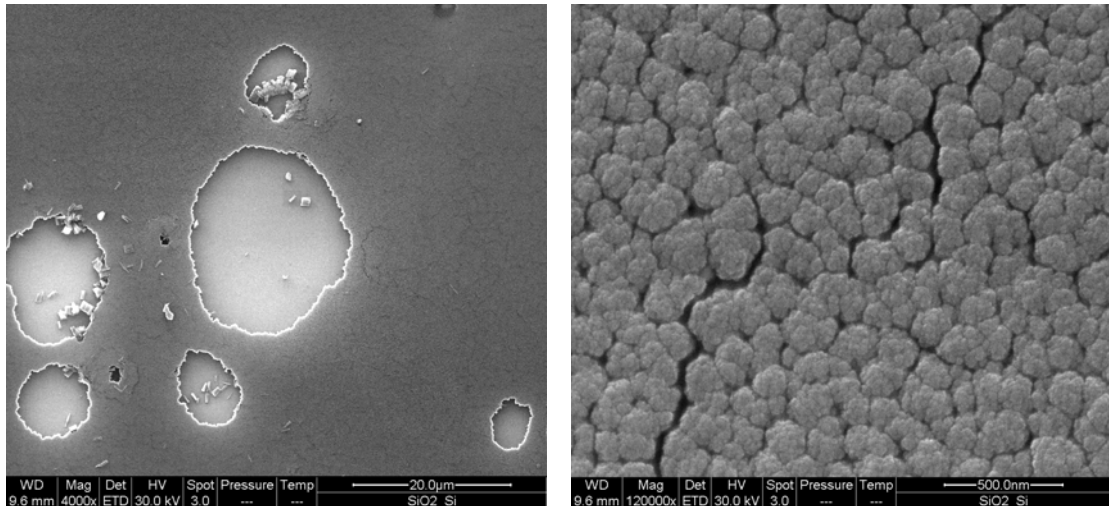
Figure 10. SEM image of sample XVI different area. On the left are shown defect on the
nanostructured film. On the right a top view of the film.

Also in this case carbon nanostructured columns have length of 500/600 nm,
diameters ranging from 200 to 300 nm, and caps with a typical areas dimension
of 20000/30000 nm^2 (see fig. 3 and fig. 10).

If we compare this picture with the sample XX we note that in this case there is no
presence of clusters on the surface. This because XVI sample is growth directly
on a SiO2/Si substrate, without the presence of any metal particles.

A confirm of this, is given also in this case from EDX analysis. We found
signal coming from carbon, nitrogen and other elements in a smaller percent
(silicon coming from the substrate (SiO2 on Si) near the defects and few atomic
percent of contaminants), but no metal particles signal. For example, in different
points we collect this kind of percent:

- ✓ C = 80,56 % and N = 19,44 % ;

- ✓ C = 70,46 % and N = 29,54 % ;

UPS measurement were acquired on different areas like in the previous
sample. The sample behaviour also in this case depends on the analyzed area. We
report both UPS spectra and UPS maps in order to study as deep as possible our
sample (chemical and morphological information).

Figures 11 and 12 present the "defocalized beam" and "focalized beam" spectra, respectively, acquired on the same area. In figure 11 we notice that the structures at ~ 80 eV and ~ 83 eV shift to higher kinetic energies.

A zoom on the range 81-92 eV shows changes in the states near Fermi. Is interesting to note that when we focalize the beam on the sample (fig. 12) we have only little variations near Fermi, this means that the defocalized beam already modified the sample surface.

Maps relative to the spectra in figure 11 and 12 are show in figure 13. Dark and bright points on the map indicates differences on the sample related to morphological or chemical characteristics.
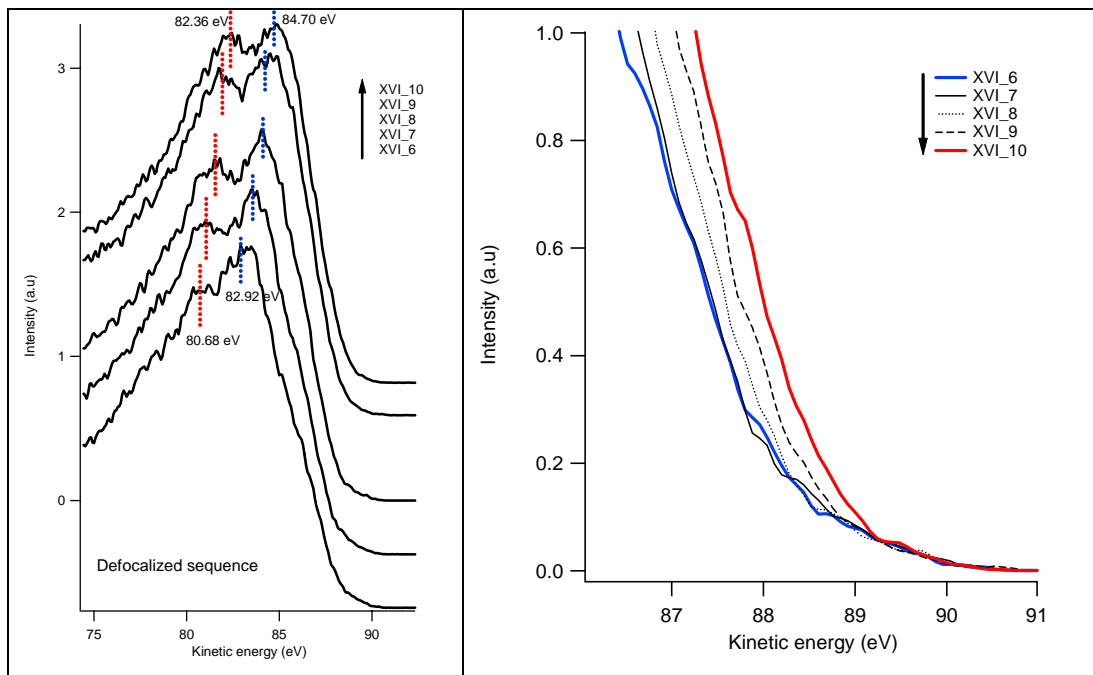
Figure 11. Defocalized sequence, the structures move to higher kinetic energy (left) (acquisition time = 90s/scan). The picture show changes at the Fermi level (range 86-91 eV) , blue and red line are respectively initial and final behaviour of the sample (right).
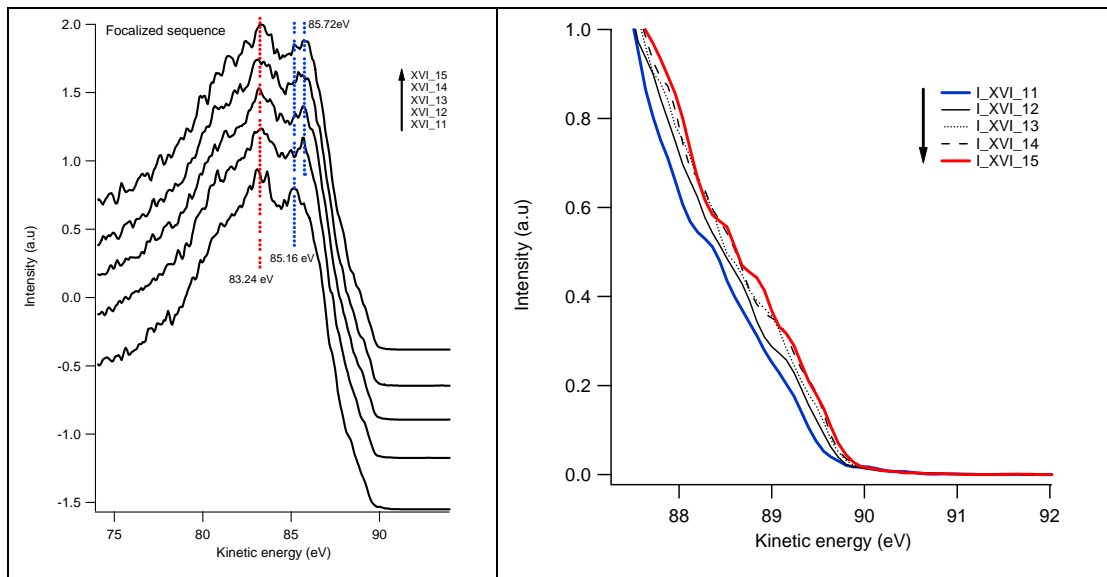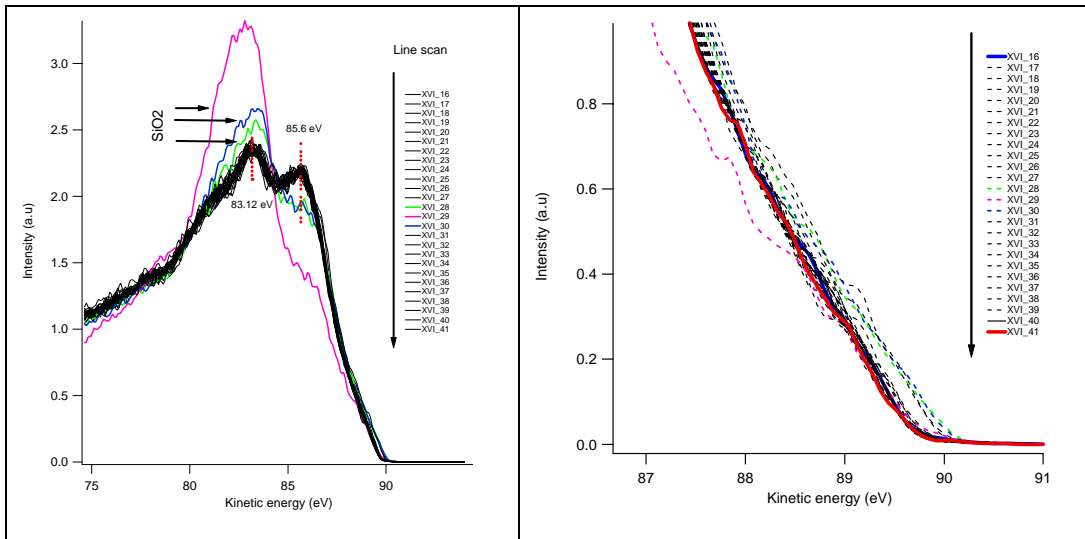
Figure 12. Focalized sequence – same area of figure 11 (left) (acquisition time = 90s/scan). Range 87-92 eV - blue and red line are respectively initial and final behaviour of the sample (right)
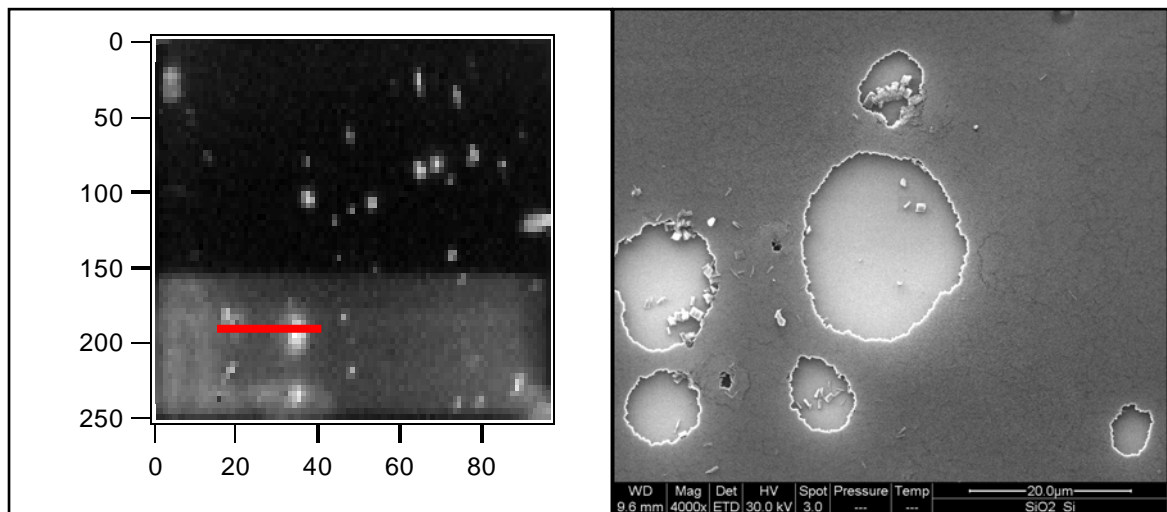

Figure 13. Map acquired on the area of figure 11 and 12 with kinetic energy = 84,1 eV. The *x* are points and *y* axis are Volts. On the right the correspondence SEM image of the area.

We acquired a *linescan* (spectra acquisition along a line) along the red line of figure 13. The result of this scan are shown below.
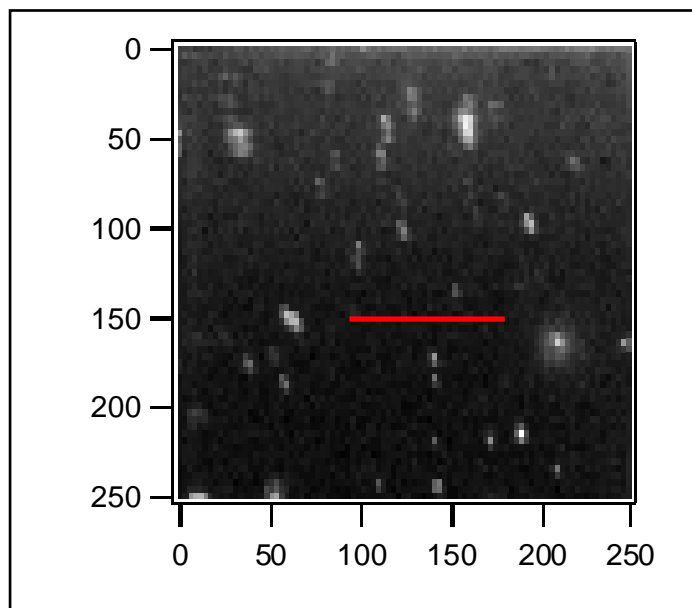
Figure 14. *Linescan* on figure 13 (along the red line) (acquisition time = 160s/scan). Charging effects on the sample (left). Range 86-91 eV - blue and red line are respectively initial and final behaviour of the sample (right).
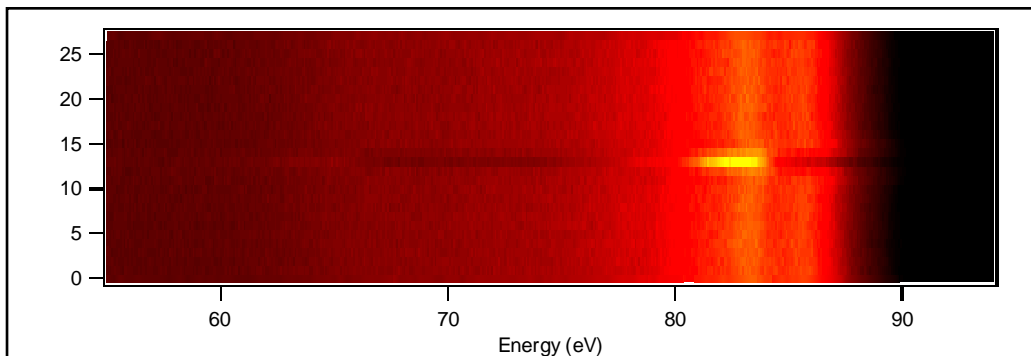
Figure 15. Intensity profile related to figure 14. A maximum is present around 83 eV

In figure 15 is shown an intensity profile for the linescan along the red line in figure 13. By comparing these results with the SEM image in figure 14, showing that the sampled area is not very uniform, we can conclude that the reasons of the observed behaviour of the UPS spectra is the sampling of Nc-C top surface where an "hole" is present. In fact, the dissimilar spectrum acquired at the centre of the line is relative to the SiO_2 surface.

In a uniform area of the sample we acquired a photoelectron map and a *linescan* with the same parameters used above.

Figure 16. Map acquired with kinetic energy = 84,1 eV.
The *x* are points and *y* axis are Volts.
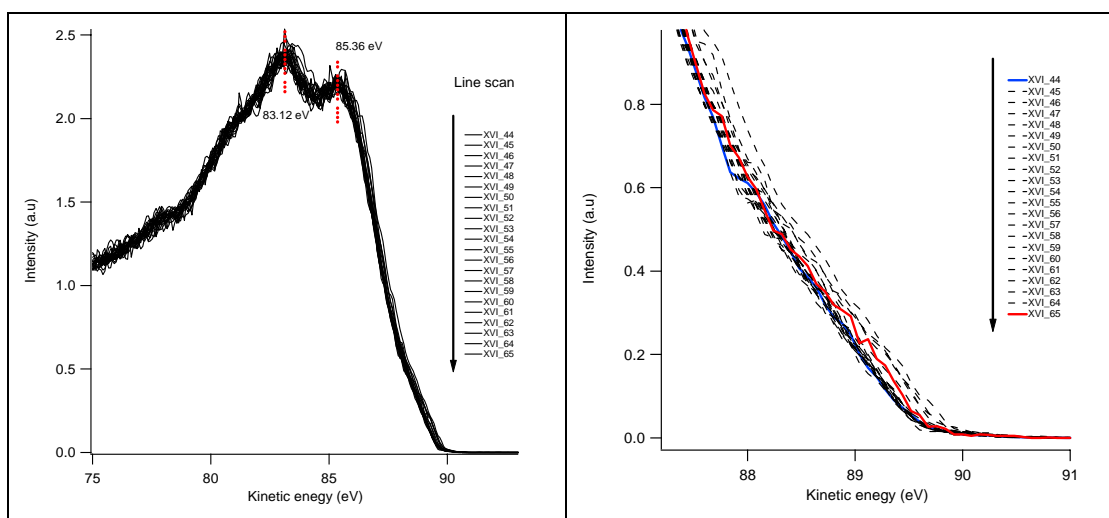
Figure 17. *Linescan* on figure 16 (along the red line) - no charging effects (left) (acquisition time = 160s/scan). Range 87-91 eV - blue and red line are respectively initial and final behaviour of the sample (right).

If we compare these spectra (see fig. 17) with the previous (see fig. 14), we can note how the sample show a uniform spectral response. For this reason we can attribute the average spectrum of figure 17 to the Nc-C topmost surface.

3.5.4 Concluding remarks

The UPS and SEM measurements on the XX and XVI samples allow us to characterize both systems. These techniques give us all the necessary information for a deep analysis of both chemical and morphological properties.

Taking into account all the results shown before, we can conclude that both samples appears to have different behaviours depending on the analyzed area.

In fact we found that they show both conductive and semi-conductive behaviour. As we explained in the previous paragraph, sometimes the conductive aspect of the sample can be related to the substrate, it means that we are looking not at the carbon nanostructures, but at the metallic elements that remained on the surface after a removal of the nanocolums (see fig. 3 and 4). SEM images display the columnar structures of the samples (see fig. 18).
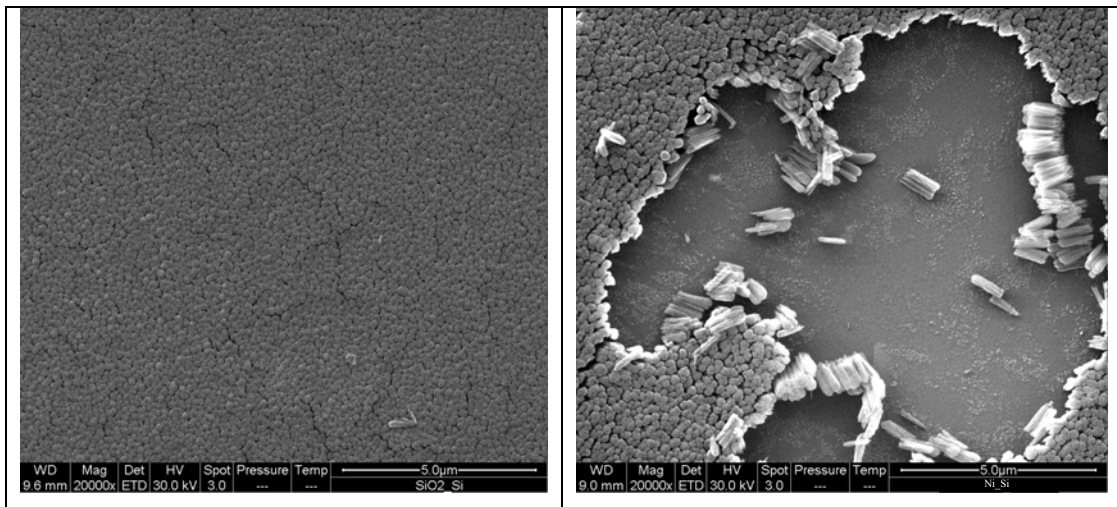
Figure 18. SEM image of samples XVI (left) and XX (right). Both samples appear with a very compact and uniform film, with nanocolumns vertically aligned on the substrate.

In conclusion, the Nc-C samples synthesized by means of RF-magnetron sputtering technique, are a new kind of aligned C based nanostructures, with a unidirectional elongation forming films with an aligned structure. We found that they grow on both Ni/Si and SiO_2 surfaces and that a considerable amount of nitrogen is incorporated during the deposition process and results contained in the nanostructures. This is due to the nitrogen gas contained in the gas mixture used

in sputtering deposition procedure. The Nc-C columns are fairly ordered and packed on the surfaces with no big differences between the two substrates (SiO2 and Ni/Si).

All these results are promising for possible applications in electronic devices of these systems remembering that similar results are obtained on both conductive and non-conductive substrates.

3.5.5 References

[1]   L. Hultman, S. Stafstrom, Z. Cziga′ ny, J. Neidhardt, N. Hellgren, I. Brunell, K. Suenaga, C. Colliex - Phys. Rev. Lett. 87 (22) (2001) 225503.

[2]   J. Neidhardt, Z. Cziga′ ny, I.F. Brunell, L. Hultman - J. Appl. Phys. 93 (5) (2003) 3002.

[3]   N. Konofaos, E.K. Evangelou, S. Logothetidis, M. Gioti - J. Appl. Phys. 91 (12) (2002) 9915.

[4]   W.T. Zheng, J.J. Li, X. Wang, X.T. Li, Z.S. Jin, B.K. Tay, C.Q. Sun - J. Appl. Phys. 94 (4) (2003) 2741.

[5]   K. P. De Jong and J. W. Geus – *Carbon Nanofibers: Catalytic Synthesis and Applications* – Catal. Rev. – Sci. Eng. **42** (4), 481-510 (**2000**)

[6]   P. M. Ajayan – *How does a nanofiber grow ?* – Nanotechnology (**2004**)

[7]   S. Scalese, V. Scuderi, F. Simone, A. Pennini, G. Compagnini, C. Bongiorno, V. Privitera – *Carbon aligned nanocolumns by RF-Magnetron sputtering: the influence of the growth parameters* – Physica E, **37** (2007) 231-235

[8]   S. Scalese, V. Scuderi, F. Simone, A. Pennini, G. Compagnini, V. Privitera – *Growth of aligned CN_x nanocolumns on silicon by RF-magnetron sputtering* – Letters to the Editor, Carbon **44** (2006) 3113-3148

4. Conclusions

Our work was performed, as specified at the beginning, in order to characterize and compare different kind of carbon-based nanometric systems. We used different techniques in order to wholly analyze our samples properties. For a chemical and morphological investigation, we use SEM (scanning electron microscopy), TEM (transmission electron microscopy), AES (auger electron spectroscopy), STM/STS (scanning tunneling microscopy/spectroscopy) and UPS (ultraviolet photoemission spectroscopy), while for the probe of electronic and structural properties we used EELS (electron energy loss spectroscopy) and Raman spectroscopy.

The analyzed structures were produced with different procedures or with the same procedure but in different conditions. In this way we could compare their main features as morphology, electronic behavior and chemical composition. In the following, we resume the main findings for each system and a general note on the entire work reported.

SWCNTs by CCVD

In this section we investigated the influence of several parameters of the growth process on the structural and electronic features of the produced carbon nanotubes. In fact, we found that, even though the carbon is the major constituent (over 70 %) of the produced material, the remaining particles have structures and compositions which change in dependence of the catalysts type (Fe, Co etc.) and percentage (2 % wt and 5% wt), on the growth time (30 and 60 minutes) and on reaction temperature (700 and 800 °C).

With respect to these parameters, we found that using Fe1% Co1% catalyst particles at 800 °C for 30 minutes we obtain the optimal SWCNTs growth. At the same time, using Fe5%-Co5% catalyst particles at 700°C for 30 minutes the produced CNT present more walls and the material shows the presence of an higher quantity of amorphous carbon. In any case, these two parameters sets give rise to a quite pure CNT samples if compared with other growth conditions. In fact, using Fe1% Co1% catalyst content at 800°C fro a longer time (60 minutes), we detected the presence of an higher quantity of

amorphous carbon while with a Fe5% Co5% particles, at 800°C for short time (30 minutes), we have the presence of a great amount of amorphous nanometric aggregates.

⬥ *Functionalized CNTs (f-CNTs)*

The analyzed systems are CNTs with different functionalization.

Laponite/CNT/N/4 : SWCNT are intercalated into the interlayer space of an synthetic clay (Laponite, chemical formula: $(Si_8)^{IV} (Mg_{5.48}Li_{0.52})^{VI} O_{20} (OH)_4 Na_{0.52})$.

DO3/39 samples: CNTs functionalized with pyridine and metal particles (DO3/39/5 SWCNT/Pyridine/Fe3Oy, DO3/39/7 SWCNT/Pyridine/CoPt and DO3/39/8 SWCNT/Pyridine/Co).

As expected, these samples show different behaviors depending on the metal particles embedded inside them. By matching all results obtained by SEM and UPS analysis, we found that DO3/39/8 and DO3/39/5 have a semiconductive behavior while DO3/39/7 is metallic and Laponite/CNT/N/4 has an insulating characteristic.

⬥ *Sn@CNTs – Filled carbon nanotubes*

The insertion of soft metals like Sn inside the CNTs gives pronounced curvature changes and consequently induces changes in the electronic properties of the sample close to the Fermi Level. The encapsulation of the metals in the inner cavity of CNTs can bend easily the nanotube structure and thus tune their electronic properties. This is an important finding that could expand the potential application of CNTs for the development of novel electronic devices.

⬥ *Nc-C (Carbon Nanocolumns)*

The Nc-C samples synthesized by means of RF-magnetron sputtering technique, are a new kind of aligned C based nanostructures, with a unidirectional elongation forming films with an aligned structure. We found that they grow on both Ni/Si and SiO2 surfaces and that a considerable amount of nitrogen is incorporated during the deposition process and results contained in the nanostructures. This is due to the

nitrogen gas contained in the gas mixture used in sputtering deposition procedure. The Nc-C columns are fairly ordered and packed on the surfaces with no big differences between the two substrates (SiO2 and Ni/Si).

All these results are promising for possible applications in electronic devices of these systems remembering that similar results are obtained on both conductive and non-conductive substrates.

CNTs by SiC (Silicon Carbide)

This way of producing CNTs seems to be very interesting and also very useful, because catalyst particles are not required. As we saw in the SEM and STM images, CNTs grown by SiC surface decomposition are very packaged on the surface. The Raman and STM analysis indicate a small number of the carbon walls. In addition the EEL spectra show the good quality of the sample. The Auger and EDX spectra confirm this quality from the absence of oxygen signal or other contaminant particles. The investigated samples show a diode-like behaviour depending on the sample bias and in particular it shows electron collector behaviour.

Finally, we can conclude that both CNTs growth procedure are interesting and useful. The CCVD required metal particles as catalyst and depending on them we could reach different results. From this point of view, we have a further growth parameter that we can set together with temperature and time, in order to produce pure SWCNT with a simple and efficient process. On the other hand, the necessity of catalyst particles could be considered as a limitation of the growth process.

In this perspective, the second procedure that we analyzed, the CNTs production by SiC surface decomposition, is more promising because it requires only a proper thermal treatment of the 6H-SiC substrate. Furthermore, this method allows to produce CNTs without eventual problems related to the presence of other particles embedded in our samples and does not need any further purification procedure.

A final and important characteristic is that the CNT films on SiC substrates are very packed and regular showing a dense structure made of aligned CNT physically attached to the SiC substrate.

The resulting features of the samples produced by use of both techniques make them useful for different applications, i.e., for example, they can be used in photovoltaic applications as an electron collector in solar cell or for the development new photonic systems. Other potential applications of CNTs are the development of novel electronic devices, as diodes or transistors, field emitters, data storage devices or the production of hydrogen storage materials. Finally, they could be used also for reinforcement in composite materials.

All these possible applications exploiting their exceptional properties, make them the objective of many experimental and theoretical works, developed worldwide, with the hope of finding their optimal applications to improve our life.

5. *References*

[1] *Nanotechnology* (Ed.: G. L. Tinp), Springer-Verlag, New York, **1998**

[2] A. N. Goldstein - *Handobook of Nanophase Materials*, Marcel Dekker, Inc., New York, **1997**

[3] L. Dai, A. Patil, X. Gong, Z. Guo, L. Liu, Y. Liu, and D. Zhu – *Aligned Nanotubes* – ChemPhysChem **4**, 1150 (**2003**)

[4] A. V. Melechko, V. I. Merkulov, T. E. McKnight, M. A. Guillorn, K. L. Klein, D. H. Lowndes, M. L. Simpson – *Vertically aligned carbon nanofibers and releated structures: controlled synthesis and directly assembly* – J. Appl. Phys. **97**, 041301 (**2005**)

[5] A.Vaseashta, J. Irudayaraj – *Nanostructured and nanoscale devices and sensors* – J. Optoelect. and Adv. Mat. **7**, 35-42 (**2005**)

[6] R. V. Ramanujan – *Nanostructured electronic and magnetic materials* - Sadhana **28**, 81-96 (**2003**)

[7] C. Verìssimo, S. A. Moshklyov, A. C. S. Ramos, J. L. Gonçalves, O. L. Alves and J. W. Swart – *Different Carbon Nanostructured Materials Obtained in Catalytic Chemical Vapour Deposition* – J. Braz. Chem. Soc. **17**, 1124-1132 (**2006**)

[8] L. Delzeit, C. V. Nguyen, B. Chen, R. Stevens, A. Cassell, J. Han, and M. Meyyappan – *Multiwalled Carbon Nanotubes by Chemical Vapour Deposition Using Multilayered Metal Catalysts* – J. Phys. Chem. B **2002**, **106**, 5629-5635

[9] L. I. Johansson, F. Qwman, P. Martensson, C. Persson, and U. Lindefelt – *Electronic structure of 6H-SiC(0001)* – Phys. Rev. B **53**, 20 (**1996**)

[10] J. T. Wolan, B. A. Grayson, G. Akshoy, S. E. Saddow – *Characterization of single-crystal SiC polytypes using X-ray and Auger photoelectron spectroscopy* – Appl. Surf. Sci. **184** (**2001**) 167-172

[11] G. M. Odegard, S. J. V. Frankland and T. S. Gates – *Effect of Nanotube Functionalization on the Elastic Properties of Polyethylene Nanotube Composites* – AIAA Journal, **43**, 8 (**2005**)

[12] H. X. Wu, R. Tong, X. Q. Qiu, H. F. Yang, Y. H. Lin, R. F. Cai and S. X. Qian – *Functionalization of multiwalled carbon nanotubes with polystyrene under atom transfer radical polymerization conditions* – Carbon **45** (**2007**) 152-159

[13] X. Liu, T. Pichler, M. Knupfer, and J. Fink – *Electronic and optical properties of alkali-meta-intercalated single-wall carbon nanotubes* – Phys. Rev. B **67**, 125403 (**2003**)

[14] L. Duclaux – *Review of the doping of carbon nanotubes (multiwalled and single-walled)* – Carbon **40** (**2002**) 1751-1764

[15] S. Suzuki, C. Bower, O. Zhou – *In-situ TEM and EELS studies of alkali-metal intercalation with single-walled carbon nanotubes* – Chem. Phys. Lett. **285** (**1998**) 230-234

[16] M. Monthioux – Filling *single-wall carbon nanotubes* – Carbon **40** (**2002**) 1809-1823

[17] H. Lùth – *Surfaces and interfaces of solid materials* – Springer Study Edition 1998

[18] M. De Crescenzi, M.N. Piancastelli – *Electron scattering and related spectroscopies* – World Scientific, publishing (1996)

[19] John T. Yates, Jr and Theodore E. Madey – *Vibrational spectroscopy of molecules on surfaces* – Plenum Press, New York and London 1987

[20] R.F. Egerton – *Application of electron energy-loss spectroscopy to the study of solid catalysts* – Topic in catalysis **21**, 4 December (2002)

[21] G. Ertl, J. Kuppers –*Low energy electrons and surface chemistry* –VCH 1985

[22] Joseph I. Goldstein, Harvey Yakowitz – *Practical scanning electron microscopy, Electron and Ion Microprobe Analysis* – Plenum Press, New York and London 1975

[23] Stroscio, A. J.; Kaiser, W. J. *Scanning Tunneling Microscopy*; Academic Press: San Diego, 1993.

[24] Hansma, P. K.; Tersoff, J. *Journal of Applied Physics* **1987**, *61*, r1.

[25] D.P. Woodruff and T.A. Delchar - *Modern Techniques of Surface Science, chap. 3* - Cambridge University Press, Cambridge (1994).

[26] M. Pruttom ed.: Electronic Properties of Surface, chap. 2, Adam Hilger, 1984

[27] B.P. Straughan and S. Walker ed.- *Spectroscopy*,chap. 7 - Chapman and Hall, (1976)

[28] B. Schrader, Chapter 4 in "*Infrared and Raman Spectroscopy*", B. Schrader ed., VCH Publishers Inc.: New York, (1995)

[29] M.D. Morris, Chapter 6 in "*Applied Laser Spectroscopy*", D.L. Andrews ed., VCH Publishers Inc.: New York, (1992).

6. Appendix

6.1   Thin-film Pt-Ru alloys

6.1.1 Introduction

Fundamental understanding of the effect of composition and architecture of a core-shell type catalyst on its electronic structure is critical in understanding and predicting the activity of its surface to adsorbates. The lengthscales over which the core of a catalyst has an influence over the electronic structure of the shell (surface) will provide predictive power in designing better core-shell catalysts, since the chemistry of catalysts is governed by not only the surface but also, indirectly, by the sub-surface.   However, very little is known about the shell (top 2-3 layers), sub-surface (3rd – 10th layer) and bulk composition, or the surface morphology, in binary alloys that are created through thermal interdiffusion.

We have conducted a systematic study of the canonical Pt-Ru catalyst system in thin-film form in order to determine the effects of alloying through interdiffusion between alternating layers (~20 Å each) of Pt and Ru, we also studied the interactions of this system with carbon monoxide (CO). XRD and EXAFS (at beamline X23A2 of the National Synchrotron Light Source at Brookhaven National Laboratory) confirmed the alloying between Pt and Ru. Using environmental SEM and AFM measurements, we find a surface roughening through terrace formation that increases the effective surface area. Microprobe UPS (at the Elettra synchrotron in Trieste) was used to establish the compositional uniformity across the terraces. We also find a Ru enrichment of the shell (65% Ru versus 50% Ru in the bulk) and a Ru depletion of the sub-surface (35% Ru with respect 50% in the bulk) upon formation of the Pt-Ru alloying. The catalyst chemistry of Pt-Ru alloys are, therefore, governed by a shell enriched by Ru and indirectly by a Ru depleted sub-surface.

6.1.2 Experimental

6.1.2.1 Sample Preparation

A compositional array of Pt-Ru alloys were prepared by dual-target sputter deposition of Pt and Ru in unique rectangular pads on Si (with a SiO_2 buffer layer).   On each pad in the array, Pt and Ru were deposited in alternating layers (each ~20 Å) with the pattern of heterostructure designed to produce the desired alloy composition after annealing (each strip containing three metal film on a SiO2/Si – see figure 2).   The unannealed, multi-compositional Pt-Ru array was cleaned by light Ar sputtering at a shallow angle prior to annealing at ~850 °C in order to form Pt-Ru alloys, under vacuum (fig. 1).   The nominal, or bulk, compositions of the alloys were, Pt, $Pt_{75}Ru_{25}$, and $Pt_{50}Ru_{50}$ as determined by the sputtering conditions.
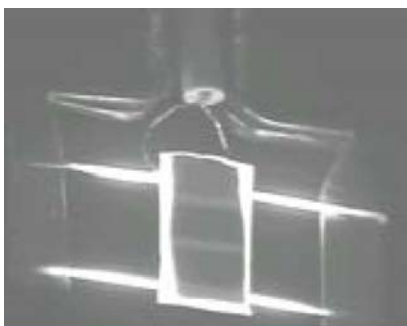

Figure 1. A sample array is being heated in-situ in a home-built sample holder.   This glowing image was captured at ~ 850°C sample temperature.

Strips are prepared in identical conditions and consist on a pure Pt film (Pt100 sample from here on), a 75%Pt/25%Ru (Pt75Ru25 sample from here on) and 50%Pt/50%Ru (Pt50Ru50 sample from here on). Pure Pt layer is about 150Å thick (56s deposition), Pt50Ru50 has a total height of 280Å (Note 50/50 by at% not vol% - 15Å of Ru on the bottom, then 20Å of Pt, then 15Å of Ru and so on till there was 8 layers of Ru and 8 layers of Pt) and Pt75Ru25 has a total thickness of 360Å (8 bilayers of Ru 10Å thick intermixed with 8 bilayers of Pt 35Å thick - the

first layer was Ru and the last capping layer was Pt). One strip was annealed at ca. 1150 K for 15 minutes, sputter cleaned and subjected to partial electron yield (PEY) spectroscopy with sample-charge compensation and CO dosing.
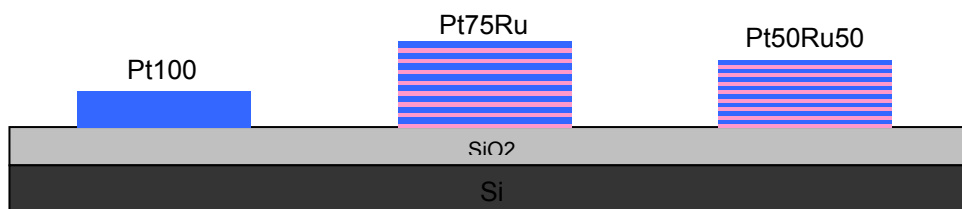
Figure 2. Schematic representation of our samples
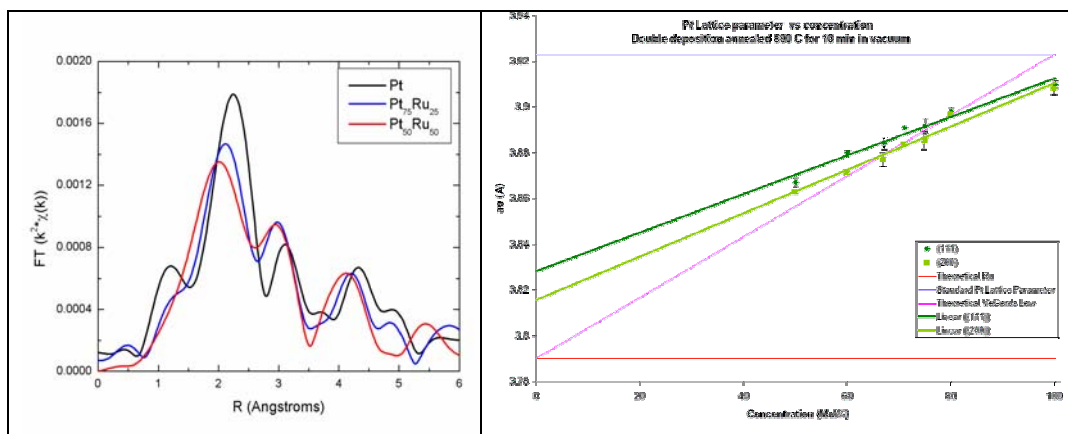
Figure 3. Analysis done at the Pt L edge. Comparison of the Pt, Pt75Ru25, and Pt50Ru50 sample. Fourier transformation shows nearest neighbor distances decrease as Ru is forming a solid solution with fcc Pt.

6.1.2.2 Temperature Programmed Desorption (TPD)

Carbon monoxide was exposed to the sample array under the conditions described in the NEXAFS section below. The beamline monochromator was moved to 288.6 eV (where significant $2\pi^*$ intensity is observed on all the alloy compositions). The array was then heated at a constant rate of 0.5 K/s, while the PEY counts from CO on a sample were collected, from 150 K to 550 K. The experiment was then repeated for each sample on the array.

6.1.3 Results and discussion

### 6.1.3.1 SEM characterization

As deposited samples

The surface structure of the 'as deposited' films is very similar. The metal surface appears quite structure less on the micrometric scale and faint features can be revealed only at very high magnifications. Those weak features emerge as a granular structure with a typical grain size of less than 90 nm.

The estimate of these lengths is carried out by using the autocorrelation function of the morphological data gathered in the surface sample SEM images: in all the three cases the function is close to zero for correlation lags above 200 nm while they show a clear negative minimum for lags close to 40-45 nm (smoother and larger structures are found for the Pt50Ru50 sample).

The data used for the computation of the autocorrelation function are extracted as linear profiles from the SEM digital images and generally consist of the intensity profile over a surface coordinate range as large as 15 times the shown window width. Where it was necessary, a background procedure is adopted in order to enhance the fast varying component.
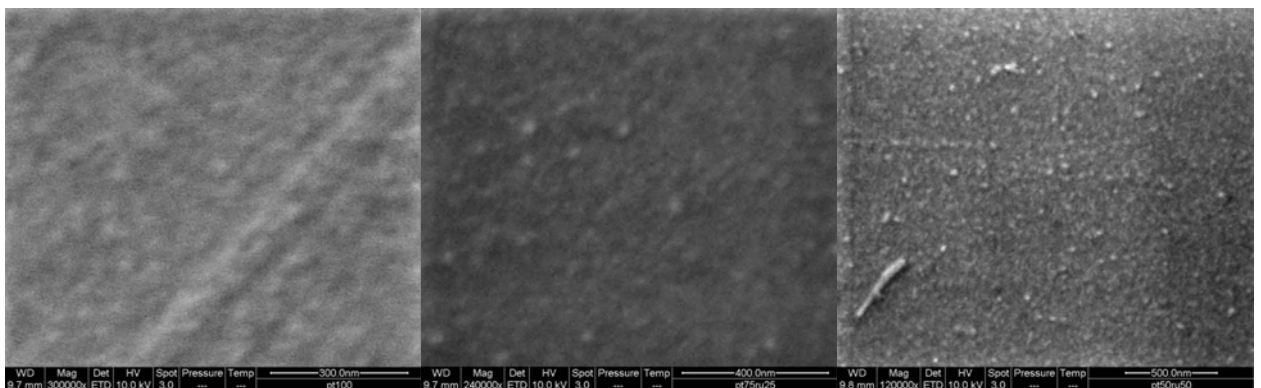

Figure 4. SEM images of the 'as deposited' PtRu/SiO2/Si samples: (from the left) Pt100, Pt75Ru25 and Pt50Ru50.
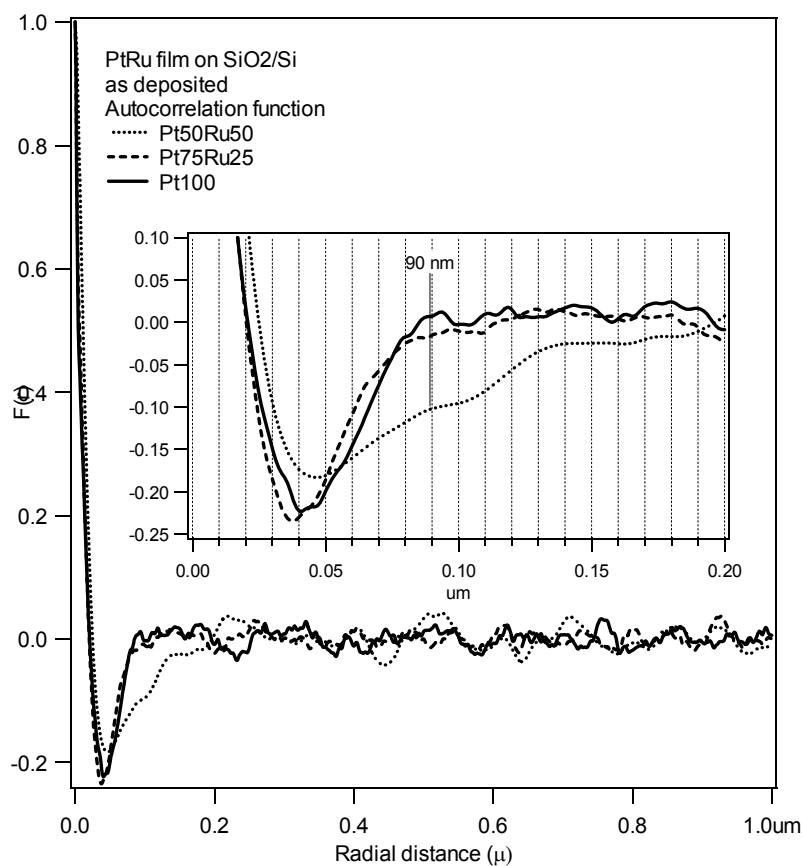
Figure 5. Autocorrelation function for the structures present on the SEM images of the metallic film surfaces.

The elemental analysis of the films was performed by acquiring the EDX spectra using a 10 keV electron beam probe. The choice of this relatively high electron energy is due to the aim of exciting the Pt M and Ru L fluorescence lines trying to minimize the effects of the electron penetration below the sample surface. Nevertheless, the Si and O signal originating from the substrate are always present in the emission spectra.

Figure 6 shows the spectra of the 'as deposited' films after they were normalized to the Pt peak intensity. The Pt/Ru calculated content ratios agree with those estimated during the deposition (see table 1). The apparent lower content of Ru in the Pt50Ru50 sample (-14%) is due to the shadowing of the hidden Ru layers by the overlaying Pt ones.
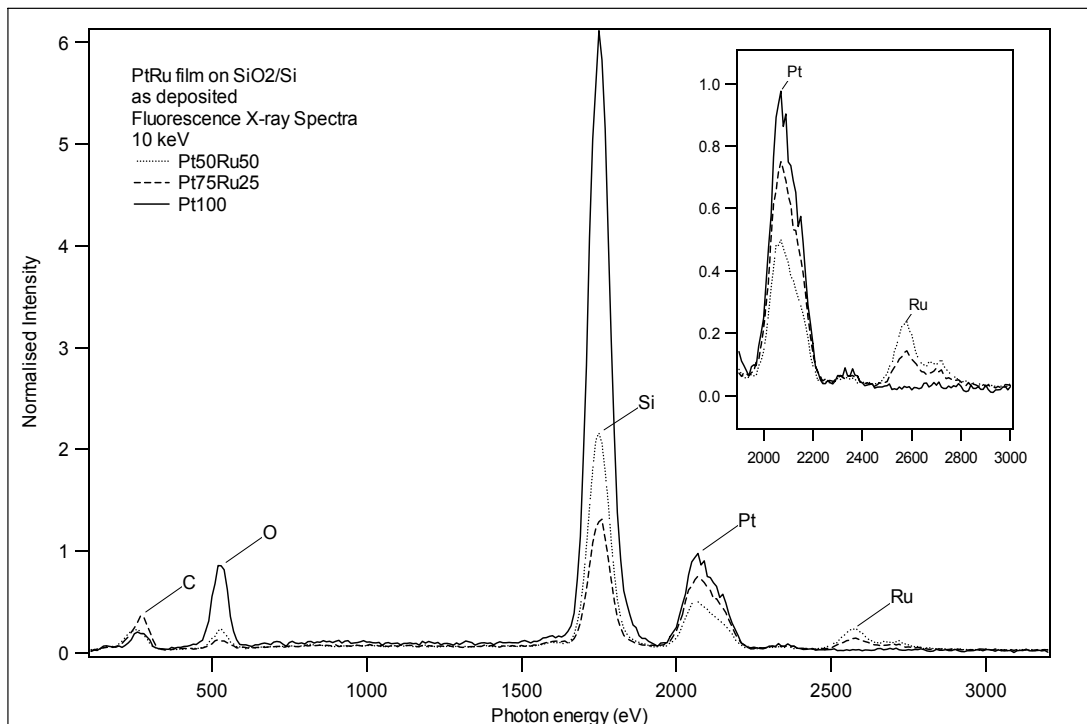
Figure 6. Normalized EDX spectra from the 'as deposited' films: note the high Si signal of the
Pt100 sample. The inset shows the region containing the Pt M and Ru L emission lines.

The Si signal, on the other hand, shows the expected behavior: Si fluorescence is
more evident in the Pt100 sample and less in the Pt75Ru25 one due to the higher
stopping power of Pt atoms.

The C fluorescence intensity and the O/Si signal ratio values show an anomalous
behavior for the Pt100 sample: the C content is much lower for this sample and
the O/Si ratio is much higher compared to the other samples. This can not be
ascribed to the effects of the surface catalytic action because, in principle, they are
strictly the same. Furthermore, from the deposition process on, their exposure to
atmospheric conditions was the same. Thus, the difference has to be related with
the cross-contamination of the surface during the growth processes.

.

Ex-situ annealed samples

The 1150 K annealing process strongly influences the morphology of the metallic
film surface. As a simpler case, we start discussing about the pure Pt film in

which we already find some interesting features. The following figure shows how the surface acquired a higher contrast due to the coalescence of the Pt atoms and the formation of aggregates with 130 nm typical size as can be deduced from both the SEM images at high magnification and the autocorrelation function. The granular structure of the surface is homogeneous over very large areas.

Sample	File	C K	O K	Si K	Pt M	Ru L	Ru/Pt	O/Si	Met/Si	Note	IMG
Pt 100 (880)	Pt100_001	6.9	25.9	64.9	2.3	0.0	0%	40%	4%	large area	Pt100_005
Pt 100 (RT)	Pt100_001	17.3	18.0	58.9	5.9	0.0	0%	31%	10%	large area	Pt100_004
Pt 50 (880)	Pt50_001	21.3	17.5	52.6	4.3	4.3	100%	33%	16%	large area	Pt50_005
Pt 50 (880)	Pt50_004	21.5	17.3	52.9	4.6	3.6	78%	33%	16%	dark particle	Pt50_008
Pt 50 (880)	Pt50_003	21.4	18.4	51.2	4.9	4.2	86%	36%	18%	bright particle	Pt50_008
Pt 50 (RT)	Pt50ru50	30.0	10.3	47.6	6.6	5.6	84%	22%	25%	large area	pt50_002
Pt 75 (880)	Pt75_001	22.4	15.3	50.3	9.1	3.0	33%	30%	24%	large area	Pt75_006
Pt 75 (880)	pt75_002	55.1	6.4	30.0	6.6	2.0	30%	21%	29%	dark particle	Pt75_008
Pt 75 (880)	Pt75_003	54.3	6.6	30.3	6.8	2.1	31%	22%	29%	bright particle	Pt75_009
Pt 75 (RT)	Pt75ru75	53.0	5.1	29.1	9.7	3.1	32%	18%	44%	large area	Pt75_001

Table 1. Elemental composition calculated from the EDX spectra acquired using a 10 keV electron beam

The annealing process of the Pt100 sample affects its fluorescence spectrum, too. The amount of Pt on the surface, calculated after the Pt M fluorescence intensity, is strongly reduced. Provided that the hypothesis of a thin and uniform film is deposited, this apparent reduction can be attributed to the uncovering of the SiO_2 surface due to the formation of the Pt aggregates. A suppression of the C signal is also observed.
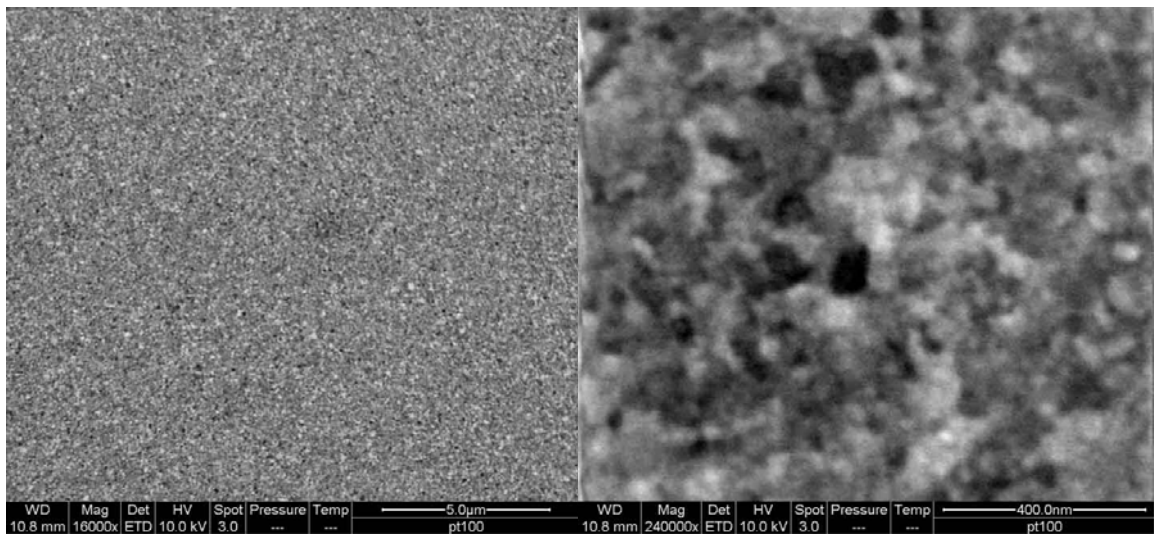
Figure 7. Pt100 surface after the annealing (1150 K) process.
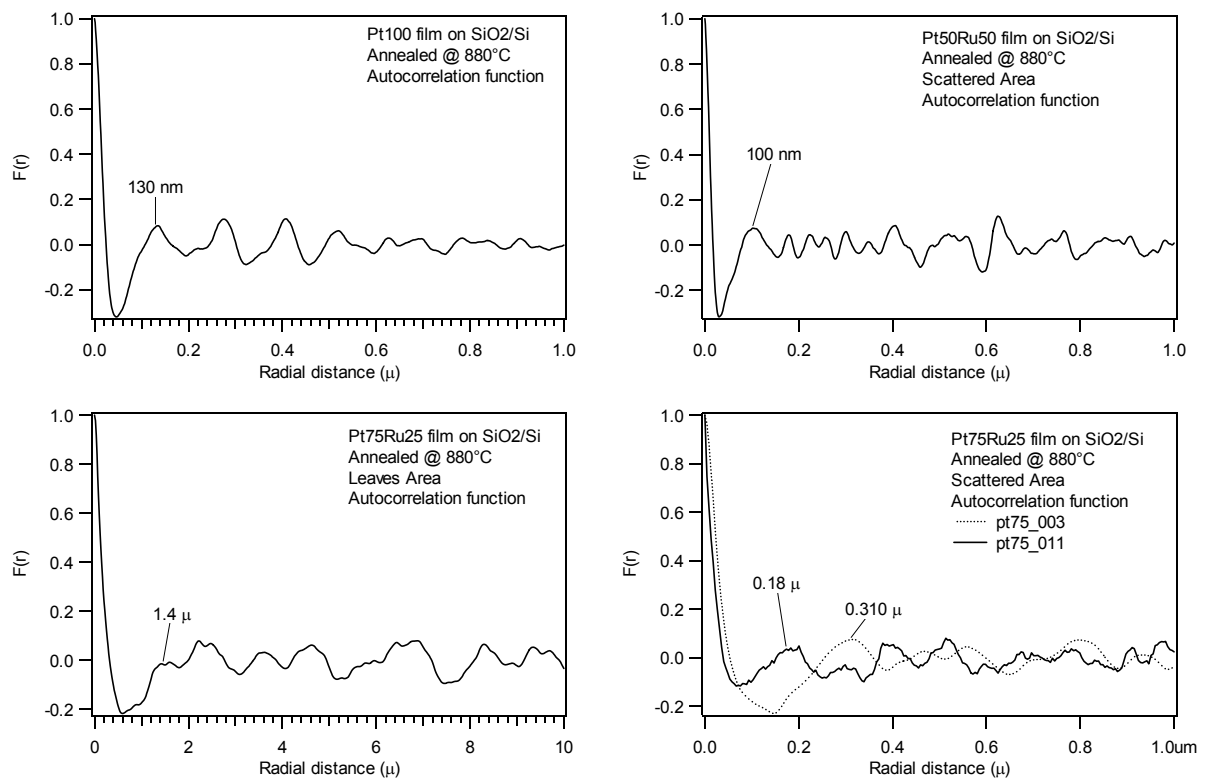
Figure 8. Autocorrelation function for the structures present on the SEM images of the metallic

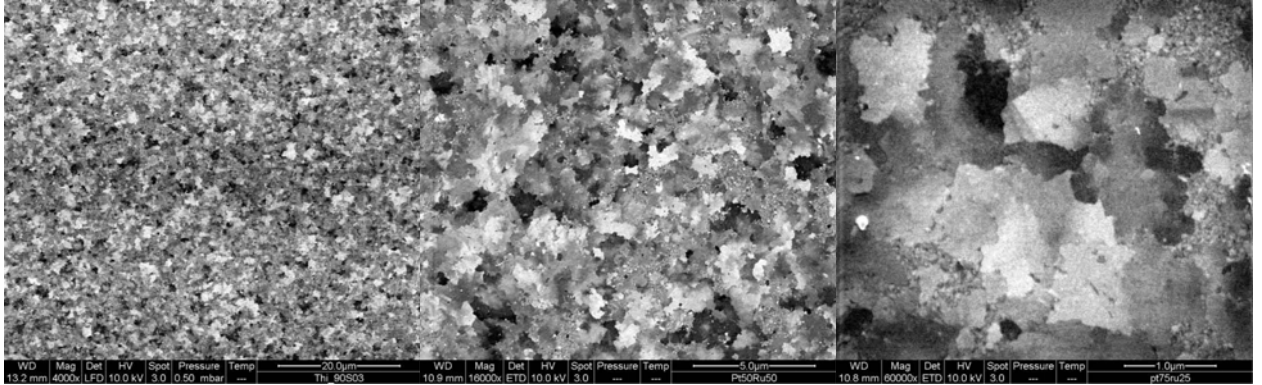film surfaces after the annealing procedure at 1150 K.

.
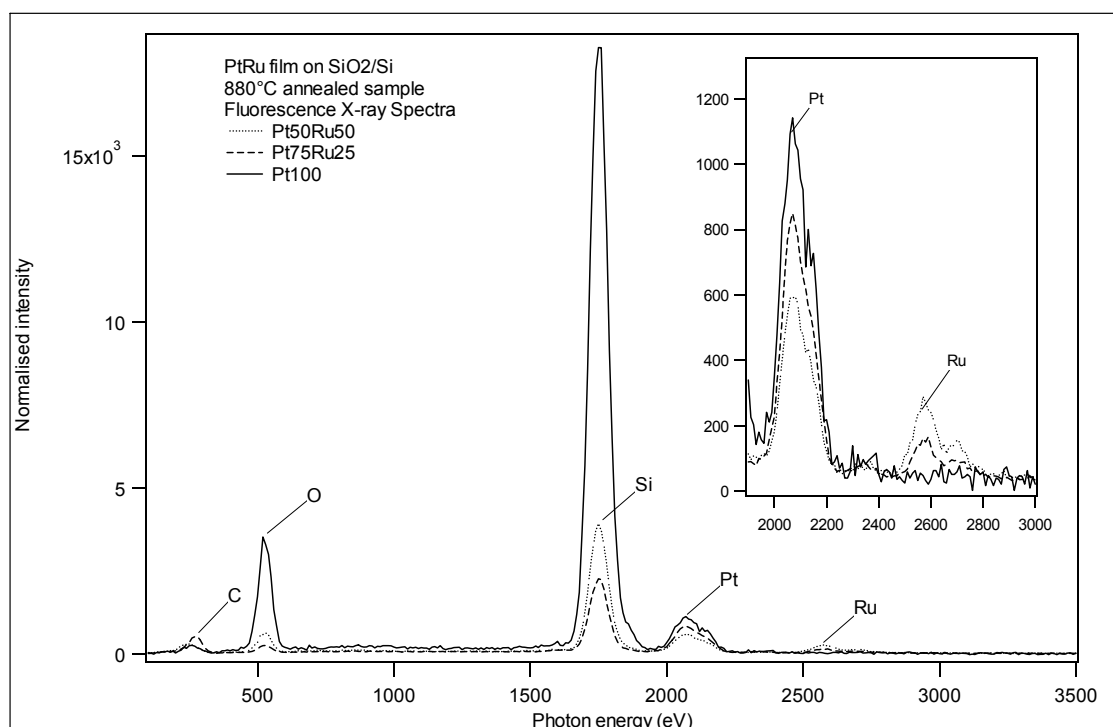
Figure 9. EDX spectra from the annealed films. The inset shows the region containing the Pt M and Ru L emission lines

The surface structure of the Ru-containing film is drastically changed by the 1150 K annealing procedure, too. We detect both the formation of large areas with granular structure and the formation of few-micron-wide islands. The granular structure is very similar to that observed on the Ru-free sample with a typical dimension of the aggregates ranging from 100 nm for Pt50Ru50 sample to 180 nm for the Pt75Ru25.

Comparing the large area EDX analysis on sample with the same composition before and after the annealing process (see table 1), we can note that the metal/Si ratio decreases of about 30-35% upon annealing. In accord with the previous interpretation of this fact, we have that the formation of the surface structures uncovers the SiO2 substrate even though to a minor extent.

The new features have a leaf shape and a typical dimension 1.4 micron, i.e. 10 times larger then the aggregates present in the granular areas. Keeping in mind that the film thickness prior to the annealing procedure is 200 Å, these structures are very flat having a very low height to lateral dimension ratio. Their surface is quite structureless and they show different intensity in secondary electron (SE)
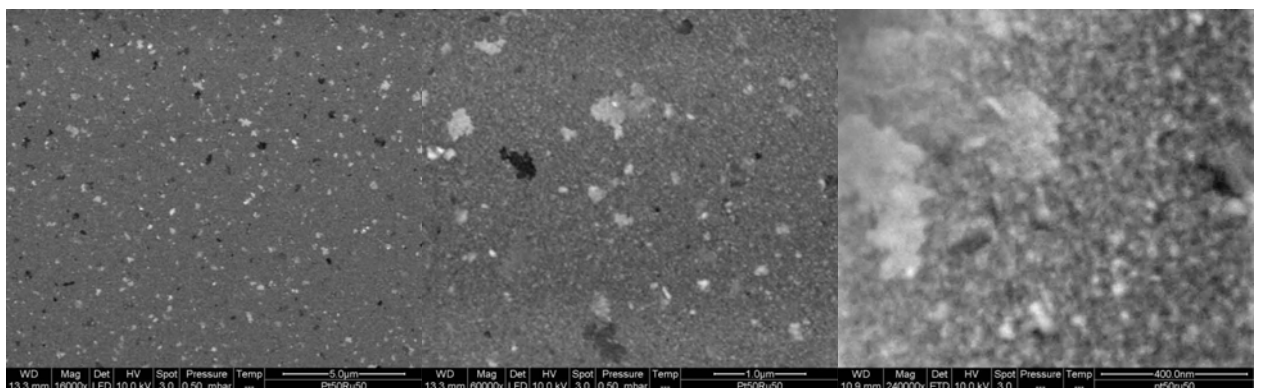
emission (see the difference in grayscale) probably because of dissimilar state of the surface oxidation.

Figure 10. Pt50Ru50 surface after the annealing (1150 K) process.

$Pt_{50}Ru_{50}$ 1150K-annealed film
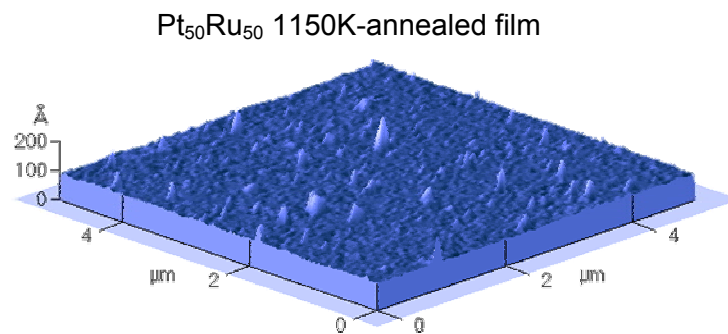
Figure 11. AFM (atomic force microscopy) surface plot.

Figure 12. Pt75Ru25 surface after the annealing (1150 K) process.

The percentage of the metallic film surface covered by those islands vary with the Ru content: they cover the 50-60% of the Pt75Ru25 sample surface being often contiguous while they are isolated on the Pt50Ru50 surface covering only the 10% of it. In order to clarify the nature of these structures, we performed a position resolved EDX analysis trying to identify possible chemical differences. The probed region, with a primary electron beam of 10 keV, is 1 micron wide and the data carry averaged information on areas whose dimension are compatible with that of the islands. The results of these investigations are shown in table 1 where it is possible to note that the Ru/Pt ratio does not meaningfully vary over islands with different SE intensity. The fluorescence data are not varying if we compare them with the large area acquisition, too. A further investigation on the chemical anisotropies is carried out by means of a line profile of the fluorescence intensities on a Pt75Ru25 sample surface. In spite to a strong anisotropy of the SE intensity, there are not meaningful variation of the Pt and Ru signals.

These results indicate that the formation of the islands do not follow a phase separation neither a differentiation due to an enrichment of one of the alloying elements. The analysis, being averaged on the whole film thickness, could not exclude that the shown effects are a simple rearrangement of the topmost metallic layers.

In-situ annealing of the Pt75Ru25 sample

By exploiting an in-situ heating stage of our SEM apparatus, we were able to anneal in situ an 'as deposited' Pt75Ru25 sample up to 1220 K. The use of the heating stage for temperature close to 1300 K requires to operate in low vacuum conditions with a residual pressure in the mbar range. Thus, the annealing was performed at a pressure of 0.3 mbar using water as residual gas (water is the standard gas). In this operating mode it is not possible the acquisition of the EDX spectra while the SE are acquired using the GSED detector which collect with relative low efficiency those emitted in the normal direction respect to the sample surface.

The heating process consisted of a step-like increase of the sample temperature in which it was kept constant for ca. 4 minutes at each value. The heating sequence is depicted in figure 14.
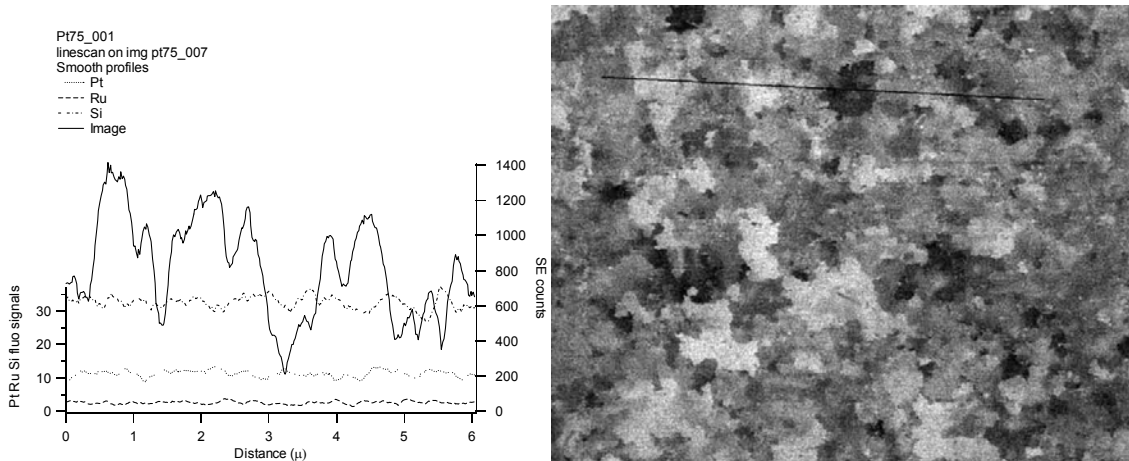

Figure 13. Line profile of the intensities on a Pt75Ru25 samples (see text).

The SEM images acquired up to 920 K did not show any difference with respect to the pristine sample. The surface is smooth and a faint granular structure is perceptible at very high magnifications. Some dark areas, few tens micron wide, are present on the surface with similar granular structure and are probably due to defects at the film/substrate interface.

Reaching 970 K a few tens dark and bright islands appear on a 500 micron x 400 micron surface area. Their size is lower than 2 micron and, all together, they occupy the 3% of the surface.

The new features have no relation with the previous dark areas which, in turn, shrink. No morphology-related pinning effect is found for the nucleation of the islands.

At 1020 K, hundreds of islands emerge with a uniform distribution on the surface and a prevalence of dark islands on the bright ones. The islands appeared at 970 K grow in lateral size reaching a mean dimension above 2 micron. The percentage of the surface area covered with these structures is 11%. At this temperature, no trace of the large dark areas remains in the investigated area. Increasing the temperature at 1070 K, the islands grow a bit more in size causing an increase of the covered area to 14%. The islands SE intensity is equally distributed between bright and dark ones. Some very bright spots with <200 nm size appear on the surface. At 1110 K and 1150 K, no differences appear on the surface. Increasing the temperature to 1220 K, the surface becomes rougher, the 'bright' islands coalesce forming larger ones with fuzzier contours while the darker ones partially disappear. New black spots with lateral size ≤1 micron develop all over the mapped area.

Pt75Ru25 annealing process
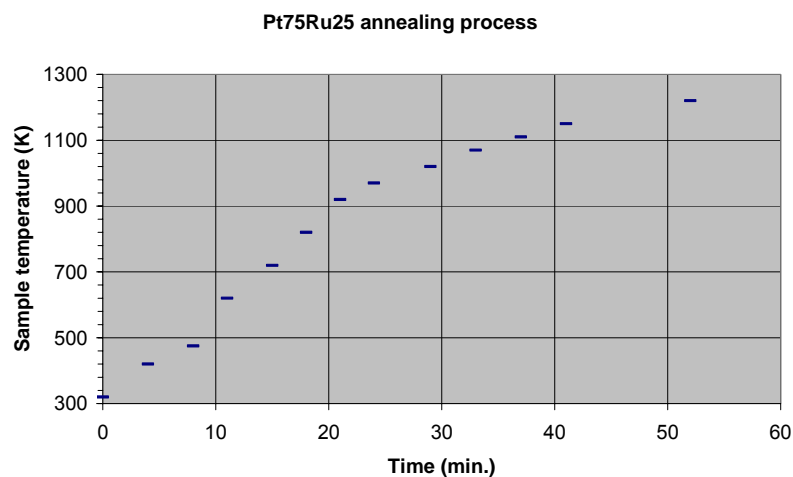
**Figure 14.** Time sequence of the Annealing Temperature.
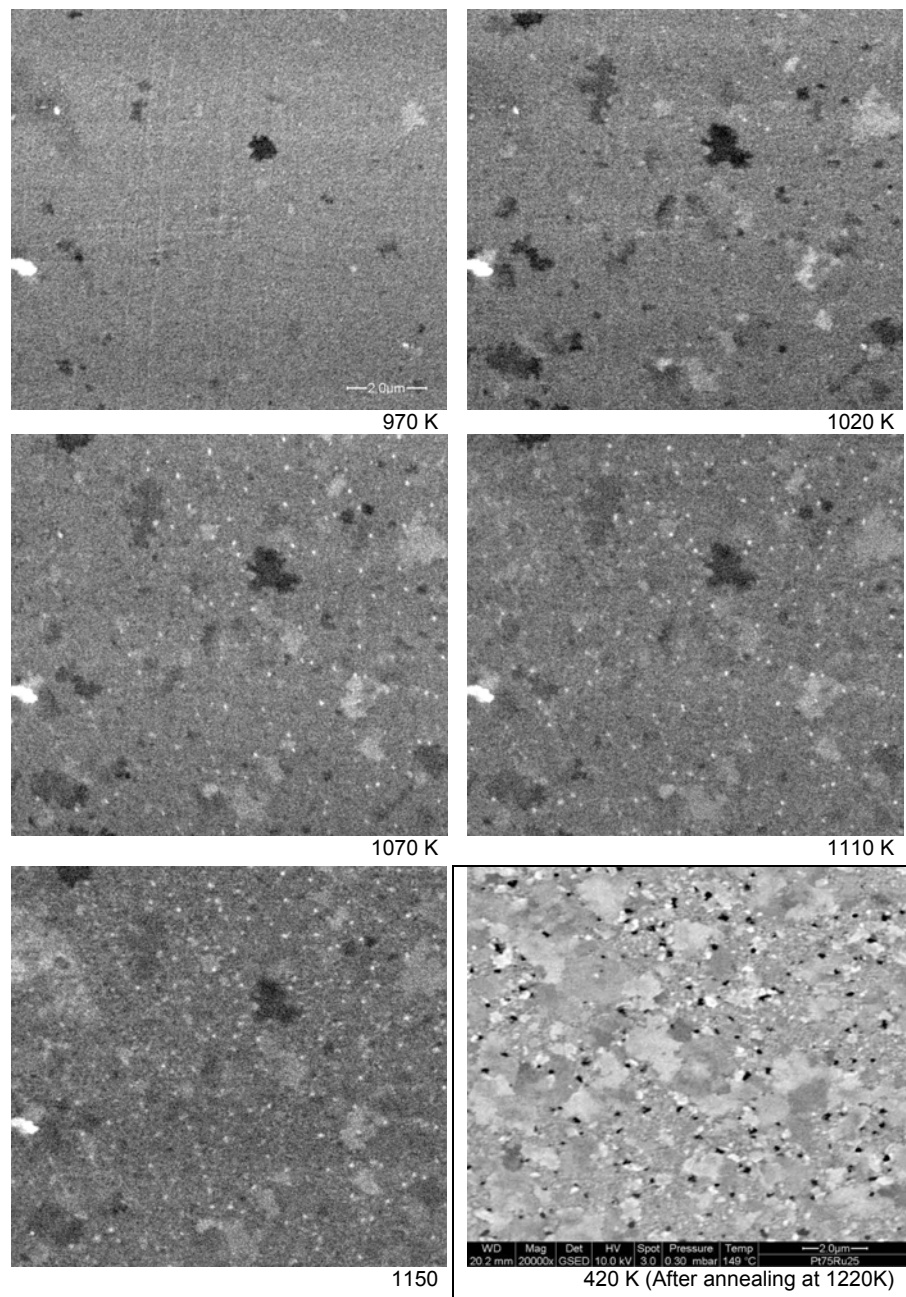
Figure 15. Annealing sequence of the Pt 75Ru25 sample. The same area is depicted in the first 5 images. Last images is relative to a different area measured after the cooling down of the sample.

6.1.3.1 XPS and NEXAFS characterization

All NEXAFS work was carried out at the U7A NIST/DOW end station of the National Synchrotron Light Source (NSLS) at Brookhaven National Laboratory. A backpressure of 1 x 10^{-7} Torr of CO was maintained in the NEXAFS UHV chamber while the samples cooled to ~ 150K. Once the sample array temperature reached 150K, the CO leak valve was closed and the C K-edge NEXAFS of adsorbed CO was collected from each composition on the array in partial electron yield (PEY) mode. The PEY signal was collected using a channeltron electron multiplier with an adjustable entrance grid bias. The spectra were collected at the magic angle of 54.7°, relative to the surface, to remove any polarization dependence of the resonant states, thus allowing NEXAFS signals from the different samples to be compared directly even if the average orientation of the adsorbed CO varied as a function of the surface alloy composition.

XPS analysis was carried out with a Scienta SES-100 hemispherical electron-energy analyzer and a multichannel detector (Gammadata), using a Mg K_α source. Compositions of the samples were measured with relative bulk versus surface sensitivity using 55° and 5°-10° take-off angles, respectively, to the spectrometer (fig. 16). At these two angles it is estimated, using the inelastic mean free path of the photoelectrons at the Mg K_α energy (Tanuma-Powell-Penn equations [1,2]), that the sampling depth is within the top 10 layers (55° take-off) versus the top 2 layers (5°-10°) of the surface.
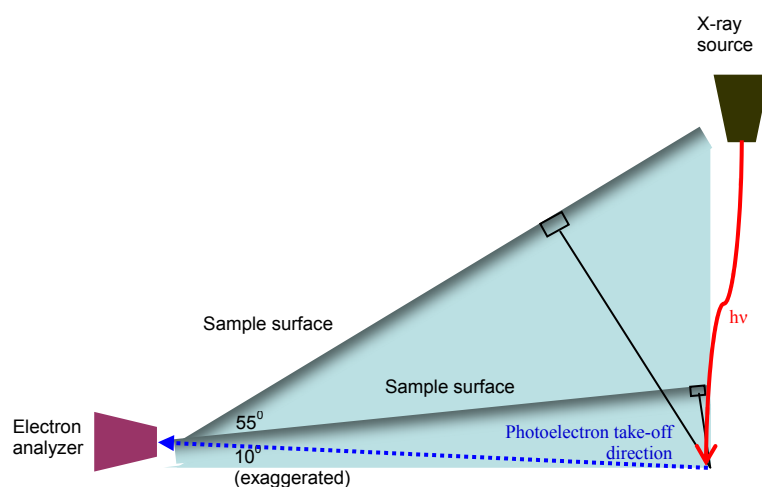
**Figure 16**. Experimental setup for XPS and NEXAFS measurements

Angle-resolved XPS allows us to look at the electronic structure of the Pt-Ru alloys at the surface to sub-surface sensitivity. We observe in figure 17 the Ru $3d_{5/2}$ and the Pt 4f spectra obtained at 55° take-off angle as well as 5°-10° take-off angle. The compositions of the alloys at the two depths were obtained using curve-fitting and the sensitivity factors derived from the pure metals. We see that there is a surface and sub-surface alloy composition that is different from the bulk nominal compositions. The surfaces of the alloys show Ru enrichment while the sub-surfaces show a Pt enrichment with respect to the nominal composition. This phenomenon is internally consistent since a surface enrichment Ru through rearrangement of the near-surface region will necessarily leave a sub-surface layer depleted of Ru. A similar phenomenon was observed Stamenkovic *et al.* where the PtCo system showed Co enrichment of the surface layer upon annealing [1].

As expected, and in accordance with results published by others, alloying of Pt with Ru is accompanied by core-level shifts [2]. At 55° take-off angle we observe a 0.3 eV and a 0.2 eV shift of the Ru $3d_{5/2}$ and the Pt 4f core levels, respectively in the nominally $Pt_{50}Ru_{50}$ alloy with respect to the corresponding elemental lines, which compare to 0.2 eV and 0.1 eV, respectively, to those reported by Liu *et al.* [4]. At 5°-10° take-off angle, the shift is about half as much for Pt (0.15 eV) between Pt and nominally $Pt_{50}Ru_{50}$. A more appropriate comparison between shifts at the two take-off angles is one using alloys that are closest in actual composition. The two closest compositions are $Pt_{35}Ru_{65}$ for the 55^{0} take-off angle and $Pt_{52}Ru_{48}$ for the shallower take-off angle. The former shows a 0.3 eV shift while the latter shows almost zero shift, with respect to Pt. A diminished shift for the surface Pt atoms, with respect to those of the sub-surface, is expected since they are surrounded by fewer Ru neighbors, but is not enough to explain the almost the shift. An explanation could be offered by suggesting that surface Pt is phase segregated from Ru. However, this is not expected from the equilibrium phase diagram. The corresponding surface Ru $3d_{5/2}$ from $Pt_{52}Ru_{48}$ does show a shift with respect to Ru which can be a result of its different crystal structure (fcc solid solution with Pt) from that of Ru (hcp). In fact, the Ru $3d_{5/2}$ from $Pt_{35}Ru_{65}$ shows a bimodal distribution containing both the hcp (hexagonal close package) as well as the fcc (face centered cubic) contributions.

Figure 18 shows a direct comparison of the C K-edge NEXAFS of CO on Pt and Ru. The spectra are being compared on a per-atom basis, as the pre- to post-edge increase in background is normalized to 1 in both cases. The Ru peak max is ~0.36 eV lower than the Pt peak max. We observe a decrease in the $2\pi^*$ resonance when we go from CO atop Ru to CO atop Pt. The decrease in the $2\pi^*$ resonance intensity can be attributed to the filling of the $2\pi^*$ states through increased backdonation from the underlying metal. The 2σ to $2\pi^*$ transition intensity is reduced due to fewer unoccupied final states. Others have shown this effect in a systematic study of transition metal carbonyls [2,3]. Also, the full-width-at-half-maximum (FWHM) of the $2\pi^*$ resonance of CO atop Ru is 1.1 eV and that of CO atop Pt is 1.3 eV. The increase in the FWHM is due to a lowering of the intrinsic energy resolution of the NEXAFS signal resulting from a decrease in the core-hole lifetime of the $2\sigma \rightarrow 2\pi^*$ transition. The decrease in the core-hole lifetime for CO atop Pt in comparison to CO atop Ru is explained by an increased electron occupancy of the $2\pi^*$ state. Sette et al. have made a similar observation with Na and CO co-adsorption on Pt [1]. The higher intensity together with a narrower FWHM of the $2\pi^*$ resonance of CO atop Ru in comparison to the corresponding features of CO atop Pt is consistent with a reduced metal $\rightarrow 2\pi^*$ backdonation from Ru in comparison to Pt.

Figure 19 shows the comparison of CO atop Pt with those of the Pt-Ru alloys. The $2\pi^*$ resonance intensity increases with increasing Ru content while the peak position is nearly the same for all spectra, within the resolution of our measurements. A direct interpretation of the changes in the $2\pi^*$ intensity as a function of the surface composition is complicated by the fact that the FWHM of CO atop Pt is nearly 4 times the difference in peak positions of CO atop Ru and CO atop Pt (see fig. 20), and so the contributions from each species can not be resolved from one another on the case of the alloys. The close vicinity of $2\pi^*$ resonance energies in the alloys to that of Pt would seem to suggest that the CO is predominantly on Pt sites, i.e., CO has sufficient diffusivity on the surface of the alloys at 150 K for CO to move from Ru to Pt sites. While this is within the realm of possibilities, there is no independent confirmation of that. Indeed, if the mobility of CO is limited at 150 K, the TPD results (see fig. 23) suggest that there

is no window of temperature over which the CO is expected to be exclusively on Pt sites. At about 350 K, near the working temperature of a direct methanol fuel cell, the TPD results suggest that 50% of the CO atop Ru would have desorbed versus 20% of the CO atop Pt, and so there is sufficient CO atop Ru to complicate the interpretation of the $2\pi^*$ intensity in the alloys. The CO atop Pt TPD results agree with those from CO atop Pt (111) measured by Burnett et al [3].
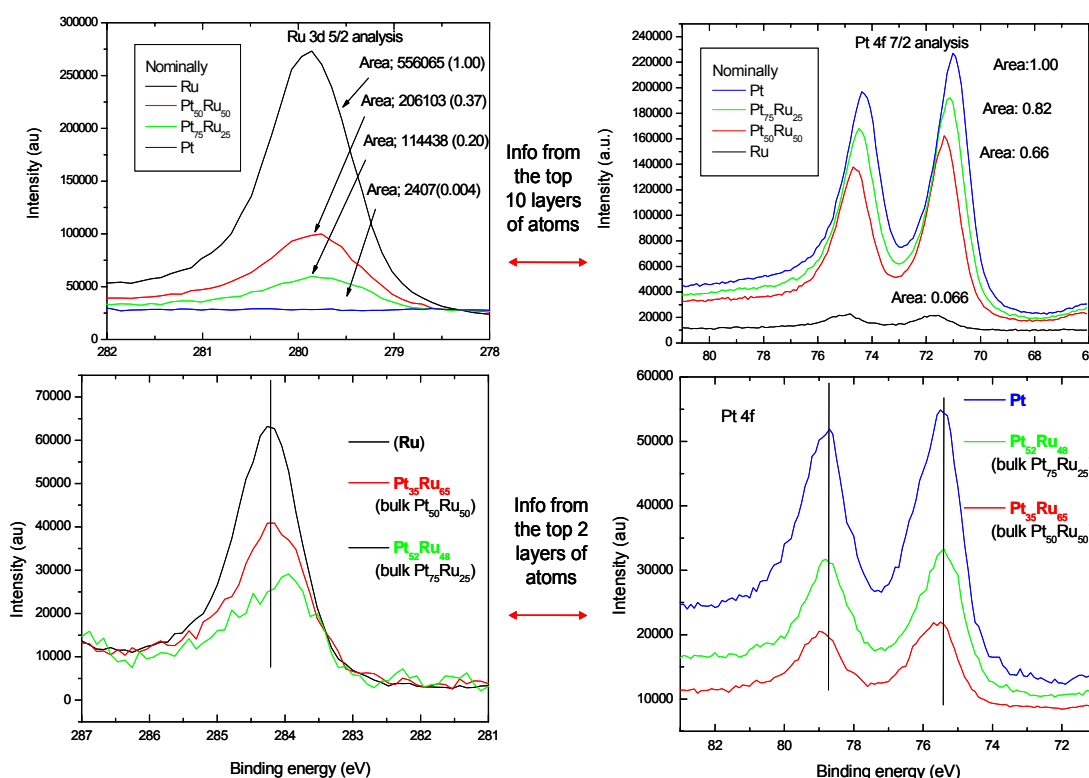
Figure 17. Ru 3d and Pt 4f from 55° take-off angle, a and b, respectively, and 5°-10°, take-off angle, c and d, respectively.
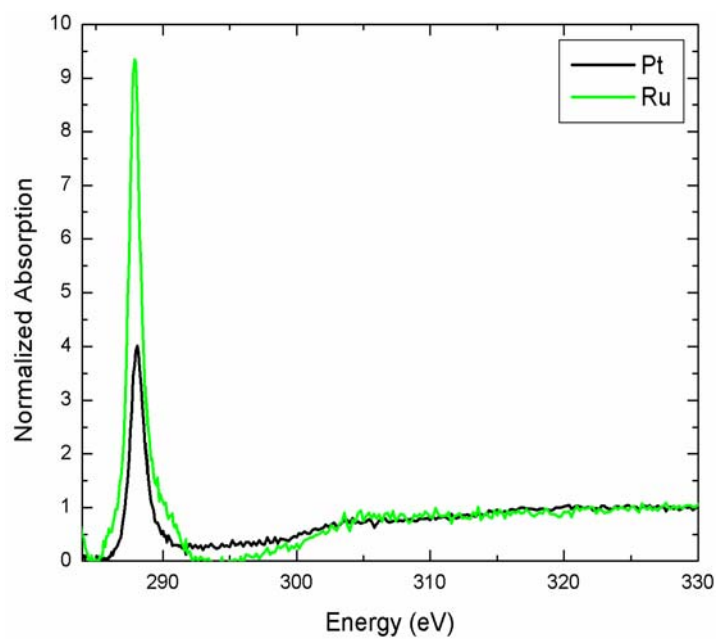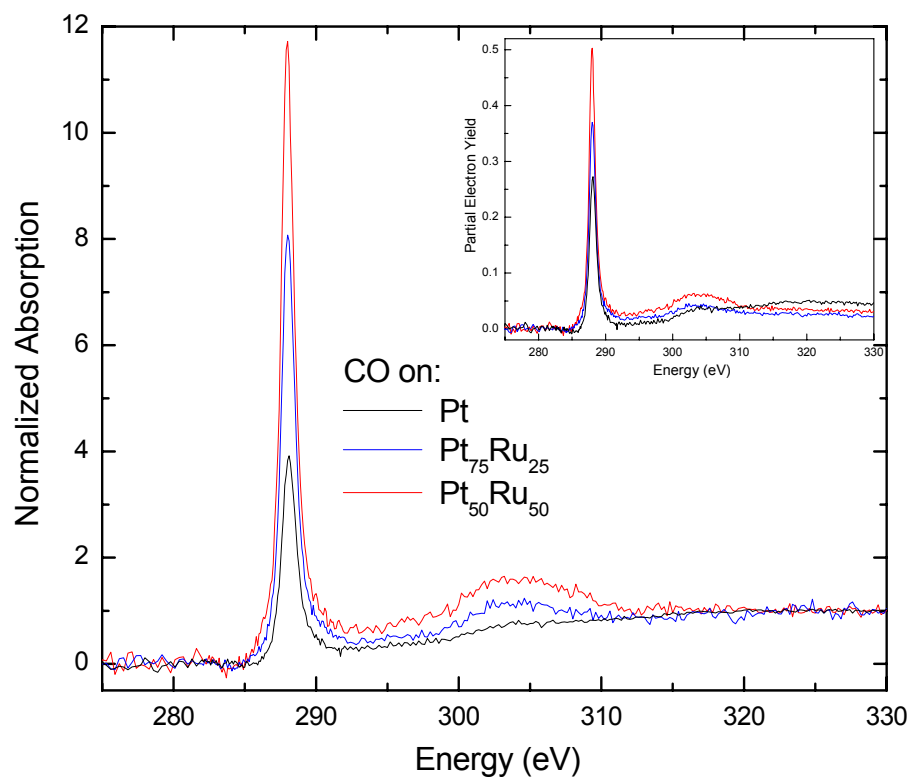
**Figure 18.** C k-edge NEXAFS spectra of CO on Pt and Ru.
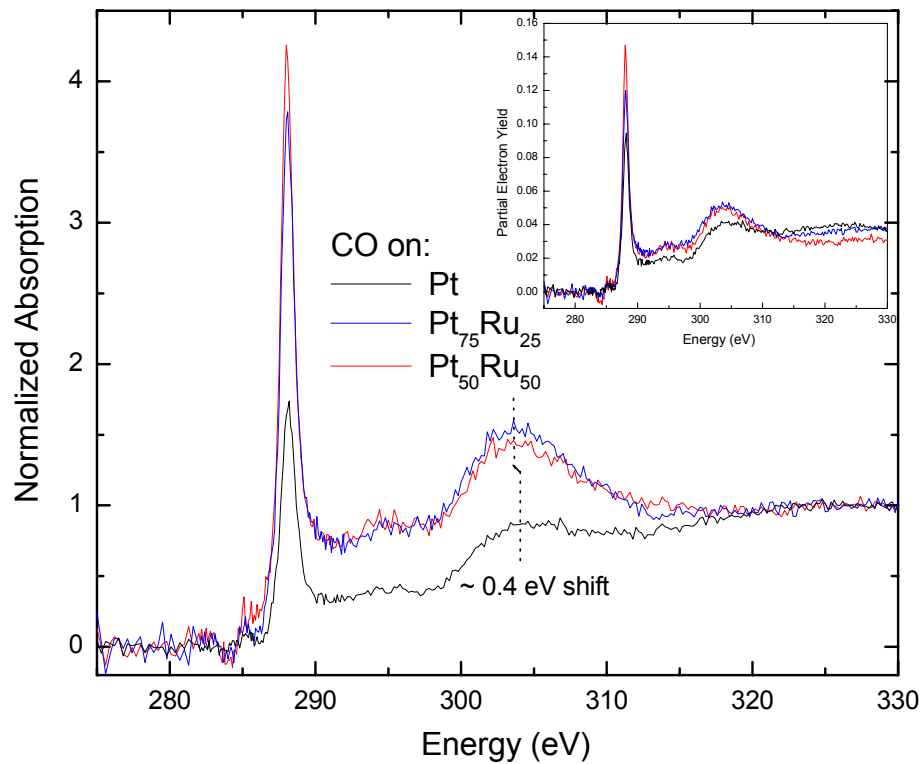
Figure 19. Grazing-angle normalized X-ray absorption at the C K-edge. CO coverage
on the samples is shown in the inset. A 0.4 eV shift is seen in the σ* resonance.

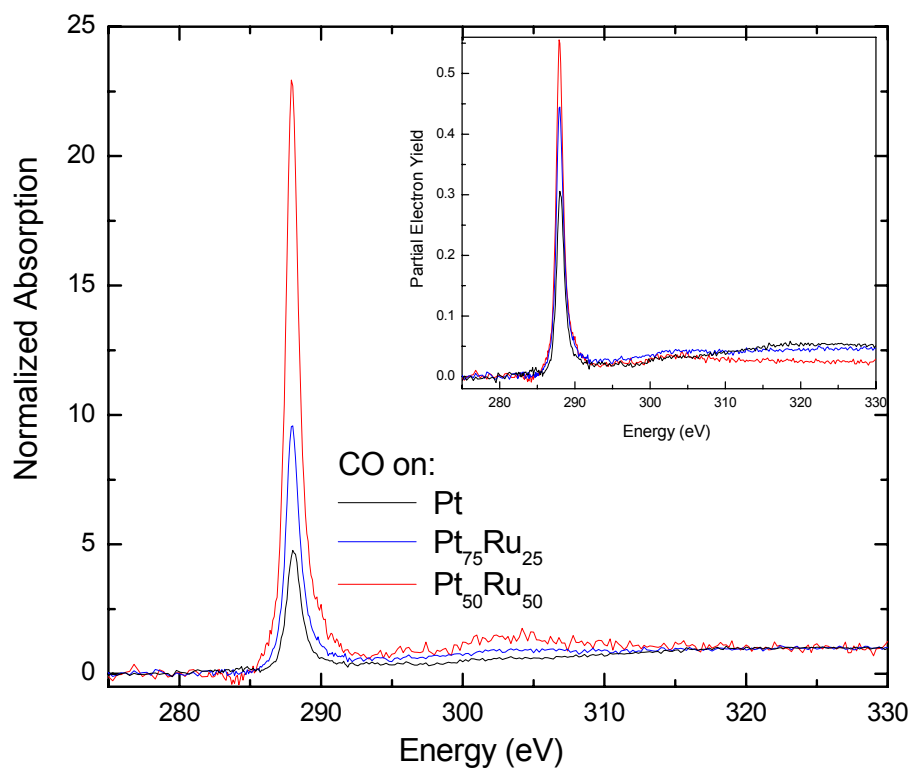**Figure 20.** Magic-angle normalized X-ray absorption at the C K-edge. The intense white line is the $2\pi^*$ resonance. Using pre-edge normalization, the relative CO coverage of the samples is shown (inset).
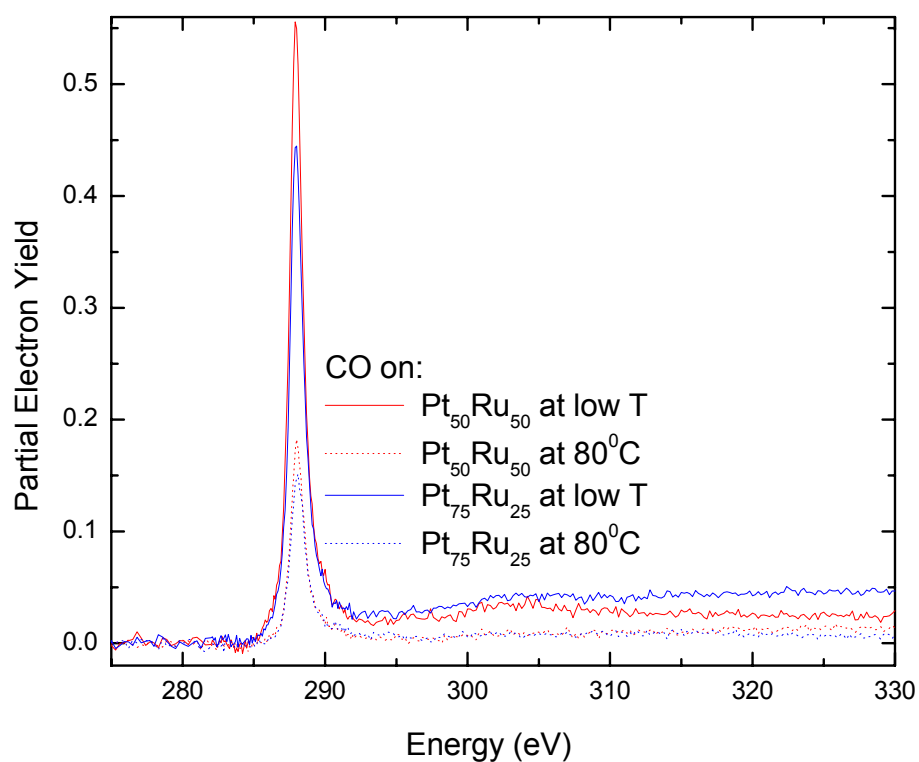
Figure 21. Change in coverage is shown for the $Pt_{75}Ru_{25}$ and the $Pt_{50}Ru_{50}$ alloys between low temperature ($\sim$ -120 °C) and the working temperature of a direct methanol fuel cell

Figure 22. Normal-angle normalized X-ray absorption at the C K-edge.
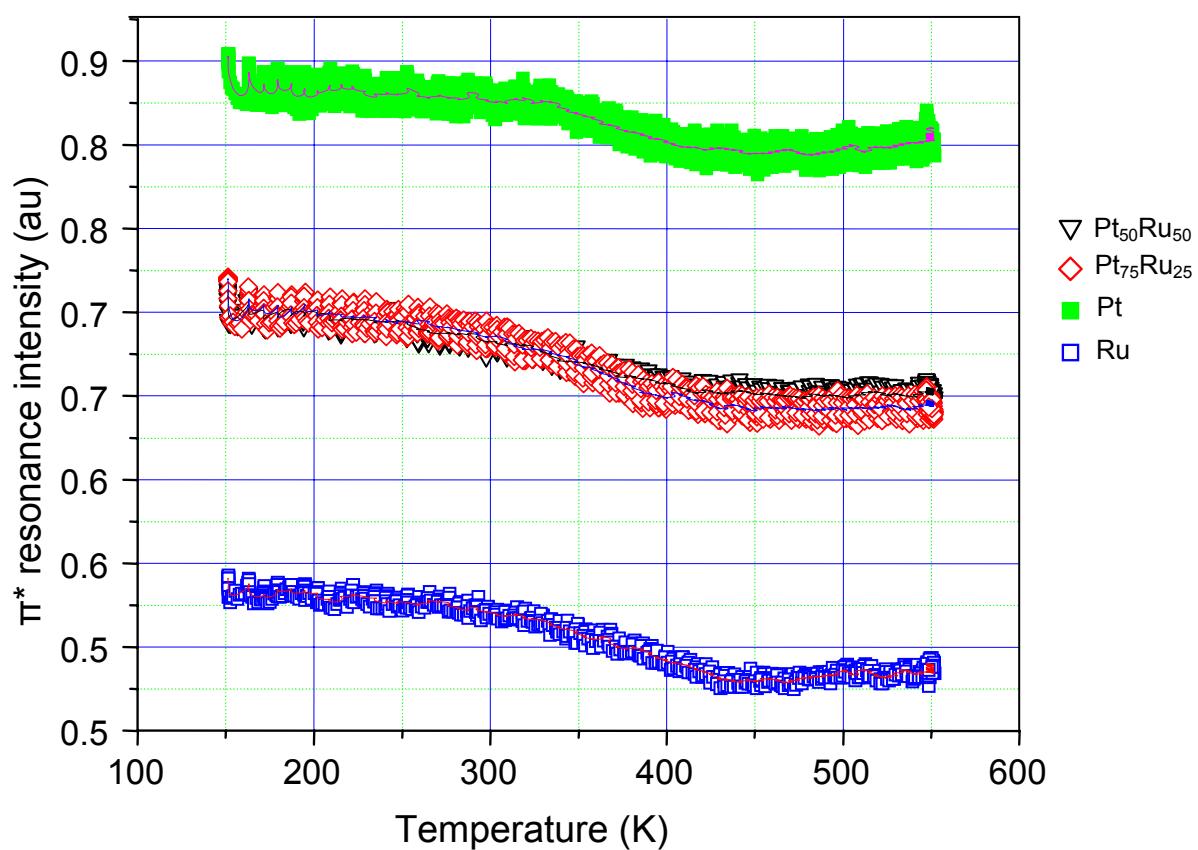
Figure 23. The TPD of CO atop Pt, Ru and Pt-Ru alloys. The lines threading the curves result from Fourier filtered smoothing of the respective data.

6.1.4 Conclusions

From these analysis we can conclude that, Pt-Ru alloys with unique terrace-like morphology formed by interdiffusion giving rise to high surface area thin films. Also the terraces formed on the surface show no compositional contrast either in the bulk or the surface.

We also find that the alloys form a Ru rich surface and a Ru-depleted sub-surface with respect to the bulk composition. This is perhaps a point missed by most surface characterization of nanoparticles where the depth profiling through both angle resolved and photon-resolved photoemission spectroscopies is not possible.

From XPS and NEXAFS analysis we found that the $2\pi^*$ resonance increases as Ru is added to Pt. This means that as Ru is added, electrons are depleted from the $2\pi^*$ molecular orbital (MO) of CO (to levels closer to gaseous CO) and therefore leaving more unoccupied states for photoelectrons to occupy. A lowered occupancy of this MO should move Pt-CO away from metal-like behaviour and increase the core-hole lifetime and reduce the energy resolution of the photoelectron transition to this state. This is indeed what we observe; as Ru is added, the full-width at half-maximum of the $2\pi^*$ resonance decreases.

6.1.5 References

[1] S. Tanuma , C. J. Powell , D. R. Penn, Surface and Interface Analysis 37, no.1, 1-14, 2005.

[2] S. Tanuma, C. J. Powell, D. R. Penn, Surface and Interface Analysis 35, no.3, 268-75, 2003.

[3] V. R. Stamenkovic, B. S. Mun, K. J. J. Mayrhofer, P. N. Ross, N. M. Markovic, J. Am. Chem. Soc. 128, 8813-8819 (2006).

[4] R. Liu, H. Iddir, Q. Fan, G. Huo, A. Bo, K. L. Ley, E.S. Smotkin, Y.-E. Sung, H. Kim, S. Thomas, A. Wieckowski, J. Phys. Chem. B 104, 3518-3531 (2000).

[5] E. Rühl, A. P. Hitchcock, J. Am. Chem.. Soc. 111, 2614 (1989).

[6] A. P. Hitchcock, A.T. Wen, E. Rühl, J. Electron Spectrosc. 51, 653 (1990).

[7] F. Sette, J. Stöhr, E.B. Kollin, D. J. Dwyer, J. L. Gland, J. L. Robbins, A. L. Johnson, Phys. Rev. Lett. 54, 935 (1985).

[8] D. Burnett, A. T. Capitano, A. M. Gabelnick, A. L. Marsh, D. A. Fischer, J. L. Gland, Surface Science 564, 29-37 (2004).

6.2   Cluster assembled nanostructured TiO2

6.2.1 Introduction

Among transition metal oxides, titanium dioxide (TiO2) is of strategic importance for applications in several technological fields such as photocatalysis, optics, solar energy conversion, gas sensing, and as biomaterial coating [1–5]. Recently also nanostructured TiO2 have attracted significant research attention [6, 7] due to remarkable improvement of some properties with respect to its bulk counterpart, as, for example, the catalytic activity [8]. Thus the control of the physical and chemical properties of the nanostructure is one of the key points to engineer suitable materials for different applications.

Wide effort has been paid to the study of molecular processes on oxide surfaces, in particular to the interaction of water with TiO2 solid surfaces [9], due to its extensive presence in the titania applicative environment and then to its strong influence on surface chemistry. The observed photochemical water dissociation on titania surfaces, opening to potential applications in the transformation of solar energy [10, 11], has further boosted experimental and theoretical investigation of water on the TiO2 (see for example Refs. [4, 12, 13]).

The reactivity of titania surface is thought to be favoured by defect sites [14, 15], although their role is still object of debate, as extensively reported by Henderson [9]. Till now, extensive studies have been mainly carried out on defective surface of anatase or rutile crystals (see the review of Diebold [4] and references therein), and not on nanostructured titania which, due to the high specific surface, is expected to have a large amount of native defects.

The purpose of this paper is to investigate the electronic structure of cluster assembled nanostructured titanium dioxide in their native status. The work was mainly focused on the study of defects associated with oxygen vacancies in as-deposited samples. The ns-TiO2 films were grown in high vacuum conditions by supersonic cluster beam deposition (SCBD) using a pulsed microplasma cluster source (PMCS) [16–19].

The nanoparticles produced within the source are carried by an inert gas supersonic jet and then deposited with a kinetic energy low enough to avoid their fragmentation. In this way it is expected that the highly defective structure of the precursor clusters is partially preserved. Moreover the mass distribution of the flying clusters can be aerodynamically controlled allowing to tailor the nanostructure of the film.

This synthesis process offers the further possibility of controlling various properties of deposits, such as grain size, morphology, nanocrystalline phase, and optical gap [18, 20].

The surface and bulk electronic structure of TiO2 single crystals has been the subject of many experimental and theoretical studies [4]. The main valence band photoemission features of stoichiometric TiO2 are observed between 4 and 8 eV below the Fermi edge. This is the energetic region of the O 2p states, but, due to hybridization between Ti 3d and O 2p states, there is also a significant contribution of Ti 3d states [21, 22]. This result indicates that a purely ionic picture is inadequate in describing the Ti-O bonding and that covalency has also to be taken into account.

Moreover when important structural and chemical defects, such as oxygen vacancies, are present, the valence band shows an emission feature related to the unsaturated Ti 3d states at about 1 eV in binding energy [23].

This picture can be highlighted by resonant photoemission spectroscopy (RESPES) [24, 25] which is an effective experimental tool to investigate the ground state electronic structure of 3d transition metals and their compounds [24, 25]. It consists in an intensity enhancement of specific photoemission spectral features when the photon energy is swept through an optical absorption edge (see for example Refs. [26, 27]). In the specific case of titanium in Ti oxides, the sweeping of the photon energy across the 2p (L2,3) [or 3p (M2,3)] absorption edge can excite the Ti atom from its ground state to a Ti 3d photoemission final state via two interfering channels: the direct 3d-photoemission channel and a two step channel, that is the 2p [or 3p] _ 3d* photoabsorption followed by an auto ionization process [28]. As a result of the resonance phenomenon, the valence band emission intensity can be greatly enhanced (see [27] and refs. therein).

As the resonant photoemission process involves an optical 2p [or 3p] _ 3d* transition, only valence band features related to Ti 3d levels are expected to resonate. This effect allows us to probe directly the Ti 3d-O 2p hybridization in TiO2. The first valence band resonant photoemission studies were carried out at the Ti 3p edge of single crystal TiO2 surfaces [14, 29, 30]. They showed a resonant enhancement for spectral features between 3 and 8 eV binding energy confirming a partial Ti 3d character of the primarily O 2p derived states. The increased availability of higher energy soft x-ray sources has allowed expansion of the range of resonant photoemission studies, including the Ti 2p edge, with interesting developments. In fact, at the Ti 3p edge the cross-section for direct photoemission and for the photoabsorption-autoionisation process are comparable, resulting in a moderate resonant photoemission enhancement and strong interference between the two excitation channels.

Moreover, as pointed out by Heise et al. [29], at the Ti 3p photon energy also the optically allowed Ti 3p _ Ti 4s* transition may contribute to the resonant process. At the 2p edge, the direct photoemission cross-section is greatly reduced, and thus the photoemission intensity is expected to be dominated by the photoabsorption induced channel [31]. The photoabsorption occurs mainly via Ti 2p _ Ti 3d* [32] while the Ti 2p _ Ti 4s* cross-section is negligible.

The first resonant photoemission experiment at the Ti 2p edge of TiO2 (rutile) was carried out by Prince et al. [33]. They showed that resonant valence band photoemission profiles in the high and low binding energy region of the primarily O 2p derived band (4 - 8 eV binding energy) can be directly related to the amount of Ti 3d character of the states.

In fact, the profiles follow very closely the Ti L-edge NEXAFS curve of stoichiometric TiO2. Moreover they show that the resonant profile of the defect states (1 eV binding energy) is very similar to the absorption curve of sub-stoichiometric Ti oxide like in Ti2O3 [34]. These results prove that at the 2p edge resonant photoemission provides information on the ground state electronic properties of the Ti atom that can be linked to the local structural environment. The Ti 2p resonant profile of the different valence band features can in fact be regarded as a site-selected XAS curve.

RESPES measurements on cluster assembled ns-TiO2 have then allowed to link electronic and structural properties. This result is of crucial importance for nanostructured titanium oxide where the high ratio between surface to bulk-like atoms can affect the average stoichiometry and the local coordination of the Ti atoms.

6.2.2 Experimental

6.2.2.1 Sample synthesis

The cluster-assembled samples were synthesized by Supersonic Cluster Beam Deposition (SCBD) in high vacuum conditions [17]. Supersonic cluster beams are produced by a Pulsed Microplasma Cluster Source (PMCS), described in detail in Ref. [16]. The source used in these experiments consists of a ceramic cavity that hosts two rods of the material to be ablated that are the electrodes of the source. A solenoid pulsed-valve is used to inject an inert gas plume towards the cathode surface while a nozzle separates the cavity from an expansion chamber.

After injecting the gas (helium in this experiment), a high voltage (about 1000 V) is applied between the two rods giving a discharge that produces a plasma of the carrier gas. Due to the high intensity and directionality of the injected gas, the ablation occurs in a well-confined region of the cathode rod.

The sputtered atoms thermalize with the buffer gas and then condense to form clusters. Finally the gas-clusters mixture expands through the nozzle by supersonic expansion into the vacuum chamber and particles are deposited on the substrate. Since the kinetic energy of the impinging clusters is low enough to avoid fragmentation, a nanostructured film keeping memory of the precursors structure is grown. Mass distribution of precursor clusters can be selected by exploiting aerodynamic properties of the supersonic beam [35]. In particular the cluster beam that exits the nozzle has a spread in the mass distribution of the flying precursors: larger clusters are more concentrated along the beam axis (and hence films can be assembled with selected size of the impinging clusters) [19].

This allows the synthesis of titanium oxide films characterized by different mean grain sizes and relative amount of crystalline and amorphous phases (see fig. 1).

Two samples have been grown with this synthesis approach: one from the deposition of the central part of the beam (labelled nc-TiO2, namely nanocrystalline-TiO2) and one from deposition of its peripheral part (labelled nsa-TiO2, namely nanostructured amorphous-TiO2). The synthesized films have been partially oxidized during the deposition process, but the full oxidation occurs after air exposure.

A reference sample, labelled sp-TiO2, was grown by reactive sputtering technique using a Ti target and oxygen rich plasma. The deposition device was a Leybold sputtering system. Table I reports the list of the analyzed samples.

Sample label	Description	Synthesis
nc-TiO2	Nanocrystalline TiO2 cluster assembled film	PMCS, simple nozzle, central part of the beam
nsa-TiO2	Nanostructured-amorphous TiO2 cluster assembled film	PMCS, simple nozzle, peripheral part of the beam
sp-TiO$_2$	Microcrystalline TiO2 film	Reactive sputtering, Ti target, Oxygen rich plasma

Table I. List of the investigated titanium oxide samples.

6.2.2.2 Characterization techniques

The deposits were characterized at nanoscale by transmission electron microscopy (TEM) with a microscope JEOL JEM- 4000EX (400 kV, spatial resolution 0.17 nm). The films to be analyzed were deposited directly onto TEM copper grids.

Raman spectra were acquired by a Jobin-Yvon T64000 spectrometer in triple grating configuration and detected by a liquid nitrogen cooled CCD camera. Spectral resolution is below 3 cm^{-1}.

The resonance spectroscopy experiments were performed at the Material Science beamline at the ELETTRA synchrotron radiation source in Trieste, Italy [37]. The samples were inserted in the measurement chamber by a fast entry load lock and the base pressure during the measurements was below 10^{-10} mbar. Two samples were observed without any further preparation treatment prior to measurements in

order to observe the samples as resulting from the film preparation and air exposure, and do not affect as much as possible the original defective structure of the films. In fact, due to the relevance of ns-TiO2 in technological applications, it is extremely important to preserve the native structure of cluster assembled films under investigation.

The photoelectron spectra were recorded at normal emission by a Specs Phoibos MCD 150 hemispherical analyzer operating at pass energy from 20 to 50 eV (with a corresponding analyzer resolution of 0.05 and 0.1 eV, respectively). The photon energy resolution of the plane grating monochromator was below 0.2 eV and the photon energy position was monitored by a gold reference sample. A gold mesh was used to measure the incoming photon flux. The resonant spectra were acquired by scanning the photon energy from 454 to 470 eV with a photon energy step of 0.2 eV. The pass energy of the analyzer was set to 50 eV and the kinetic energy step of the valence band spectra was 0.1 eV. These settings allow an adequate energy resolution and signal to noise ratio. At the same time we acquired the Ti L2,3 edge absorption curve in partial yield mode.

Unwanted second order radiation was present in the photon beam, the second order light excites Ti 2p states giving spurious structures overlapping the valence band. By following a standard procedure [33] the second order excited Ti 2p peaks were fitted at photon energies above the L2,3 edge where there was no overlapping with the valence band. The peaks were then displaced, normalized and subtracted from the experimental spectra to obtain the present results.

6.2.3 Results and discussion

6.2.3.1 Morphology and nanostructure

Figure 1 shows TEM images of the nc-TiO2 (a) and nsa-TiO2 (b) samples. The former shows that several rutile, anatase and brookite nanocrystals are embedded and dispersed in an amorphous TiO2 matrix. Their size ranges in the nanometer scale with a typical average dimension of 3 nm. In the nsa-TiO2 samples, the amorphous structure dominates. Both samples have been concurrently deposited

with a simple nozzle (see Table I), and the only difference lies in the cluster precursors size. They are larger for the first sample with respect to the second one, being the former collected at the centre of the target substrate where the larger mass clusters trajectories end. Lighter clusters are scattered over a larger target area producing an amorphous halo around the nanocrystals-rich centre.

The ns-TiO2 samples and the sp-TiO2 sample have been characterized by Raman spectroscopy, too. The collected spectra show that the sputtered film appears be microcrystalline with a dominant anatase phase and a secondary rutile phase (data not shown). The spectra from the nanostructured samples, on the other hand, are dominated by broad lines hindering an analysis in terms of crystalline components and pointing out the amorphous nature of those films. As it will be discussed, this observation will be corroborated by XAS measurements.
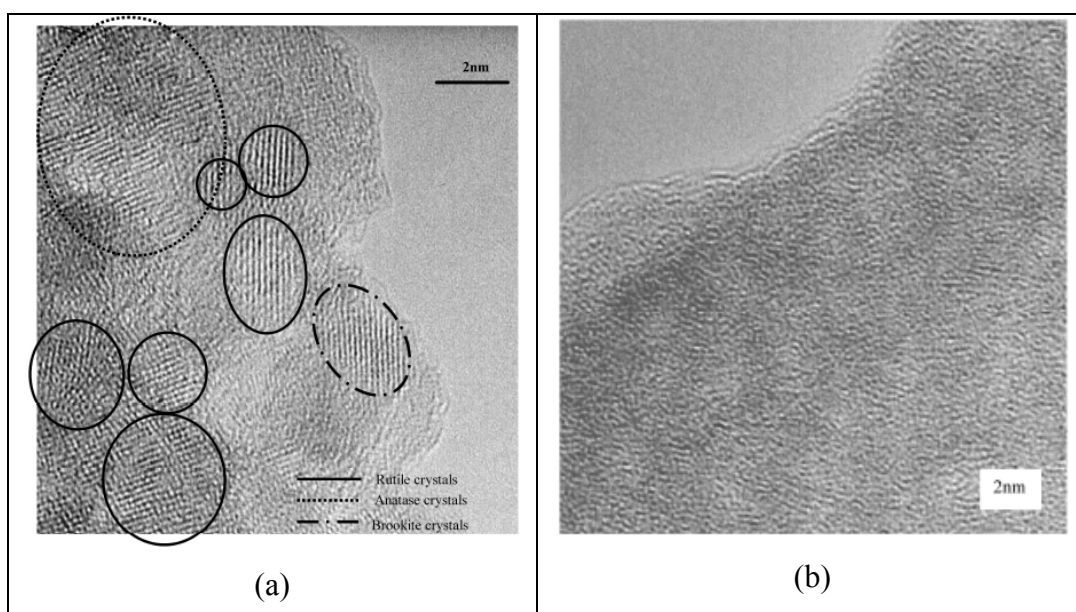

Figure 1. TEM images of the cluster assembled TiO2 films: (a) central beam deposition (nc-TiO2); (b) peripheral beam deposition (nsa-TiO2).

6.2.3.2 Soft x-ray electronic spectroscopy

Preliminary XPS spectra covering a wide kinetic energy range (hν = 614.5 eV, data not shown) have been acquired for all the investigated samples. The photoelectron spectra a part from the titanium and oxygen photoemission lines, exhibit a small carbon contribution coming from usual contaminants.

The Ti 2p doublet photoelectron signal of the examined samples, shown in figure 2, have very similar lineshapes with the doublet component positions placed at 458.6 eV and 464.3 eV [38, 39].
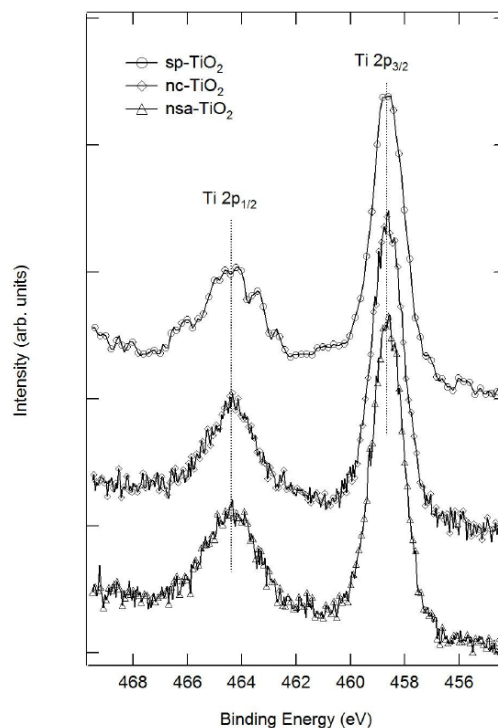
**Figure 2**. Ti 2p photoelectron emission of the investigated samples (hν = 614.5 eV).

No shoulder shifted towards lower binding energies appears, attesting a negligible contribution of TiO2-x oxides and therefore there is no direct evidence of Ti3+ point defects. This suggests that the film surface stoichiometry is close to TiO2.

The local symmetry and the chemical environment of titanium atoms have been investigated by X-ray absorption spectroscopy around the Ti 2p threshold. Ti L2,3 near-edge absorption spectra acquired in secondary electron yield mode (figure 3) display the four peaks due to transitions from the spin-orbit split Ti 2p core levels to the Ti 3d* empty levels which, in turn, are split into t2g and eg sub-bands due to the octahedral coordination of oxygen atoms around the titanium. The L2 and L3 edges are separated by ~ 5.3 eV while the energy separation between L3-t2g and L3-eg is on average of 2.2 eV. The increased Coster-Kronig Auger decay channel for the L2 edge entails a shorter lifetime of the 2p1/2 core hole manifested in the broadening of L2 edge features [40]. The ligand-field splitting

energy can not be simply evaluated has the difference between the energies of t2g and eg, as it happens within a single particle scheme, since strong correlation effects are present. Atomic multiplet calculations with inclusions of cubic crystal field give instead a good description of the L-edge features of d0 transition metal oxides [41].

The lineshape of eg orbitals (dx2-y2 and dz2) is very sensitive to the local symmetry of the metal cations since they form s-type bonds with O 2p orbitals. On the other hand, the lineshape of the t2g orbitals (dxy, dxz and dyz) are sharper due to the weaker interaction of p-type bonds with O 2p orbitals. Going through the sequence from the sputtered sample to the nanostructured ones, as reported in figure 3, the following main differences among the spectra can be observed: i) a growing broadening of the peaks causing an apparent shift of the leading edge towards lower photon energies; ii) the t2g/eg intensity ratio decreases; iii) the lineshape of the L3-eg peak changes.

In particular, with respect this last point, the sp-TiO2 shows that the L3 band is composed by two overlapping sub-features (indicated with P and Q in figure 3), whereas in ns-TiO2 samples this splitting is not well resolved.
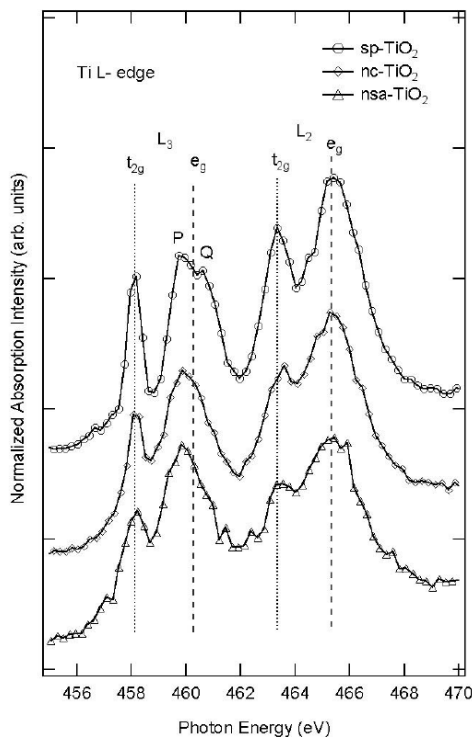
Figure 3. Ti L2,3 edge X-ray absorption spectra in secondary electron yield. Vertical bars are placed in correspondence of the absorption peaks relative to the t2g and eg orbital for each edge.

The NEXAFS spectra of rutile or anatase phases show an intense and narrow t2g band and a splitting of the eg band [4]. The L3-eg component is better resolved than the L2-eg, mainly due to the above mentioned lifetime-related broadening of this peak. The L3-eg component is better resolved than the L2-eg, mainly due to the above mentioned lifetime-related broadening of the latter. Crocombette and Jollet [42] indicate that the presence and shape of eg sub-bands may reflect long-range effects, at least due to the interactions of titanium with second-neighbor shell.

Amorphous titania systems exhibit L2,3 edge with broad peaks and structureless eg bands, as observed for TiO2 crystal surfaces sputtered with ion beam [34], and for natively amorphous TiO2 and titania aerogels [40]. Kucheyev et al. [40] ascribe the peak broadening to a lost of the long range order due to the effects of interactions of titanium with second-neighbour atoms. Both, the nc-TiO2 and nsa-TiO2 XAS spectra well resemble those of the amorphous TiO2 where the L2,3 edge show broad structures, low intensity of the t2g and structureless eg [40]. The sp-TiO2 sample shows instead a definite crystalline structure as indicated by the sharpness and higher t2g and the double features of eg band structure, similar to that seen in stoichiometric anatase TiO2 [40].

To obtain a deeper insight into the local environment of titanium, we have performed resonant photoemission experiments by sweeping the photon energies around the Ti L2,3 edge and acquiring the valence bands emission from the samples under investigation. Figure 4 shows selected valence band spectra of the nc-TiO2 sample. In the region of the primarily O 2p derived states (between 3 and 9 eV), two major features can be identified at about 7.5 and 5.2 eV, labelled A and B, respectively. The defects related Ti 3d states lay just below the Fermi level and are labeled as C. The first (hν = 454.0 eV) and last (hν = 469.7 eV) photon energies of the series are below the Ti L3 and above the Ti L2 absorption edge, respectively. At photon energies corresponding to absorption peaks the whole valence band shows a resonant enhancement, in particular the defect state region, whose intensity actually vanishes in off-resonance conditions.

As already noted by Prince et al. [33] the maximum resonant enhancement takes place for feature A by a factor 3 while for B the maximum enhancement factor is

1.5. The stronger resonant effect is then observed at higher binding energy and is associated with a higher bonding character of those states, as indicated by Heise et al. [29]. Due to the very low intensity of the defect peak in the off-resonance spectra, the relative resonant enhancement of the peak C cannot be determined, even if at resonance the presence of defects is remarkable (see fig. 4). Analogous results are obtained for the other nanostructured TiO2 samples, as discussed below.
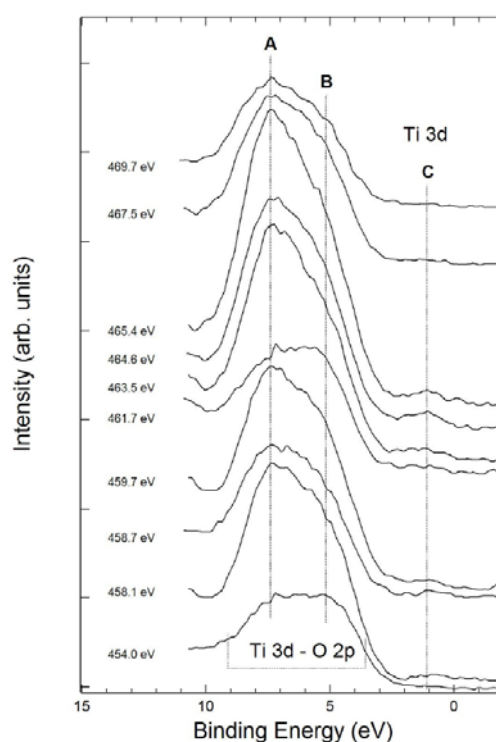

Figure 4. Resonant behaviour of the valence band photoelectron spectra for nc-TiO2 film. Selected spectra are presented for photon energies across the Ti L2,3 edge.

Since the revealed defective states in our samples are not created with any post-production sample treatment, we are in presence of a noteworthy result: the chemical (oxygen vacancies) and/or structural defective states are native and specific of the intimate structure of the cluster assembled nanostructured TiO2 films. As a matter of fact, the study of defective states by RESPES experiments on TiO2 crystals was performed after sputtering and heating the samples in vacuum (see for example Refs. [30, 33]) in order to promote their formation.

Resonant photoemission measurements on the whole series of sample is shown in figure 5 where the off-resonance (hv = 454.0 eV) valence bands are compared to on-resonance (hv = 464.0 eV) ones.

The off-resonance spectra suggest an electronic structure typical of titanium dioxide, i.e. of a wide band gap (~ 3 eV) semiconductor [4]. At resonance, all the samples exhibit a modification of the shape and the intensity of the valence band emission region, with a manifest increase of the relative weight of feature A with respect to feature B. More evident changes appear in the pristine nanostructured TiO2 films, where the signal from the defect related Ti 3d states (binding energy ranging between the valence band maximum and 1.6 eV) clearly arises with similar intensity. This peak is wholly absent in film grown by reactive sputtering, confirming for it the stoichiometric ratio of titanium dioxide. Going into details of the Ti 3d -O 2p band, in off-resonance condition the nanostructured TiO2 spectra show broad and overlapping A and B features, while in the sputtered sample one they are clearly split. In on-resonance conditions, the two features become more distinct even if the double structure is better resolved for the sputtered samples, suggesting a larger local order of these specimens.
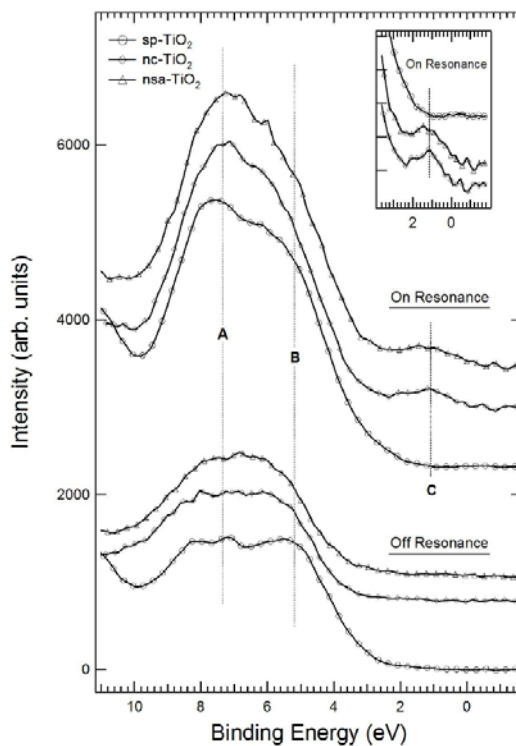
Figure 5. Off-resonance (hv = 454.0 eV) and on-resonance (hv = 464.0 eV) valence band photoelectron spectra of the investigated samples. In the inset a magnification of the defect state region in on-resonance condition.

The RESPES spectra of the valence (feature A) and defect states (feature C) versus the incident photon energy are shown in figure 6. The curves have been generated by integrating the spectral intensities of a binding energy window of 1.5 eV centred at A and C maxima. The curves have been normalized to the integral intensity in off-resonance condition ($h\nu$ = 456 eV). The resonant behaviour of the high binding energy states resemble very closely the Ti L2,3 edge absorption spectra (see fig. 3) characteristic of six-fold coordinated titanium oxide [33, 40]. Actually both doublet splitting and peak widths match the XAS structure. In particular the sp-TiO2 sample shows resonant photoemission intensity curve Ti 3d - O 2p region having the sharper and better discernible features.
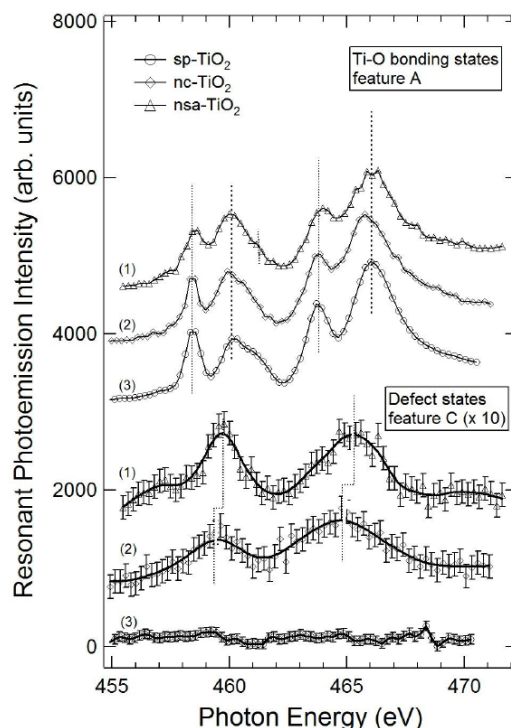
Figure 6. Resonant photoemission intensity curves of the Ti 3d -O 2p (feature A) and Ti 3d (feature C) states. The normalized resonance photoemission spectra have been obtained integrating at binding energies centered at 7.3 eV and 1.0 eV, respectively, over a 1.5 eV wide window (see text). The series of the three bottom spectra has been rescaled by factor 10, an interpolate spline curve is added as a guide for the eyes.

The RESPES profiles of the defect states are very different. For nanostructured samples, we observe two broad peaks centered approximately between each of the

two crystal field split structures (t2g and eg) of L2,3 XAS spectrum. Indeed, the behaviour of this resonance is expected to be different since it is related to defect states where the oxygen coordination is lower, due to the missing of at least one oxygen ligand at Ti probed site. In analogy with the Ti 3d-O 2p RESPES spectra that well reproduce the absorption curve, the defect state resonance curve will be related to the Ti local density of states. In other words, these curves can be considered as "chemical state selective" XAS measurements, since the absorption spectrum is obtained using the "defect states" emission where no "stoichiometric states" emission is present. Our results are consistent with previous RESPES data on titanium dioxide samples at the titanium L2,3 edge obtained by Prince et al. [33] on intentionally defected TiO2 (100) crystal.

Comparing the nanostructured sample spectra, the nsa-TiO2 sample come out to have a higher enhancement of the defects-related resonant signal and a broader and lower Ti 3d-O 2p resonant photoemission features. This behaviour can be related to a lower degree of local order with a larger presence of disordered-like structures. As previously described, this sample was deposited with 10 small clusters and is mainly amorphous. This spectroscopic analysis corroborates this picture.

On the other hand, the RESPES curve of the TiO2 sample grown via reactive sputtering is rather flat, confirming the absence at any photon energy of detectable defect states emission as already observed in the on-resonance valence band spectrum. These results indicate a dominant octahedral symmetry, a stronger hybridization between Ti 3d and O 2p states and in general a higher local

order with respect to nanostructured samples. Furthermore, comparing the RESPES lineshapes of the A peak with previous investigation on similar solids [33, 40], we find that Ti atoms in sp-TiO2 experience a local structural and chemical environment similar to that in anatase crystalline phase.

The nanocrystalline TiO2 sample shows an intermediate behavior between the other two analyzed samples: Ti 3d-O 2p RESPES curve is more similar to the sp-TiO2 sample one, implying higher local order and octahedral symmetry in the fully oxygen coordinated Ti site, whereas the defects states resonant photoemission signal presents more similarity with the nsa-TiO2 one. This

observation agrees with the fact that the nc-TiO2 film is deposited starting from bigger clusters and the above mentioned structural investigations show a higher presence of nanocrystals with defined surfaces and a random orientation. Defects in nc-TiO2 are most likely present both on the TiO2 nanocrystals surfaces and on the nanocrystals boundaries and edges but with a density comparable to the amorphous sample one.

Finally, it is important to note some dissimilarities in the defect related resonant photoemission signal for nc-TiO2 and nsa-TiO2: defects states RESPES curves for nsa-TiO2 are sharper and slightly shifted (on average 0.4 eV) to higher photon energies comparing to nc-TiO2. This result implies that defects related conduction band local density of states (CB LDOS) in nc-TiO2 should extend more inside the band gap respect to nsa-TiO2. Structural and chemical states of the defects are then influenced by the different morphology of the two films (amorphous vs. nanocrystalline).

The possibility to tune the defects electronic structure by engineering the film morphology may open an important route for the applicative use of defects as photoactive sites, as they influence the system band gap, i.e. the overall photo-catalytic activity.

6.2.4 Conclusions

Resonant photoemission across the Ti L2,3 edge has been used for studying both the local order and the electronic structure of nanostructured titanium dioxide thin films assembled by cluster beam deposition. We focused on the differences between nanocrystalline (rutile, anatase and brookite nanocrystals embedded and dispersed in an amorphous TiO2 matrix) and nanostructured-amorphous samples and compared the results with those collected from a reference TiO2 samples grown using reactive sputtering technique having a microcrystalline 11 dominant anatase phase and a secondary rutile phase.

While XAS analysis of both cluster assembled samples ends up to the sole determination of their main amorphous character, RESPES measurements allows

to deeper investigate the valence band states and perform a "chemical state selective" XAS measurements. We determined that the majority of the Ti atoms are in octahedral symmetry (six-fold coordinated with O atoms) in both nanocrystalline and nanostructured-amorphous samples while a certain fraction experience a broken symmetry. On-resonance valence band spectra give evidence for the presence of defect states and their relative amounts showing that the nanostructured (nanocrystalline and amoprhous) samples have a larger abundance of defects. In comparison, no defects states were found in reference TiO2 samples grown using reactive sputtering technique. These defective states are native and specific of the cluster assembled nanostructured TiO2 films.

Since the resonant photoemission spectra of Ti 3d-O 2p band closely resemble the XAS spectra of stoichiometric TiO2, we have got a picture of the local order at Ti sites: in nanostructured TiO2 films there is a strong titanium-oxygen hybridization with a lost of long range order. Moreover the RESPES spectra of the defect Ti 3d peak give XAS-like spectra typical of sub-stoichiometric titanium oxide. The nanocrystalline and amorphous samples show a different defects related local density of states influenced by the overall films morphology (nanocrystalline vs. amorphous)

In conclusion we have used the capability of the resonant photoemission of being site selective and giving information up to now unachievable on the nature of bonds and on the local order of titanium oxides. Thus this spectroscopic approach opens new routes for the investigation of the intimate nature of nanostructured transition metal oxides.

6.2.5 References

[1] M. Grätzel, Semiconductor Nanoclusters-Physical, Chemical and Catalytic Aspects (Elsevier (Amsterdam), 1997).

[2] C. Barbe, F. Arendie, P. Compte, M. Joresek, F. Lenmann, V. Shklover, and M. Grätzel, J. Am. Chem. Soc. 80, 3157 (1997).

[3] A. Fujishima, T. N. Rao, and D. A. Tryk, J. Photochem. Photobiol. C 1, 1 (2000).

[4] U. Diebold, Surf. Sci. Rep. 48, 53 (2003).

[5] D. Brunette, P. Tengvall, M. Textor, and P. Thomsen, Titanium in medicine: material science, surface science, engineering, biological responses and medical applications (Springer Verlag (Heidelberg and Berlin), 2001).

[6] E. Barborini, A. M. Conti, I. Kholmanov, P. Piseri, A. Podestà, P. Milani, C. Cepek, O. Sakho, R. Macovez, and M. Sancrotti, Advanced Materials 17, 1842 (2005).

[7] T. F. Baumann, A. E. Gash, G. A. Fox, J. J. H. Satcher, and L. W. Hrubesh, Handbook of Porous Solids (F. Schuth, K.S.W. Sing, and J.Weitkamp Wiley-VCH (Weinheim), 2002).

[8] H. D. Jang, S.-K. Kim, and S.-J. Kim, J. Nanopart. Res. 3, 141 (2001).

[9] M. Henderson, Surf. Sci. Rep. 46, 1 (2002).

[10] A. Hagfeldt and M. Gr¨atzel, Chem. Rev. 99, 77 (1999).

[11] M. Grätzel, Nature 414, 338 (2001).

[12] I. M. Brookes, C. A. Muryn, and G. Thornton, Phys. Rev. Lett. 87, 266103 (2001).

[13] C. Di Valentin, A. Tilocca, A. Selloni, T. J. Beck, A. Klust, M. Batzill, Y. Losovyj, and U. Diebold, J. Am. Chem. Soc. 127, 9895 (2005).

[14] R. Kurtz, R. Stockbauer, T. Madey, E. Roman, and J. de Segovia, Surf. Sci. 218, 178 (1989).

[15] R. Schaub, P. Thostrup, N. Lopez, E. Lægsgaard, I. Stensgaard, J. K. Nørskov, and F. Besenbacher, Phys. Rev. Lett. 87, 266103 (2001).

[16] E. Barborini, P. Piseri, and P. Milani, J. Phys. D: Appl. Phys. 32, L105 (1999).

[17] P. Milani, P. Piseri, E. Barborini, A. Podestà, and C. Lenardi, J. Vac. Sci. Technol. A 19, 2025 (2001).

[18] E. Barborini, I. Kholmanov, A. Conti, P. Piseri, S. Vinati, P. Milani, and C. Ducati, Eur. Phys. J. D 24, 277 (2003).

[19] T. Mazza, E. Barborini, I. Kholmanov, P. Piseri, G. Bongiorno, S. Vinati, P. Milani, C. Ducati, D. Cattaneo, A. Bassi, et al., Appl. Phys. Lett. 87, 103108 (2005).

[20] I. Kholmanov, E. Barborini, S. Vinati, P. Piseri, A. Podestà, C. Ducati, C. Lenardi, and P. Milani, Nanotechnology 14, 1168 (2003).

[21] S. Munnix and M. Schmeits, Phys. Rev. B 30, 2202 (1984).

[22] A. T. Paxton and L. Thieng-Nga, Phys. Rev. B 57, 1579 (1998).

[23] R. Sanjin´es, H. Tang, H. Berger, F. Gozzo, G. Margaritondo, and F. L´evy, J. Appl. Phys. 75, 2945 (1994).

[24] E. Bertel, R. Stockbauer, and T. Madey, Phys. Rev. B 27, 1939 (1986).

[25] J. Nerlov, Q. Ge, and P. M¨oller, Surf. Sci. 348, 28 (1996).

[26] J. Kikuma and B. P. Tonner, J. Electron Spectrosc. Relat. Phenom. 82, 41 (1996).

[27] V. Formoso, G. Chiarello, R. Agostino, L. Papagno, E. Colavita, L. Floreano, R. Gotter, A. Morgante, A. Santaniello, and A. Verdini, Eur. Phys. J. B 43, 463 (2005).

[28] P. A. Brühwiler, O. Karis, and N. Mårtensson, Rev. Mod. Phys. 74, 703 (2002).

[29] R. Heise, R. Courths, and S. Witzel, Solid State Commun. 84, 599 (1992).

[30] A. G. Thomas, W. R. Flavell, A. R. Kumarasinghe, A. K. Mallick, D. Tsoutsou, G. Smith, R. Stockbauer, S. Patel, M. Grätzel, and R. Hengerer, Phys. Rev. B 67, 35110 (2003).

[31] G. van der Laan, B. Thole, H. Ogasawa, Y. Seino, and A. Kotani, Phys. Rev. B 46, 7221 (1992).

[32] G. van der Laan, Phys. Rev. B 41, 12366 (1990).

[33] K. C. Prince, V. R. Dhanak, P. Finetti, J. F. Walsh, R. Davis, C. A. Muryn, H. S. Dhariwal, G. Thornton, and G. van der Laan, Phys. Rev. B 55, 9520 (1997).

[34] V. Lusvardi, M. Barteau, J. Chen, J. Eng, Jr., B. Fr¨uhberger, and A. Teplyakov, Surf. Sci. 397, 237 (1998).

[35] P. Piseri, A. Podestà, E. Barborini, and P. Milani, Rev. Sci. Instrum. 72, 2261 (2001).

[36] P. Piseri, H. Tafreshi, and P. Milani, Curr. Opin. Solid State Mat. Sci. 8, 195 (2004).

[37] R. Vasina, V. Kolarik, P. Dolezel, M. Mynar, M. Vondracek, V. Chab, J. Slezak, C. Comicioli, and K. Prince, Nucl. Instrum, and Meth. in Physics Research A 467, 561 (2001).

[38] H. Noda, K. Oikawa, T. Ogata, K. Matsuki, and Kamada, Nippon Kagatu Kaishi 8, 1084 (1986).

[39] G. C. Bond and S. Flamer, Appl. Catalysis 46, 89 (1989).

[40] S. O. Kucheyev, T. van Buuren, T. F. Baumann, J. J. H. Satcher, T. M. Willey, R. W. Meulenberg, T. E. Felter, J. F. Poco, S. A. Gammon, and L. J. Terminello, Phys. Rev. B 69, 245102 (2004).

[41] F. M. F. de Groot, J. C. Fuggle, B. T. Thole, and G. A. Sawatzky, Phys. Rev. B 41, 928 (1990).

[42] J. Crocombette and F. Jollet, J. Phys.: Condens. Matter 6, 10811 (1994).